Doctoral Dissertation

Thermal-Mechanical Analysis and Experimental Measurement of Residual Stresses in Wire-Arc Additive Manufactured Typical Parts

（ワイヤアーク積層造形材における残留応力の熱構造連成解析と実験測定）

HUANG WENJIA

June 2024

Division of Global Architecture,

Graduate School of Engineering,

Osaka University

I dedicate this thesis to my beloved parents and wife.

Table of Contents

List of Abbreviations and Symbols

AM: Additive manufacturing

ASTM: American Society for Testing and Materials

FDM: fused deposition modeling

PBF: Powder bed fusion

SLS: Direct metal laser sintering

SLM: selective laser melting

EBM: electron beam melting

UV: ultraviolet

LOM: lamination object manufacturing

DED: Directed energy deposition

LENS: laser-engineered net shaping

EBW: Electron beam welding

WAAM: wire and arc additive manufacturing

HAZ: heat-affected zone

GMAW: gas metal arc welding

PAW: plasma arc welding

CMT: Cold metal transfer

Ti: Titanium

Al: Aluminum

Ni: Nickel

SUS: Stainless steel

XRD: X-ray diffraction

FEA: finite element analysis

LTT: Low-transformation-temperature material

Ms: martensite transformation starting temperature

16Cr8Ni-LTT: LTT material containing 16% chromium and 8% nickel

EDM: electric discharge machine

ISM: implicit method

IEFEM: idealized explicit FEM

ACEXP: accelerated explicit

FE: finite element

Ac1: austenite transformation temperature

DH: deposition height

Mf: martensite transformation finish temperature

TRIP: phase transformation-induced plasticity

BM: base metal

16Cr8Ni-LTT-27%: 16Cr8Ni-LTT with a dilution rate of 27%

λ: X-rays of wavelength

2θ: the diffraction angle

d: diffraction plane lattice spacing

h: Value of FEM node

h_i: Value of measurement point

d_i: Distance between FEM node and measurement point

σ: Standard deviation

T: time

x, y, and z: coordinates

ρ: density

λ: thermal conductivity

q_V:internal volume heat generation rate

$[C]$: heat capacity matrix

$\{P\}$: heat flux matrix

Δt: time step

$\theta \in [0,1]$: weighting factor, with $\theta = 0,0.5,2/3,1.0$

F_i: element of the heat flow matrix $\{F\}$

$A_{i,k}$: element of the i-th row vector of the conductivity matrix $[A]$

T_k: nodal temperature

NF: number of modes with unknown temperature

μ: correction factor

{Δu}: unknown nodal displacement increment

[K]: overall stiffness matrix

[M]: concentrated mass matrix

$\{F_{ext}\}$: external forces

$\{F_{int}\}$: equivalent internal nodal forces

$\{F_{damp}\}$: damping forces

qv: heat source intensity

IU: heat power

h: heat efficiency

$2a$: length of the heat source

$2b$: width of the heat source

C: depth of the heat source

Q: heat-transfer rate

h: heat-transfer coefficient

A: surface area that transfers heat

T: temperature of the hot side

T_{cold}: temperature of the cold side

M: mass of the substance

C: specific heat capacity of the substance

Δt time required for the temperature to change.

ε: strain

ε^e: elastic strain

ε^p: plastic strain

ε^{th}: thermal strain

ε^{tp}: phase transformation plastic strain

f_M: martensite fraction

K: coefficient of transformation plasticity

$\{\sigma'\}$: deviation stress tensor

σ_{XX}, σ_{YY}, σ_{ZZ}, τ_{XY}, τ_{YZ}, τ_{ZX}: stress components

σ_{XX}: average stress

List of Figures

List of Tables

Chapter 1. Introduction

1.1. Additive manufacturing

1.1.1. Introduction

Additive manufacturing (AM) is a layer-by-layer process for fabricating components directly from the 3D CAD models. This process usually involves designing, layer slicing, fabricating the object, post-processing, examination, and testing[1,2]. Different from traditional subtractive manufacturing, AM stands out due to its high design freedom and material utilization efficiency. Additionally, AM demonstrates clear advantages in rapid prototyping and handling a variety of materials simultaneously[3,4]. Nowadays, AM has been applied in multiple fields such as automotive, aerospace, biology, engineering, and medicine[5–7].

AM, originating in the early 1980s, can be traced back to Charles Hull's invention of a technique called stereolithography, which involved curing liquid photopolymer resin layer by layer using ultraviolet (UV) light. This precursor to what is now known as 3D printing paved the way for the technology's achievement. After 40 years of development, AM has branched out into many different directions. Kruth and Helsinki University of Technology have reported their classification standard for the AM processes. In recent years, the American Society for Testing and Materials (ASTM) International announced seven AM technology categories: (1) material extrusion, (2) powder bed fusion, (3) vat photopolymerization, (4) material jetting, (5) binder jetting, (6) sheet lamination, and (7) directed energy deposition[8].

1.1.2. Classification

Material extrusion including fused deposition modeling (FDM) and contour crafting, could deposit thermoplastics, ceramic slurries, and metal pasted through thermal energy. These technologies have advantages like low machine cost and multiple materials application but are short in part resolution and poor surface quality[9,10].

Powder bed fusion (PBF) uses a laser or electron beam to selectively melt a powder bed. This technology is first developed by Deckard and Beaman in the 1980s to process polyamides and polymer composites. Then PBF starts to be applied to process the materials such as ceramics and metals[11,12]. Direct metal laser sintering (SLS), selective laser melting (SLM), and electron beam melting (EBM) are the hot technologies to handle the metal powder with high shape accuracy and good specific parts performance. The problems for PBF mainly focus on the expensive cost of powder production and recycling, complex post-processing, and limited fabrication sizes[13–15].

Vat photopolymerization is a high-speed AM technology and stereolithography is the most representative one. It is known for producing high-resolution parts with smooth surface finishes, making it suitable for applications where intricate details and fine features are required[16,17]. A UV light source is applied to selectively expose specific areas of the liquid resin according to the digital design of the object being produced. After the first layer is finished, the build platform moves down by a small distance, and a new layer of liquid resin is spread over the top. The UV light then exposes the new layer according to the next slice of the digital model, solidifying it in the desired shape[18,19]. The disadvantages of this technology are the process error resulting from over-curing and scanned line shape and limitations brought by the photopolymerization[20,21].

Material jetting has technologies like polyjet printing and inkjet printing which use thermal energy or photocuring as the power source to create three-dimensional objects by selectively jetting or depositing droplets of photopolymer resin or wax material onto a build platform layer by layer[22,23]. The ability to handle various materials and high surface quality make this technology suitable for prototyping, product development, and creating visual models. The limitation occurs in the selection of materials due to the use of liquid materials[24–26].

Binder Jetting is a technique used in metal additive manufacturing where a layer of powdered material, usually metal powder, is jetted onto a build platform[27]. Subsequently, a binder, such as an adhesive or bonding agent, is sprayed onto each layer to fuse the powder layers, creating the desired part[28,29]. Binder Jetting is suitable for rapidly and economically manufacturing large batches of metal parts, but the surface quality and accuracy may be relatively lower. Usually, the sintering or heat treatment is required as a post-processing step to achieve the final part's desired density and mechanical properties[30–32].

Sheet lamination is known as lamination object manufacturing (LOM) which was developed by Cubic Technologies in 1986. This technology involves joining or laminating together thin sheets of material to fabricate three-dimensional objects layer by layer[33]. Sheet lamination presents notable benefits such as diverse material options, cost-effectiveness, broad applicability, elimination of support structures, and fast production speeds, positioning it as a favored technology in additive manufacturing[34–36].

Directed energy deposition (DED) technology is one of the most popular metal AM technologies. Common types of DED include laser-engineered net shaping (LENS),

Electron beam welding (EBW), and wire and arc additive manufacturing (WAAM)[37]. Unsimilar to other AM technologies that use powders or resins, DED applies a focused energy source (laser, arc, or electron beam) to melt the material as it is deposited[38,39]. This feature makes it possible for DED to produce large-scale metal objects with a high deposition rate and minimal material waste. DED also excels in manufacturing complex components which might be challenging or impossible to achieve with traditional manufacturing methods. The wide applicability of DED has earned it a place in the field of repair and refurbishment as well. Although DED has so many advantages, there are still some issues that need to be addressed. Compared to the surface finish by PBF, the one produced by DED is much rougher, and additional post-processing such as machining or polishing is required. Furthermore, the shape accuracy provided by DED is also limited. The great heat input brought by the focus energy source will lead to poor production performance in the deposition part and heat-affected zone (HAZ)[40–43].

1.2. Wire and arc additive manufacturing (WAAM)

1.2.1. Introduction

Wire Arc Additive Manufacturing (WAAM) is a technique used in metal additive manufacturing, which constructs three-dimensional components by depositing and welding metal wire onto the surface of the workpiece layer by layer. This process commonly utilizes arc welding, where the metal wire is melted and deposited in sequential layers through precise control of welding parameters and movement trajectories, ultimately shaping the part according to design specifications.[44] Compared to other AM technologies, WAAM has an outstanding deposition rate, cost-effectiveness,

and high material utilization, which brings advantages in fabricating large-size metal parts, rapid prototyping, and customization. Essentially, WAAM can be classified into DED and the earliest patent related to WAAM appeared in 1920[45]. Afterward, the development of WAAM has been closely linked to advancements in welding technology. WAAM technology has gradually been applied in various fields such as aerospace, automotive, marine, energy, etc., for manufacturing complex metal components, prototypes, and tooling[46].

1.2.2. WAAM methods

Based on the use of welding heat sources, WAAM processes can be divided into three types as shown in Fig.1.1, gas metal arc welding (GMAW), gas tungsten arc welding (GTAW), and plasma arc welding (PAW). MIG is the most selected heat source because the direct-feeding spool of welding wire allows for efficient and continuous wire feeding during the welding process[47–49].

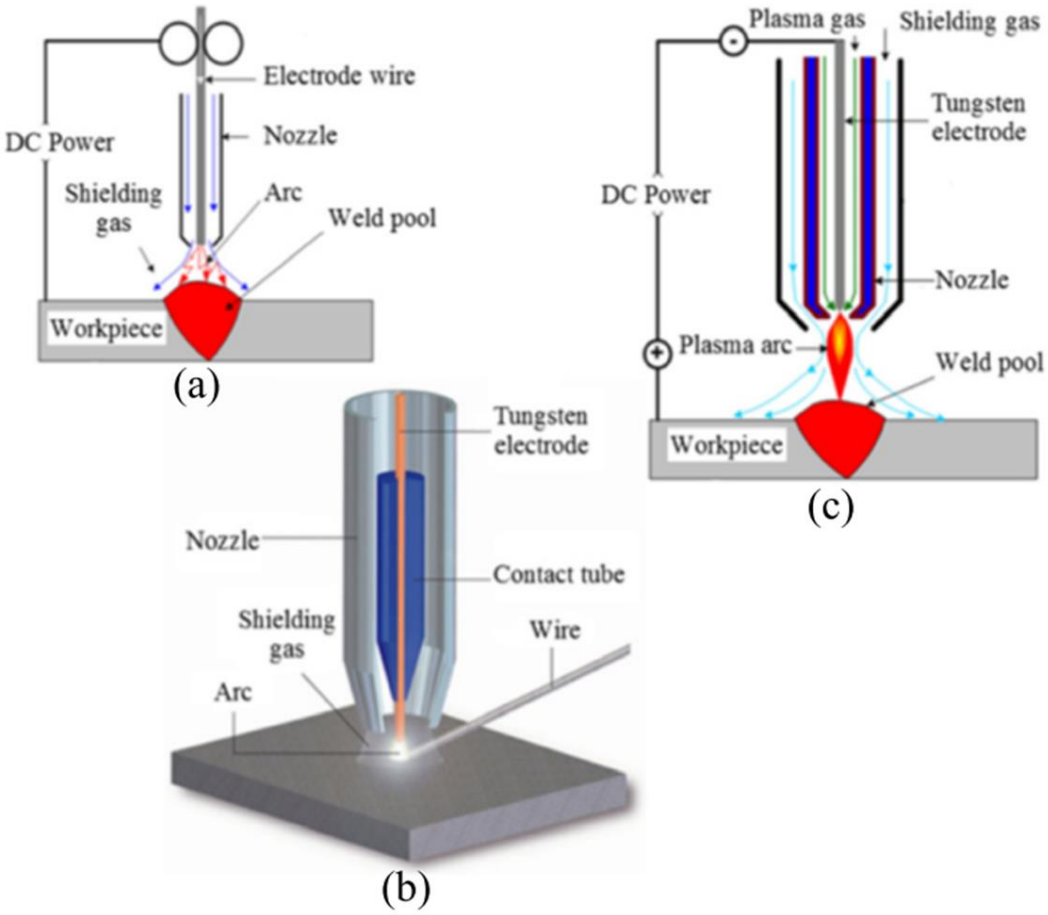

Fig. 1.1. Schematic of WAAM heat source: (a) MIG; (b) TIG; (c)PAW. [46]

MIG is a process that creates an electric arc between a consumable wire electrode and the workpiece. It encompasses four primary welding modes: Globular mode; Short-circuiting mode; Spray mode; Pulsed-spray mode. These modes vary in terms of arc characteristics, metal transfer mechanisms, and suitability for different welding applications[46]. Although MIG has an impressive deposition rate, problems like distortion, residual stress, and poor finish surface still exist. Cold metal transfer (CMT) is recognized as an improvised version of GMAW with reduced heat input and improved weld quality. Through modulating the welding current and arc, the droplet transfer can be controlled precisely[50–52].

Different from MIG, TIG, and PAW use a non-consumable tungsten electrode and externally provided machine for wire feed[53,54]. The welding area of TIG is protected by an inert gas, typically argon, while the workpiece and filler material are melted and joined together by an arc. PAW generates a high-temperature plasma arc by tungsten electrodes and Ionized inert gas to melt the feeding material with substrate. In general, TIG welding is suitable for welding applications that require high precision, high quality, and a superior appearance. On the other hand, PAW welding is suitable for welding thick materials, high-speed welding, and applications that demand a higher welding speed[55–57].

1.2.3. WAAM process steps and equipment

The fabrication of parts through WAAM comprises three fundamental stages: Process planning, deposition, and post-treatment. Fig. 1.2 illustrates the sequence of steps involved in fabricating a part.

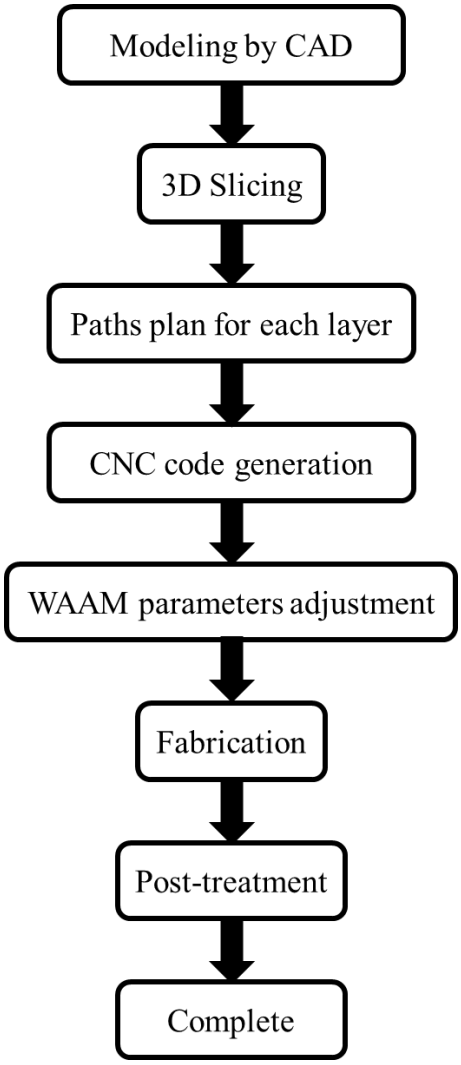

Fig. 1.2. Process steps for WAAM.

The initial step is to create a three-dimensional model using CAD or reverse engineering techniques, such as three-dimensional scanning. The model is then saved in a standard format for use in slicing software. The 3D model is converted into 2D layers of appropriate thickness for accurate deposition by the slicing software. Computer software plans the optimal path and defines parameters for the deposition process. Control of essential parameters like material feed rate, table speed, arc current, gas flow rate, path strategy, and heat input are critical for fabricating components with near-net shape. This planning and programming are tailored for specific materials and parts. Next, CNC code

generation is performed manually or through computer programming. Using selected welding and deposition parameters, the product is additively manufactured layer-by-layer. Deposition begins on the substrate, and subsequent layers are added by moving the nozzle upwards. This process continues until the entire component is complete. Additional processes to enhance part performance may be carried out concurrently or independently during heat treatment if required[45,58–62].

Usually, the WAAM fabrication system includes welding equipment, electrodes and filler materials, gas protection systems, workbenches and motion systems, control, and monitoring systems, as well as post-processing equipment. Fig.1.3 shows the components of a WAAM fabrication system. Given the significant overlap between WAAM technology and welding techniques, there are usually more choices and flexibility available when building a WAAM system to meet different requirements. Two main types, robotic and machine-tool-based, are used to better divide the WAAM system.

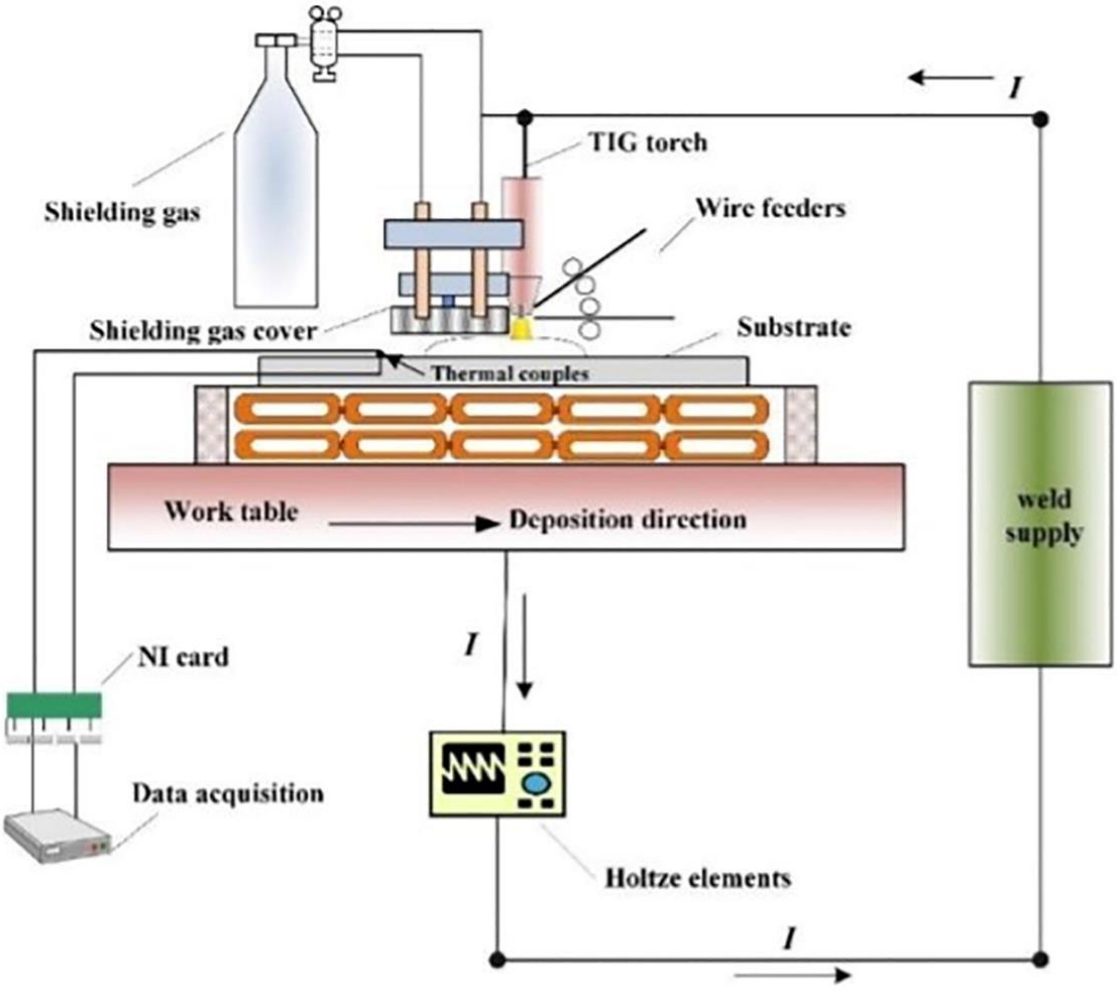

Fig. 1.3. WAAM schematic diagram. [63]

1.2.4. Materials applied in WAAM

Based on the mature welding technology, WAAM has strong compatibility with metal welding wire materials. There are some common options for the deposition material such as Titanium (Ti)-based alloy[64], Aluminum (Al)-based alloy[65], Nickel (Ni)-based alloy[66], and steel-based alloy[67]. Each material has its unique characteristics, and during manufacturing, it is important to choose based on the specific application, weighing the pros and cons. It is even possible to adopt a mix of multiple materials for

certain applications. Currently, the most common applications are in aerospace, automotive, marine, corrosion resistance, high temperature, and tools & molds[45].

The traditional fabrication methods have difficulties when dealing with the Ti-based alloy because of characteristics like the high oxidization rate, low elastic modulus, and low thermal conductivity. WAAM can produce large-size Ti-based alloy components with a high deposition rate and low equipment cost. A lot of research has been carried out on the macrostructure, microstructure, and mechanical properties of the parts fabricated by Ti-base alloy[68–70]. Wang et al. [71] investigate a Ti-6Al-4V WAAM deposition and find that the as-deposited material has a similar average yield and ultimate tensile strengths to a forged Ti-6Al-4V bar but with higher fatigue life. Kennedy et al. [72] focus on grain refinement in Ti-6Al-4V WAAM parts by introducing TiN and ZrN particles. The results indicate that the TiN particles successfully reduce the grain size and modify the columnar grains to equiaxed grains.

Al-based alloy is selected by the industry due to its lightweight design, excellent thermal conductivity, good machinability, and corrosion resistance. Al-based alloy WAAM technology combines the excellent properties of aluminum-based alloys with the advantages of additive manufacturing, making it suitable for a wide range of industrial applications[73–75]. Wang et al. [76] develop a WAAM system based on GTAW to successfully fabricate an Al4043 alloy part. The research indicates that the geometry, finish surface, and hardness are significantly influenced by the WAAM parameters. Ouyang et al. [77] improve the wettability and distortion of a 5356-aluminum alloy WAAM component. The relationships between WAAM parameters, geometry, and deposited layers are investigated.

Ni-based alloys attract interest from multiple fields due to their excellent stability at high temperatures, which is quite suitable for aerospace, aeronautical, and petroleum industries. The combination of Ni-based alloys with WAAM has significantly increased industrial production efficiency for high-performance components while greatly suppressing the increase in production costs[78–80]. Zeng et al. [81] reported a work that fabricates NiTi parts using Ni-rich NiTi wire with the WAAM process. The superplasticity phenomenon is first detected under tensile conditions, which demonstrates the potential of WAAM application in depositing advanced functional materials. Tanvir et al. [82] deposited an Inconel 625 part by WAAM and the heat treatment effect is investigated in his research. The study provides a deep understanding of the relationships between heat treatment time and microstructure transformation in fabricating Inconel 625 by WAAM.

Stainless steel (SUS) is a mature material often used in countless industries. The good corrosion resistance and ductility performance make SUS so attractive in WAAM applications[83–85]. Common types of SUS include ferritic stainless steel (SUS 430, etc.), austenitic stainless steel (SUS 304, etc.), austenitic-ferritic duplex stainless steel (SUS 2205, etc.), and martensitic stainless steel (420, etc.)[67]. Specific research needs to be carried out due to the large difference between these stainless steels in microstructures and mechanical properties after the WAAM process. Wang et al. [84] discussed the effect on microstructure and mechanical properties under different arc modes. The results report that the component fabricated by SpeedArc WAAM has a better solidification structure, greater tensile strength, and hardness than the one fabricated by SpeedPulse WAAM. Le et al. [85] investigate the influence caused by WAAM parameters on a 308L steel wall. The optimization for WAAM parameters is conducted based on the investigation results.

Then, the microstructure and mechanical properties are also evaluated through hardness and tensile tests.

1.3 Residual stress in WAAM

WAAM has made significant progress in the last decade but is still not widely used for practical industrial applications[86]. A crucial factor is the mechanical properties of the finished product. Factors like residual stress, distortion, and microstructure have a great effect on the final performance of the product. Residual stress refers to the stress state that exists within or on the surface of an object without external loading. This type of stress arises due to non-uniform plastic deformation, temperature changes, phase transformations, or other factors within the object[87,88]. Especially, a high heat input leads to high tensile residual stresses, which significantly degrade mechanical properties and shorten fatigue life[89,90].

Shen et al. [91,92] recognized the importance of this problem and used neutron diffraction to characterize the residual stress distribution in the Fe3Al intermetallic wall WAAM components. Sun et al. [93] measured the residual stress in aluminum WAAM components using X-ray diffraction (XRD) and investigated the difference between WAAM and multi-pass welding. Liu et al. [94] investigated the effects of specimen shape and dimensions on the residual stress distribution in a large circular WAAM mockup. In their study, the two-cut contour method was used. Ahmad et al. [95] proposed an effective method to analyze the deformation and residual stresses in stainless steel WAAM components. Two different heat source models were discussed in their work.

Currently, to relieve the high-level tensile residual stresses in WAAM components, the more mature solutions to this problem focus on post-process execution. A rolling method

has been developed and applied to a WAAM residual stress control strategy. Colegrove et al. [96,97] reported that residual stress and distortion in WAAM steel parts can be reduced by interlayer rolling with profiled and slotted rollers. Additional grain refinement occurred when the rolled part was reheated by the subsequent deposition layer. Subsequently, Martina et al. [98] successfully applied the rolling method to large titanium alloy WAAM parts and proposed a new pinch roller for wall structures. The results indicate the potential of this method to reduce the deformation and residual stress in straight WAAM structures. However, a special tool is required when this method is used for structures with complex geometries. With this in mind, Hönnige et al. [99] investigated the function of a roller with a convex surface. It was clarified that the rolling process only promotes microstructure formation and has little effect on residual stress. Heat treatment is another strategy to reduce residual stress. Heat treatment can significantly improve the mechanical strength of parts made with WAAM using Ti alloys, Ni superalloys, Al alloys, and intermetallic Ti/Al [100]. Mughal [101] suggested increasing the preheating temperature to reduce the residual stress. It has been shown that a substrate with a higher preheating temperature combined with continuous deposition reduces the residual stress and distortion. Although heat treatment is so effective, it is still important to realize that improper heat treatment parameters can lead to an increased possibility of cracking under external mechanical load. In addition, it is difficult to apply heat treatments for large-scale WAAM production. Other solutions, such as laser shock peening [102] and ultrasonic shock[100,103], have been excluded due to their high manufacturing costs.

1.4 Numerical simulation for WAAM residual stress

Although the residual stress distribution can be measured experimentally, its formation mechanism during the WAAM cannot be elucidated. Numerical simulation is an effective method to reveal the mechanism of residual stress formation and deformation, and also [104–106]to investigate the characteristics of residual stress distribution as a function of deposition height and shape. The finite element analysis (FEA) is one of the most used methods in numerical simulation[107–110]. Since WAAM is based on the development of welding technology, the welding simulation method can be seamlessly connected to WAAM simulation. Usually, the procedures of WAAM-FEA can be divided into two steps: thermal analysis and mechanical analysis. The flowcharts of analysis are shown in Fig.1.4 and Fig.1.5.

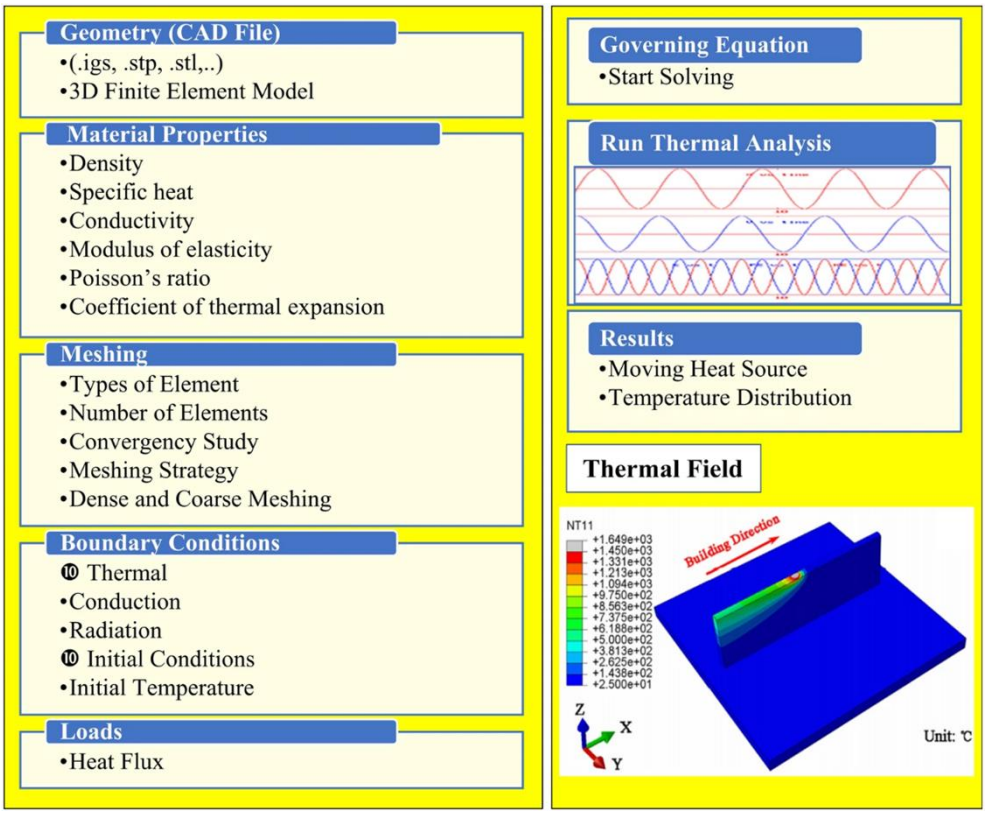

Fig. 1.4. Flowchart of thermal analysis. [111]

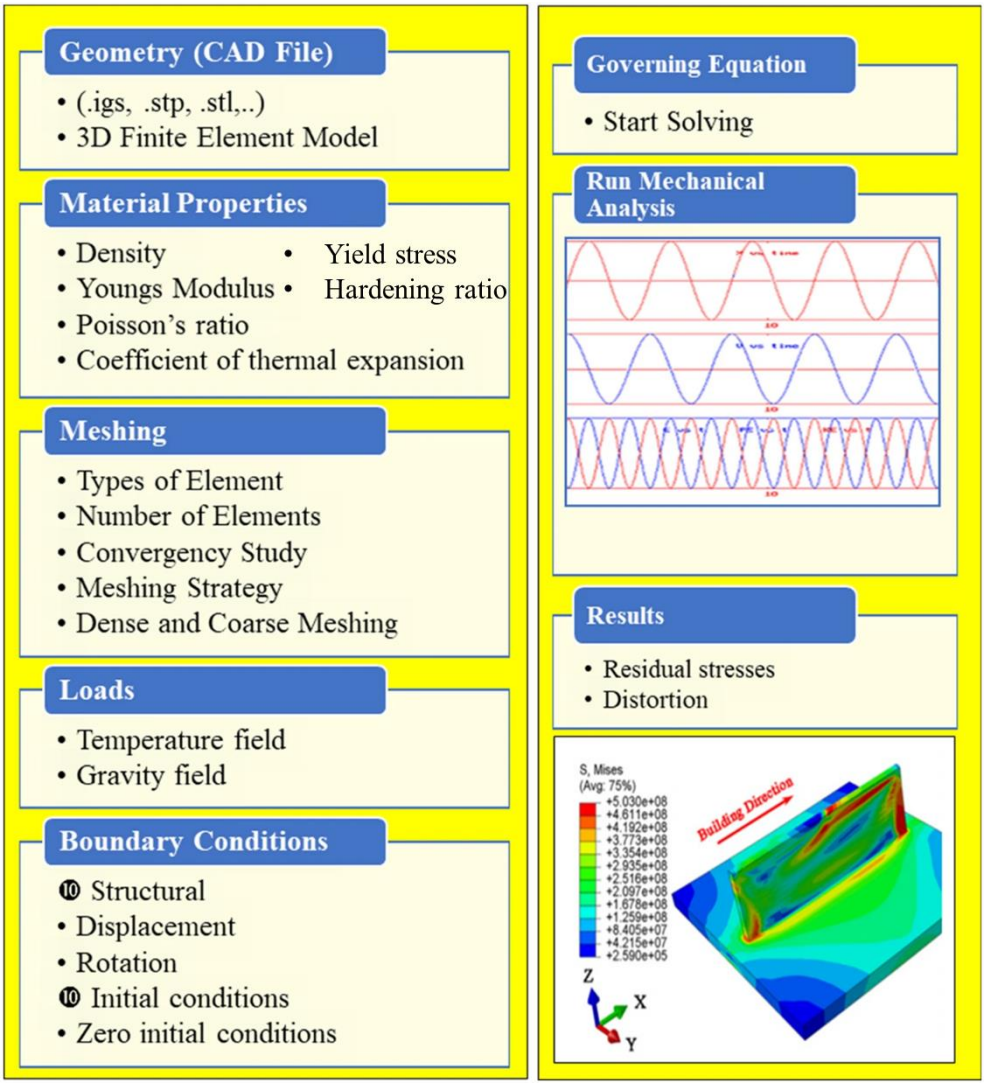

Fig. 1.5. Flowchart of mechanical analysis. [111]

The temperature field, molten zone, heat-affected zone (HAZ), and peak temperature can be obtained by thermal analysis. Through these results, it is convenient to investigate the characteristics and microstructure formation mechanism of deposited materials[112,113]. Mechanical analysis can be coupled with real-time thermal analysis or based on the complete thermal analysis. Coupled analysis generally has higher accuracy, while sequential analysis has higher computational efficiency and the ability to handle large-size models[114,115]. Through mechanical analysis, the residual stress and

deformation can be calculated. The evaluations of part performance, fatigue life, and crack initialization are based on the mechanical analysis results[116,117].

Kumar et al. [111] discussed measurement methods of residual stress in the metal parts and FEA simulations in the WAAM. The conclusion was made that the FEA simulation provides better insights into physical phenomena analysis. Tangestani et al. [118] investigated the effect of vertical and pinch rolling on residual stresses based on the validation of a finite element model. Jia et al. [119] proposed a segmented temperature function method to raise the efficiency of mechanic analysis in large-scale complex WAAM simulations.

1.5 Low-transformation-temperature material (LTT)

Although some studies have proposed effective solutions to reduce residual stress in WAAM, each of them is inevitably flawed. Murata et al. [120] developed Low-transformation-temperature materials (LTT) in the 1990s and indicated that a Fe-based alloy with Cr and Ni as the main alloying elements can make the martensite transformation starting (Ms) temperature to about 180 °C. The LTT uses the volume expansion resulting from the phase transformation to reduce the tensile strain caused by thermal contraction, thereby reducing the residual tensile stress in the weld zone[121,122]. The transformation progress and comparison with conventional material are shown in Fig.1.6.

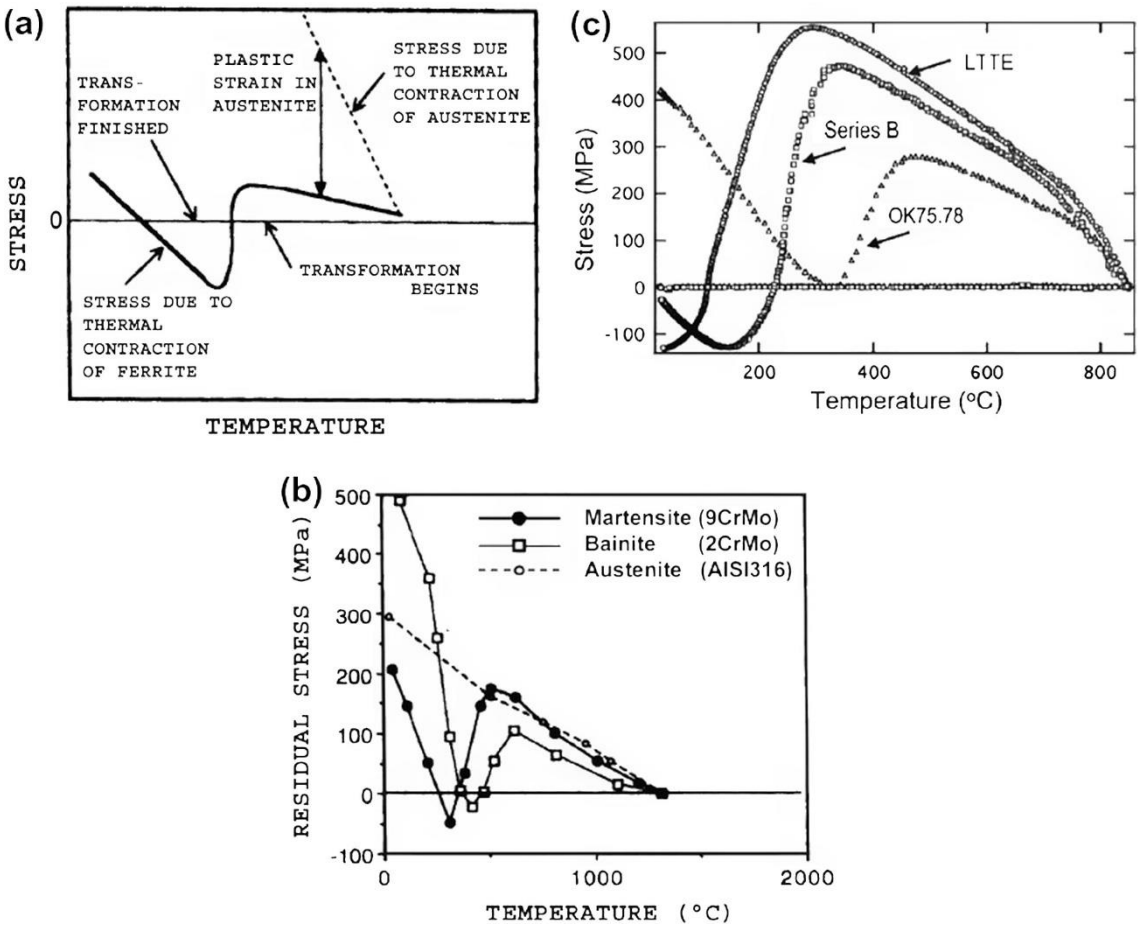

Fig. 1.6. Effect on residual stress with cooling; the balance of phase transformation expansion and thermal contraction. (a) Stress temperature schematic; (b) Satoh test results for final residual stress of different steel phase types on cooling; (c) Satoh test results for conventional (OK75.78) and LTT weld filler alloys (LTTE & Series B). [123,124]

Numerous studies have demonstrated that LTT materials can effectively relieve tensile residual stress and decrease deformation in welded structures[125–127]. Several researchers have conducted in-depth studies on LTT and found that compressive residual stresses are generated in welded structures when the Ms temperature is below 400 °C[128–130]. This eventually enhances fatigue performance and shape accuracy, which are also of great importance in WAAM. Recently, Kitano et al. [131,132] introduced this feature into WAAM to mitigate tensile residual stress and distortion by

applying an LTT material containing 10% chromium and nickel as feedstock. Song et al. [133] fabricated a 26-layer LTT wall sample by WAAM. The microstructure formation and change mechanism are investigated in their research. The result shown in Fig.1.7 reveals that a unique heat treatment caused by the thermal cycle is beneficial to improving the performance of WAAM LTT parts. Plotkowski et al. [134] applied operando neutron diffraction to characterize transient phase transformations and lattice strain evolution during WAAM of LTT. The findings offer a novel approach to designing residual stress states and property distributions in additively manufactured components.

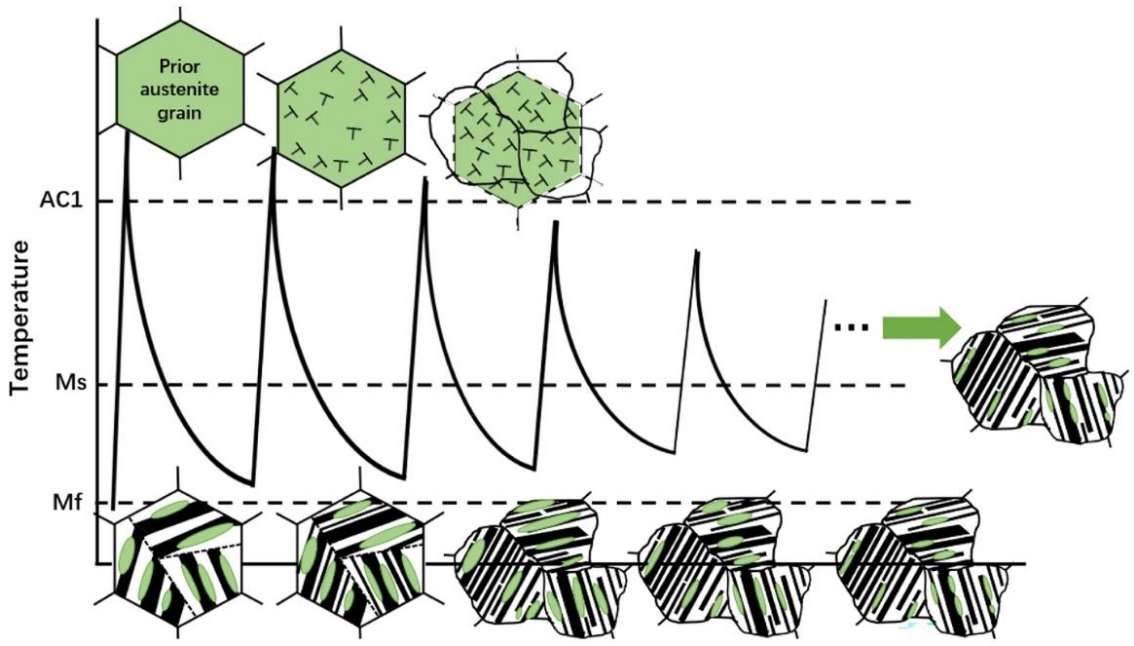

Fig. 1.7. Schematic diagram of thermal history and microstructure of deposition track in the middle of LTT sample. [133]

Moreover, the chemical composition of LTT is similar to that of austenitic stainless steels, implying that LTT possesses excellent corrosion resistance[120]. Additionally, an elevated magnitude of the surface compressive residual stress enhances corrosion resistance[135–137]. In manufacturing storage containers for nuclear waste, where

considerations include the need for long-term underground burial, there is a paramount demand for corrosion resistance on the container surfaces. Compared with powder cladding, WAAM utilizes LTT wires as feedstock, which exhibits remarkable advantages in terms of deposition size, deposition efficiency, and cost-effectiveness[138–140].

1.6 Purpose and outline of this dissertation

As is well known, one of the biggest challenges WAAM faces is how to further improve the mechanical performance of its products, with residual stress being a key factor among them. Residual stress can impact the stability, durability, and performance of components. Therefore, researching effective methods to manage and reduce residual stress to enhance the mechanical performance of WAAM components is an important research direction in this field. As mentioned earlier, most researchers have focused on determining the residual stress distribution through experimental measurements and relieving the tensile residual stresses through mechanical processing. On one hand, to understand and solve the residual stress problem in WAAM, it is necessary to conduct an in-depth analysis of the formation process of residual stress through numerical simulation. On the other hand, if the residual stress problem can be solved from the material's point of view, the tedious post-processing based on existing methods can be avoided and the cost can also be controlled. Therefore, the purpose of this dissertation is to better understand the residual stress problems in WAAM by combining experimental measurement and thermos-elastic-plastic finite element analysis. On this basis, LTT materials are introduced to solve the problem of residual stress caused by high heat input inside WAAM components, and the mechanism is analyzed to better guide the application of LTT materials in WAAM.

In Chapter 1, the introduction and classification of AM and WAAM technologies are first introduced. Then residual stress issues in WAAM and experimental solutions for these problems are discussed. For a deeper understanding of the mechanism in WAAM, the development history and current status of the numerical simulation method for WAAM are introduced in this chapter. Moreover, the research on the application of LTT material in WAAM is investigated. The potential of applying LTT to improve the mechanical properties of WAAM is demonstrated. Fig.1.8 shows the flow chart of this dissertation which includes six parts.

In Chapter 2, the systematic research method for residual stress in WAAM is introduced. The method consists of two parts, experiment measurement and FEA. The mechanism of two major experimental methods applied for the residual stress distribution measurement is revealed. The FEA is carried out by our in-house software, JWRIAN-Hybrid, and the modeling method and modeling verification are given here.

In Chapter 3, stainless steels 308LSi and 304 (i.e., SUS308LSi and SUS304, respectively) are used as the feedstock and substrate to build the wall and pipe WAAM components. A thermomechanical coupling simulation model with an equivalent parallel double heat source is proposed to reproduce the WAAM residual stress distribution, and its accuracy is validated by comparison with the distribution measured by the contour method. On this basis, the formation mechanism of the WAAM residual stress is elucidated. The correlation with the deposition height and shape is quantitatively analyzed, which contributes to the development of the residual stress of the accelerated calculation method in future large-scale WAAM components.

In Chapter 4, the research focuses on a WAAM pipe structure commonly employed in storage or transportation. Substrate deformation and residual stress distribution in the

circumferential direction of the deposition are measured as a reference. Numerical thermal and mechanical analyses are conducted using the in-house software JWRIAN-Hybrid. The simulation results are compared with the measurement results to validate the model. Based on the simulations, the characteristics of LTT residual stress distribution in WAAM and its evolution with an increase in the number of deposition layers are revealed. This provides a clear understanding of the distribution characteristics of LTT residual stresses in WAAM and their formation mechanisms.

In Chapter 5, an LTT material containing 16% chromium and 8% nickel (16Cr8Ni-LTT), developed in our previous research, is used to address the sensitivity to the phase transformation sequence. This study provides scientific insights into LTT-induced compressive residual stresses and highlights the superiority and flexibility of cladding LTT materials via WAAM for improving the resistance of large metal components to fatigue and corrosion.

In Chapter 6, the conclusion of this dissertation is presented.

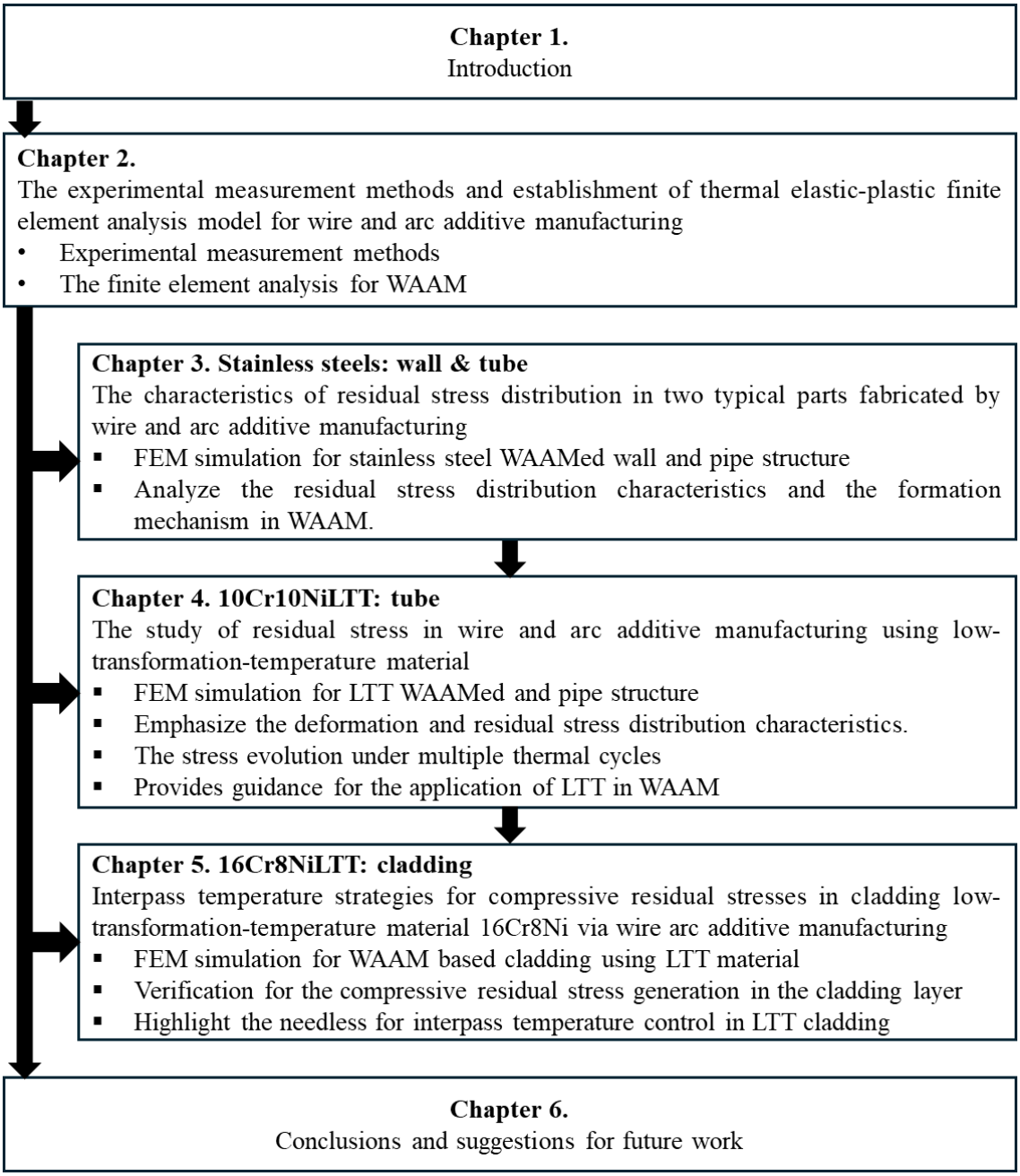

Fig. 1.8. Flow chart of this dissertation.

Chapter 2. The experimental measurement methods and establishment of thermal elastic-plastic finite element analysis model for residual stress of wire and arc additive manufacturing

2.1. Experimental measurement methods

2.1.1. The X-ray diffraction (XRD) method

2.1.1.1. Introduction

XRD is a commonly used material analysis technology used to study the crystal structure and crystallographic properties of materials. XRD technology is based on the diffraction phenomenon of X-rays in substances and determines the crystal structure and lattice parameters of substances by measuring the diffraction angle and diffraction intensity. XRD technology is widely used in materials science, geology, chemistry, biology, and other fields. Its main uses include the following aspects: crystal structure analysis, phase change research, material composition analysis, crystal defect and stress analysis, and material performance evaluation[141–145].

Towards the end of the 19th century, scientific pioneers like Jean-Baptiste Fourier and Auguste Bravais delved into studying the diffraction phenomenon of crystals, laying down fundamental theories in crystallography. Building upon these foundational theories, Dutch physicist Van Laue introduced the Van der Langt equation in 1913, outlining the diffraction principles of X-rays within crystals and providing the theoretical groundwork for the subsequent advancement of XRD technology. In 1912, the father-son duo William

Henry Bragg and Lawrence Bragg formulated Bragg's law based on the Van der Langt equation, delineating the geometric prerequisites of X-ray diffraction and the characteristic patterns of diffraction peaks[146]. This breakthrough laid the groundwork for the practical application of XRD technology.

2.1.1.2. XRD for residual stress measurement

In X-ray stress measurement, the lattice spacing of the crystal serves as the reference distance, and variations in the lattice spacing caused by stress are gauged using the crystal's X-ray diffraction phenomenon to ascertain elastic strain. When a crystal is irradiated with X-rays of wavelength λ, the diffraction angle 2θ and the diffraction plane lattice spacing d are related by the Bragg conditional expression.

$$\lambda = 2d \sin\theta \qquad \text{Eq.2.1}$$

As shown in Fig.2.1, suppose that the crystal spacing on the sample surface changes from $d0$ in the strain-free state to $d0 + \Delta d$ due to stress. In this case, differentiating the above equation with constant wavelength, the equation can be obtained:

$$\varepsilon = \frac{\Delta d}{d_0} = -\cot\theta_0 \,(\theta - \theta_0) \qquad \text{Eq.2.2}$$

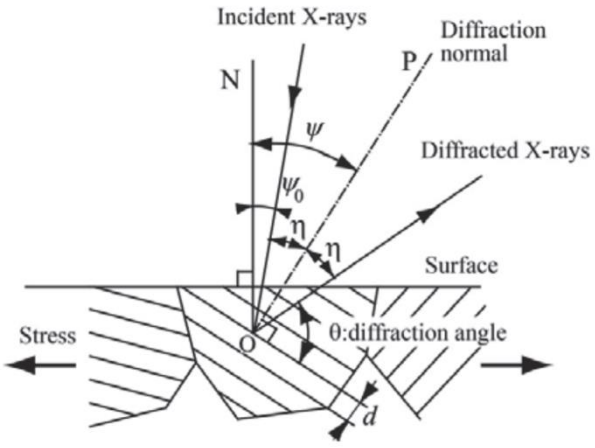

Fig. 2.1. Diagram of strain measurement by XRD. [147]

Here $2\theta_0$ is the diffraction angle without strain. Measuring the change in the diffraction angle allows for determining the change in lattice plane spacing or the perpendicular strain along the diffraction plane. The diffraction intensity curve (also known as the diffraction profile), acquired by exposing a polycrystalline material to X-rays, is a composite of diffractions originating from numerous crystals that meet the diffraction criteria. Hence, the peak value in the diffraction profile represents the average diffraction angle 2θ of numerous diffracted crystals, and the lattice strain derived from this variation using Eq.2.2 corresponds to the macroscopic elastic strain.

Currently, there are two common option methods for residual stress measurement: $\sin^2\psi$ method and $\cos\alpha$ method[148,149]. $\sin^2\psi$ method does not require an accurate determination of the absolute value of the strain-free diffraction angle $2\theta_0$.The stress is determined from the relative change in diffraction angle with $\sin^2\psi$. Determine the stress from the slope of a linear regression of the relationship between diffraction angle (or strain) and $\sin^2\psi$. By using several points to determine the stress value, the variation of the measured value can be suppressed, and the confidence limit of the measured value can be quickly evaluated from the linearity. The influence on the measurement of sample mis-setting, and surface irregularities is limited. The $\cos\alpha$ method determines the stress using information on the entire circumference of the Debye ring obtained with a two-dimensional detector using a single grazing incidence X-ray beam. The $\cos\alpha$ method has advantages such as short measurement time and relatively high accuracy. 2012, a portable, compact, lightweight stress measuring device (PULSTEC u-X360) employing the $\cos\alpha$ method became commercially available.

2.1.2. The contour method

2.1.2.1. Introduction

The contour method is established based on solid mechanics. The specimen will be cut into two pieces through a careful experiment and deformation caused by residual stress on the cutting surface is measured. The contour method is usually performed on metallic components, which can be processed by the electric discharge machine (EDM), for residual stress measurement. The contour method was first introduced at a conference in 2000 and developed in the next decade[150]. The theory of the contour method is based on Bueckner's superposition principles which was proposed in 1958[151]. Schajer et al.[152] proposed a unit pulse solution method that has direct physical interpretations for the residual stress solution approach. Paliaro et al.[153] extend the contour method for multiple residual stress components with multiple cuts. The results indicate a good agreement between the multiple-cut contour method, neutron diffraction, and simulation.

2.1.2.2. Procedures and processes

Basically, the contour method measurement consists of specimen cutting, surface profile measurement, and residual stress calculation by FEM[154]. In specimen cutting, the measurement direction and cutting position need to be determined. The cutting speed for EDM needs to be set very slow to prevent the wire broken during the machining. In surface profile measurement, the residual stress relaxation caused by the cutting leads to elastic deformation on the cutting surface, which can be measured by equipment. Then based on the cross-section geometry, we can build the FE model and input the necessary material properties for elastic analysis. The stresses that need to be applied in the plane to restore the deformed section to a flat state are calculated by transforming the surface

profile data measured in the previous step into displacement conditions perpendicular to the computed cross-section and bringing them into the model. The final result is the original residual stress distribution in the cross-section. Fig.2.2 shows the step flowchart for the contour method.

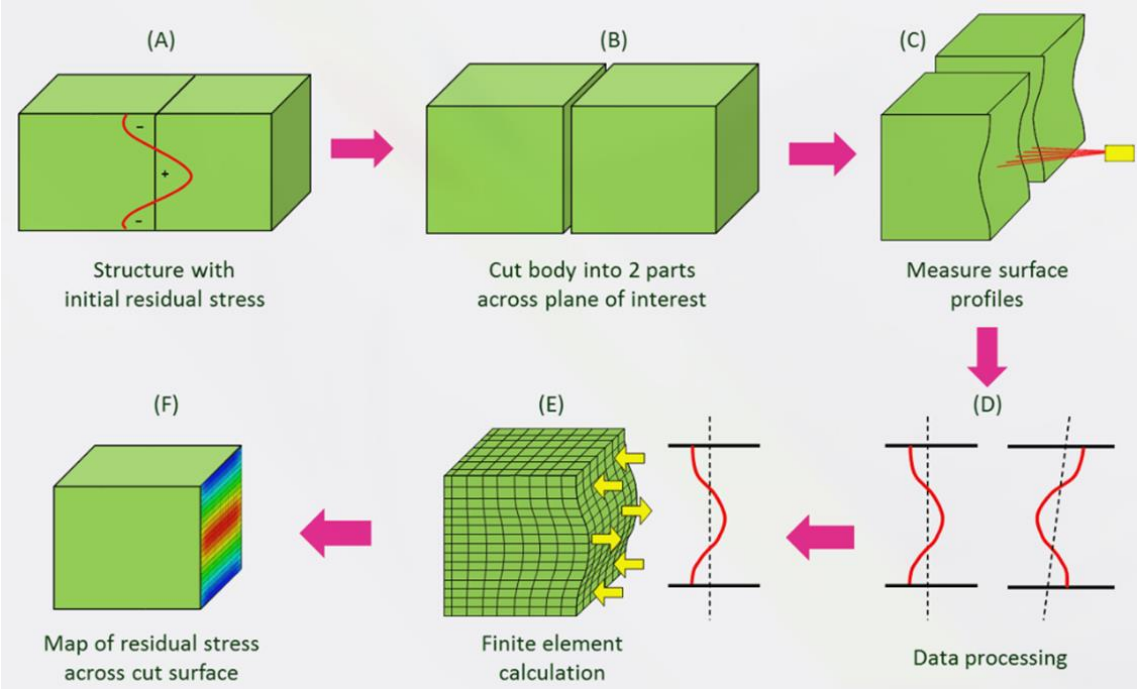

Fig. 2.2. Procedures for contour method. [155]

In this dissertation, the applied contour method is developed based on the in-house software, JWRIAN-Hybrid. The surface profile of the measured cross section is measured with Keyence's VR5000 series 3D shape determination equipment. For accuracy, the camera magnification is adjusted to the highest currently selectable magnification according to the measurement range. In the calculation program, 'SMOOTH_GAUS = σ' is applied, which means the values of each measurement point within a 3σ radius centered on the finite element node are averaged under GAUSSIAN and given to the finite element node as the final value. The process can be explained by the following equations:

$$h = \frac{\sum(W_i \cdot h_i)}{\sum(W_i)} \quad \text{Eq.2.3}$$

$$W(t_i) = \frac{1}{\sqrt{2\pi\sigma^2}}\, exp\left(-\frac{d_i^2}{2\sigma^2}\right) \quad \text{Eq.2.4}$$

h: Value of FEM node

h_i: Value of measurement point

d_i: Distance between FEM node and measurement point

σ : Standard deviation

2.2 The finite element analysis for WAAM residual stress

2.2.1 Thermal analysis

The temperature field calculation in WAAM is the same as the one in welding. The thermal conduction during WAAM is quite complex due to the coupling with the thermal field, fluid field, and electromagnetic field. However, the calculation could be more efficient if we only focus on the transient thermal-mechanical phenomena and ignore the influence of temperature other than melting temperature. Hence, the general partial differential equation of thermal conduction and FEM equation can be given by the following:

$$\rho c \frac{\partial T}{\partial t} = \frac{\partial}{\partial x}\left(\lambda \frac{\partial T}{\partial x}\right) + \frac{\partial}{\partial y}\left(\lambda \frac{\partial T}{\partial y}\right) + \frac{\partial}{\partial z}\left(\lambda \frac{\partial T}{\partial z}\right) + q_V \quad \text{Eq.2.5}$$

$$[K]\{T\} + [C]\left\{\frac{\partial T}{\partial t}\right\} = \{P\} \quad \text{Eq.2.6}$$

Where T is temperature, t is time, x, y, and z are coordinates, ρ is density, c is specific heat, λ is thermal conductivity, q_V is the internal volume heat generation rate, $[K]$ is stiffness matrix, $[C]$ is heat capacity matrix, $\{P\}$ is heat flux matrix. Based on the equations, the conventional implicit method can be presented as follows:

$$\{T\}_{t+\Delta t} = [A]^{-1}\{F\} \quad \text{Eq.2.7}$$

$$[A] = \theta[K] + \frac{1}{\Delta t}[C] \quad \text{Eq.2.7a}$$

$$\{F\} = \left(-(1-\theta)[K] + \frac{1}{\Delta t}[C]\right)\{T\}_t + \theta\{P\}_{t+\Delta t} + (1-\theta)\{P\}_t \quad \text{Eq.2.7b}$$

Where Δt is time step, $\theta \in [0,1]$ is the weighting factor, with $\theta = 0, 0.5, 2/3, 1.0$. To perform the calculation more efficiently, the Newton-Raphson explicit method scheme is also applied[115]. The equation for approximate solution and residual error can be calculated by follows:

$$\{\Delta F\} = \{F\} - [A]\{T\}_{t+\Delta t}^{cal} \quad \text{Eq.2.8}$$

$$B_i(\{T\}) = F_i - \sum_{k=1}^{NF} A_{i,k}T_k, \; k = 1,2,\dots,n, \quad \text{Eq.2.9}$$

Where F_i is an element of the heat flow matrix $\{F\}$, $A_{i,k}$ is an element of the i-th row vector of the conductivity matrix $[A]$, T_k is the nodal temperature, *NF* is the number of modes with unknown temperature. To make each term of $B_i(\{T\})$ converge to 0, the Newton-Raphson method is applied here to get the solution. Finally, each nodal temperature can be expressed as follows:

$$T_i^{N+1} = T_i^N - \mu\frac{B_i(\{T\})}{a_{ii}} \quad \text{Eq.2.10}$$

where μ is the correction factor.

2.2.2 Mechanical analysis

Currently, several efficient methods such as implicit method (ISM), idealized explicit FEM (IEFEM), and accelerated explicit (ACEXP) have been proposed for raising accuracy and reducing the calculation time in thermo-elastoplastic analysis for large-scale multi-layer weld. JWRIAN-Hybrid is developed to analyze the unsteady heat conduction and thermal-elastoplastic mechanical behavior of welds. It improves the calculation

efficiency by applying the implicit and explicit methods to the heating and cooling periods separately[156].

Usually in the implicit method, the unknown nodal displacement increment {Δu} is solved by Eq.2.11 with the known nodal thermal load increment {ΔF}. A large number of components in the overall stiffness matrix [K] are required and this leads to the increase in computation time and memory for storage. In the explicit method, the motion equation shown in Eq.2.12 is applied. [M] is the concentrated mass matrix at the nodes. $\{F_{ext}\}$, $\{F_{int}\}$, and $\{F_{damp}\}$ are the equivalent nodal forces and damping forces due to external forces and stresses at the nodes, respectively. With the accelerated explicit method, acceleration {a} is calculated using small time increments while applying damping. Nodal velocities, displacements, strains, and stresses are calculated in sequence, while convergence calculations are performed at specified times or steps as needed to obtain static balancing. In the hybrid solution, as shown in Fig.2.3, the nonlinear mechanical phenomena during weld heating are calculated using a stable accelerated explicit method, and the thermal stress-strain during cooling is calculated using an implicit method. For multiple thermal cycles, the calculations are carried out by switching iteratively and using explicit and implicit methods, respectively.

$$[K]\{\Delta u\} = \{\Delta F\} \qquad \text{Eq.2.11}$$

$$[M]\{a(t+dt)\} = \{F_{ext}(t+dt)\} - \{F_{int}(t)\} - \{F_{damp}(t)\} \qquad \text{Eq.2.12}$$

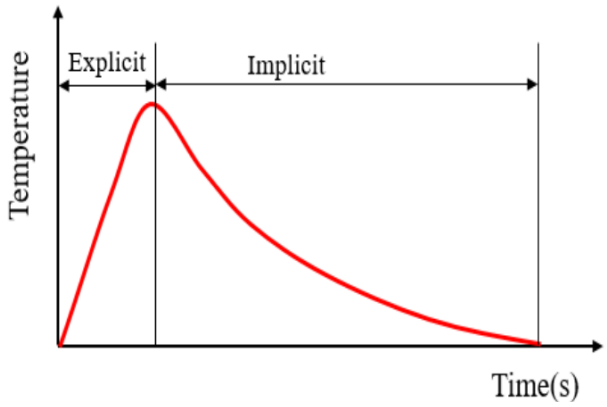

Fig. 2.3. Hybrid method for heating and cooling periods. [156]

2.3. Material model for LTT and mesh size sensitivity analysis

The modeling process for WAAM residual stress in JWRIAN-Hybrid is similar to the one for multi-pass welding. The FE model needs to be created first. For thermal analysis, the melting temperature and temperature-dependent material properties like density, thermal conductivity, and specific heat are required for the temperature field calculation. According to the practical condition, the heat transfer coefficient of each outer surface can be defined individually. In mechanical analysis, the provided material model is based on the thermo-elastoplastic material model. Material properties like Young's modulus, Poisson's ratio, yield stress (or stress-strain curves), hardening coefficient, and thermal expansion coefficient are required here.

For phase transformation materials, the mechanical material properties in heating and cooling periods are both needed when performing the mechanical analysis. The effect of phase transformation on stress field is reflected by the change in the thermal expansion coefficient. In addition, the extra file generated in thermal analysis, which records the peak temperature of each element in every thermal cycle, is also required to distinguish the occurrence of phase transformation and decide which period material properties

should be used. As shown in Fig.2.4, THAZ is the phase transformation temperature for distinguishing heating and cooling material properties and the peak temperature is considered as the reference temperature. When the reference temperature is higher than THAZ, the heating period will use the heating material properties, while the cooling period will use the cooling material properties. When the reference temperature is lower than THAZ, both the heating and cooling periods will use heating material properties, which means there is no phase transformation happening in the current condition.

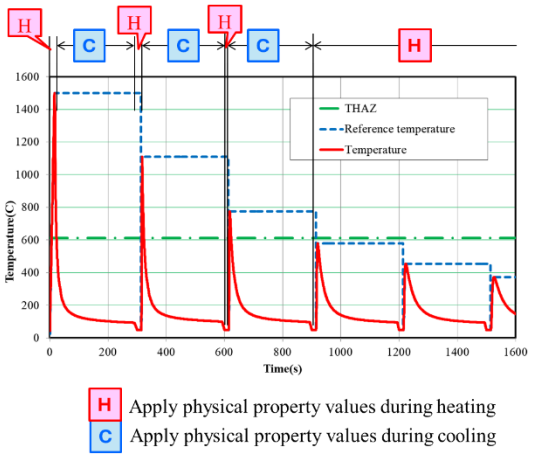

Fig. 2.4. Material properties strategy for phase transformation material simulation.

Considering the simulation precision, the mesh size sensitivity analysis based on the thermal analysis was carried out. The test object is a WAAM pipe part with 20 layers deposited and the details of simulation parameters are given in Chapter 3. Only the mesh sizes and temperature history results are discussed here. Table 2.1 displays the four different mesh conditions for the same object and Fig.2.5 shows the images of each case.

Table 2.1. The finite element model information of four meshes.

	Coarse mesh	**Simulation mesh**	**Fine mesh 1**	**Fine mesh 2**
Element type	Solid	Solid	Solid	Solid
Node number	17339	26555	100463	193657
Element number	13312	21760	87040	174080
Mesh size (mm)	1.3~4.2	0.6~4.2	0.6~2.1	0.3~2.1

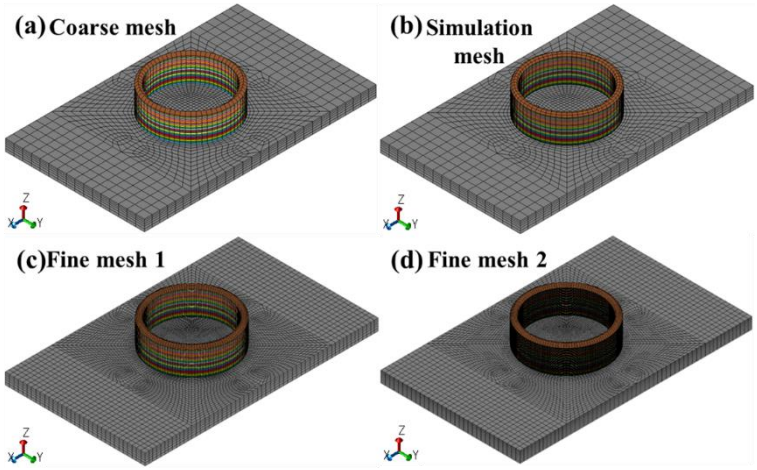

Fig. 2.5. The diagrams of the finite element model: (a) coarse mesh; (b) simulation mesh; (c) fine mesh 1; (d) fine mesh 2.

The history maximum temperature contours and temperature history curves at the 1st layer were plotted in Fig. 2.6 and Fig. 2.7. In the coarse mesh case, the temperature distribution shows significant non-uniformity and the maximum temperature is apparently higher than in the other three cases. For fine mesh 1, fine mesh 2, and simulation mesh, the temperature-time curves are almost consistent with each other. This means the simulation mesh is suitable for finite element analysis. Therefore, the fine mesh size for the deposition layer in chapters 3,4, and 5 will be controlled between 0.5~1.0 mm to ensure the simulation accuracy and efficiency at the same time.

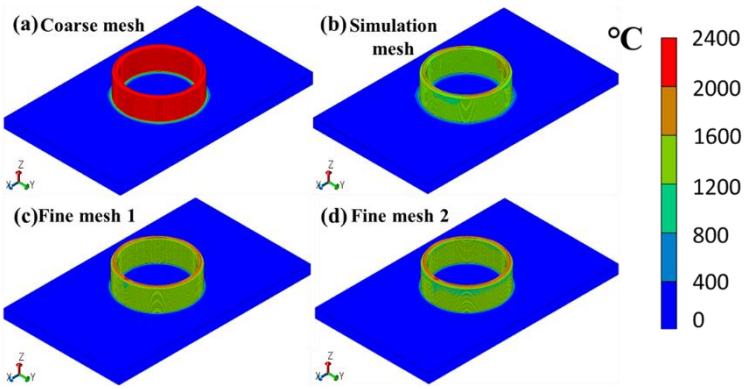

Fig. 2.6. History of maximum temperature contours: (a) coarse mesh; (b) simulation mesh; (c) fine mesh 1; (d) fine mesh 2.

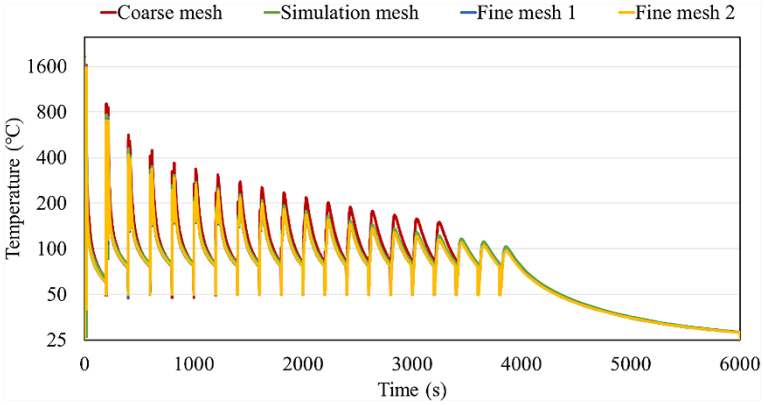

Fig. 2.7. Temperature-time curves of 1st layer under four mesh conditions.

Chapter 3. The characteristics of residual stress distribution in wire and arc additive manufactured two typical parts of stainless steels

3.1. Introduction

Residual stress distribution in the WAAM is of great importance due to its high relevance to the performance. However, the residual stress distribution may change due to the deposition variables and the relationship between them has not been thoroughly studied and understood. In this study, stainless steels 308LSi and 304 were used as WAAM feedstock and substrate, respectively, for additive manufacturing of two typical structures, namely wall and pipe structures. A thermomechanical coupling analysis model for WAAM was developed to investigate the formation mechanism of residual stresses in both structures, and their relationship with the deposition height and shape. The validity of the analysis was evaluated by comparing the simulated residual stresses with those measured by the contour method. The tensile longitudinal residual stress exists on the WAAM top surface and has the largest value at the position of several layers below the top surface. Regardless of wall or pipe structure, the distribution pattern of the longitudinal residual stress is tensile in the layers near the top surface, compressive in the layers near the substrate surface, and tensile near the bottom surface of the substrate. This distribution pattern reaches a quasi-stable state when the total deposition height is greater than a certain size. The maximum tensile residual stress is about 300MPa in both structures. For pipe structure, however, the residual stress distribution in the pipe model is not symmetric along the height direction. This analysis model provides a new guidance

for fast and accurate prediction of residual stresses for large-scale WAAM components in the future.

3.2. Experiment methods

3.2.1. Fabrication of WAAM components

Two typical WAAM components (i.e., MODEL-I and MODEL-O) were manufactured by WAAM using SUS308LSi as the feedstock, as shown in Figs. 1 and 2. MODEL-I was a wall structure additively manufactured on a SUS304 substrate (Fig.3.1(a)), consisting of 12 deposition layers with dimensions of 125 × 10 × 25.2 mm3 (Fig.3.1(b)). The WAAM parameters were 149 A for current and 14.5 V for voltage, respectively. The arc moving velocity was 250 mm/min with a transverse wave of 2 Hz frequency and 8 mm amplitude (Fig.3.1(c)). The temperature between each pass was kept below 150 ℃. MODEL-O was a pipe structure with 20 layers with a radius of 40 mm, a thickness of 6 mm, and a height of 27 mm, deposited on a SUS304 substrate (Fig.3.2(a) and (b)). The arc current, voltage, and moving velocity were 168 A, 20.5 V, and 1000 mm/min, respectively. The deposition path can be seen clearly in Fig.3.2(c), and each layer was deposited when the inter-pass temperature was lower than 50 °C.

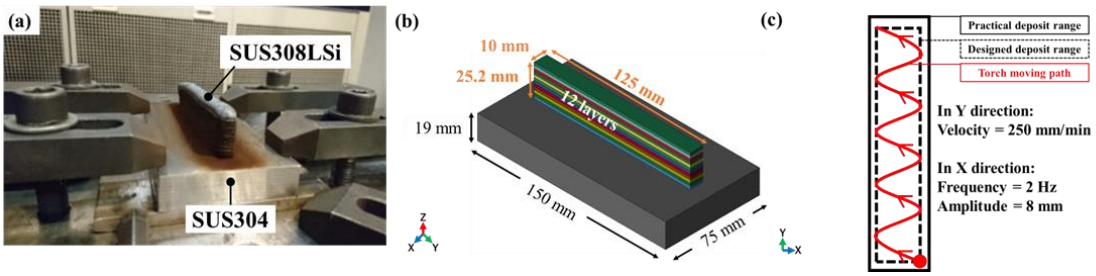

Fig. 3.1. Details of WAAM component MODEL-I: (a) actual component, (b) dimensions, (c) deposition path.

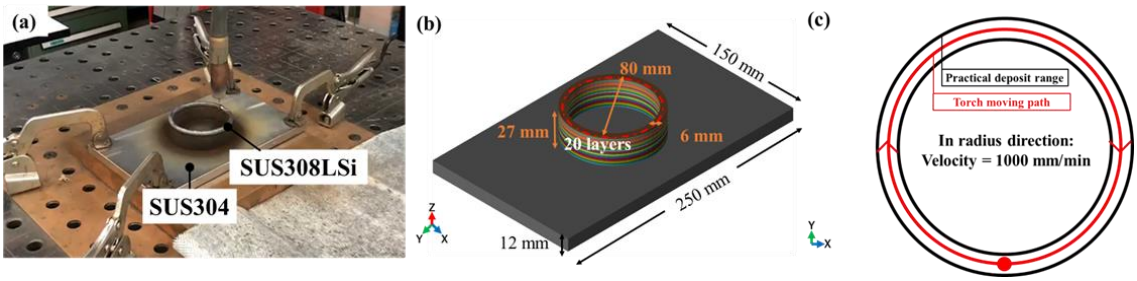

Fig. 3.2. Details of WAAM component MODEL-O: (a) actual component, (b) dimensions, (c) deposition path.

3.2.2. Residual stress measurement by contour method

The contour method was adopted for mapping residual stress distribution in both WAAM components. The diagram, Fig.3.3, displays the processing steps. Taking MODEL-I as an example (Fig.3.3(a)), the specimen was cut into two sections along the plane of interest (Fig.3.3(b)) using wire electrical discharge machining (WEDM). The residual stress was released by elastic deformation. The deformed contours of the two cut surfaces were measured using a KEYENCE VR5000 (Fig.3.3(c)). The contour data were smoothed (Fig. 3(d)) and then used in the established finite element (FE) model (Fig.3.3(e)) to calculate the residual stress. In this step, the common modeling method is to create a geometrically simplified FE model. The mapping from the contour data to the restructured surface would fail at some places due to the shape error, resulting in the calculation error for the residual stress. Therefore, the FE model in this study was built based on the actual surface profile to ensure the calculation accuracy using the contour method. Consequently, the residual stress distribution on the plane of interest could be obtained, as shown in Fig.3.3(f).

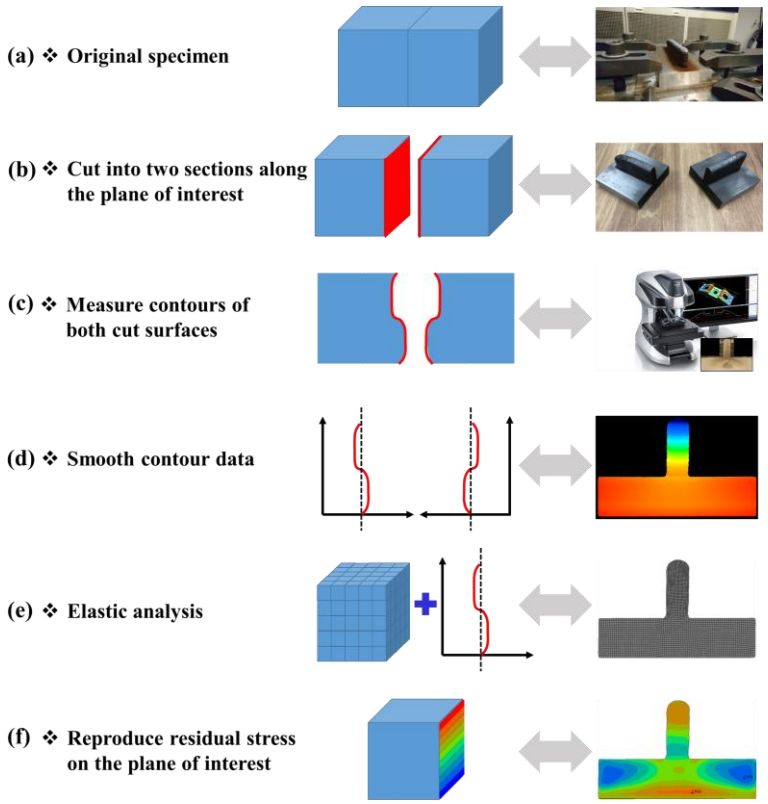

Fig. 3.3. Schematic representation of residual stress measured by the contour method.

Fig.3.4 and 3.5 compare the measured and restructured surfaces for both typical WAAM structures, respectively. It can be seen that the profiles are almost identical. To ensure the mapping quality, the mesh size of the FE model, which was used for the contour method to calculate the residual stresses, was 0.5 mm.

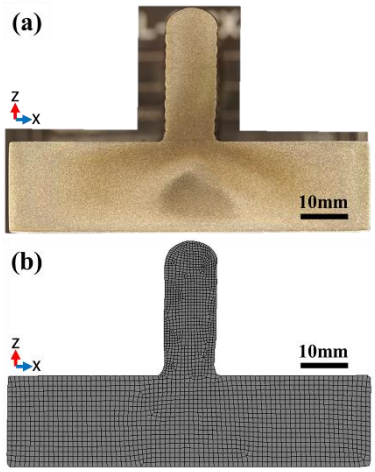

Fig. 3.4. Comparison of (a) measured and (b) restructured surfaces of MODEL-I.

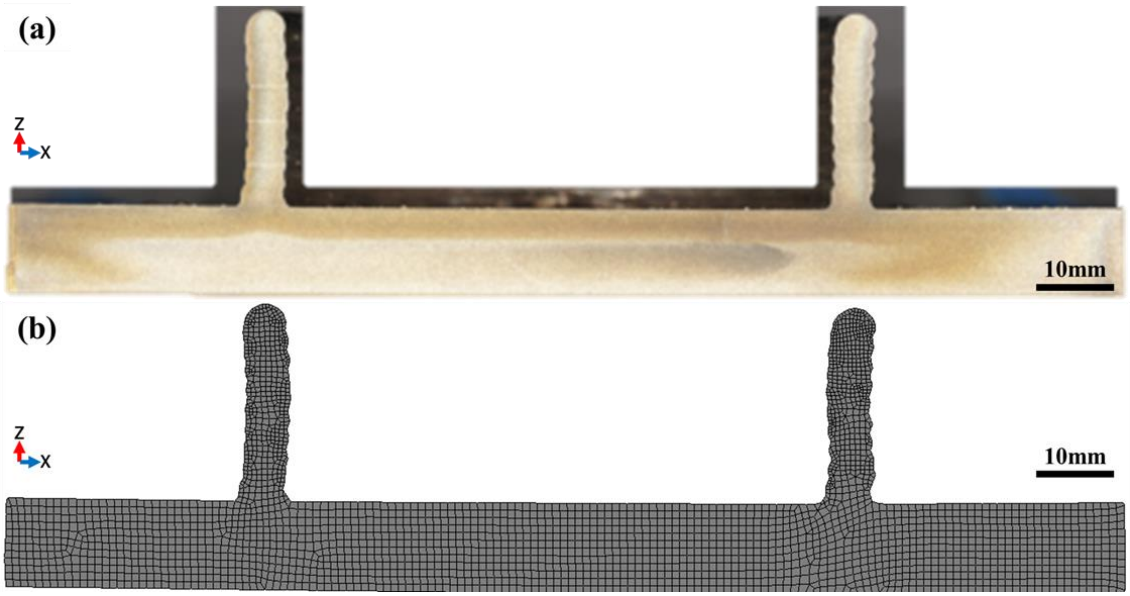

Fig. 3.5. Comparison of (a) measured and (b) restructured surfaces of MODEL-O.

3.3. Numerical modeling

3.3.1. Geometry modeling and boundary conditions

The WAAM simulations were performed using the in-house software JWRIAN-Hybrid[156]. Fig.3.6 and 3.7 show the geometry and meshing of MODEL-I and MODEL-O, respectively. Both were modeled based on the actual dimensions and meshed with 8-node fully integrated hexahedral solid elements. The deposition layers and contact region of the substrate (Fig.3.6(a) and Fig.3.7(a)) were meshed with a uniform size, and a sparse and dense transition mesh was used to reduce the computational cost, as shown in Fig.3.6(b) and Fig.3.7(b). For MODEL-I, there were 42924 nodes and 36208 elements, and the minimum mesh size was 0.525 mm. The MODEL-O meshes were scattered outward from the substrate center and sparsely arranged according to the thickness of the substrate. In MODEL-O, the number of nodes and elements were 26555 and 21760,

respectively. Similarly, a uniform mesh was used in the deposition layers and in the substrate region of interest. The minimum mesh size was 0.675 mm.

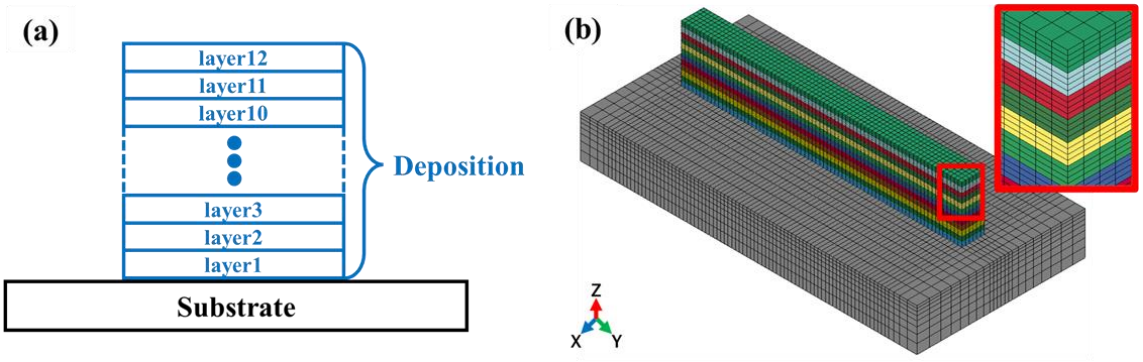

Fig. 3.6. (a) Deposition layers, (b) geometry, and meshing in WAAM models for MODEL-I.

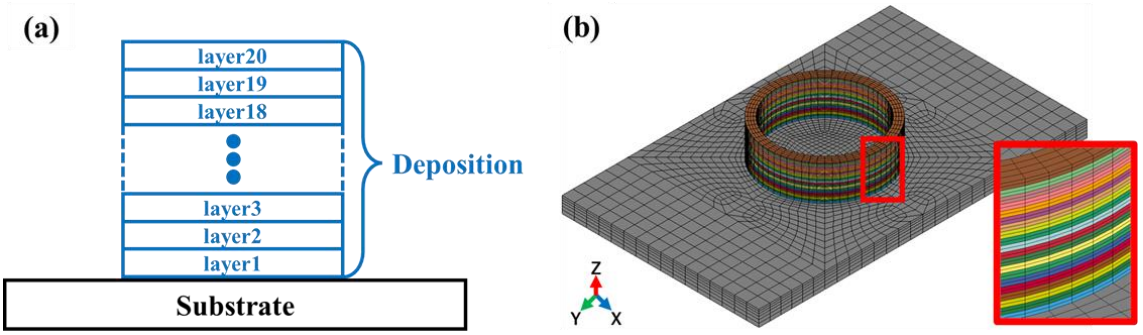

Fig. 3.7. (a) Deposition layers, (b) geometry, and meshing in WAAM models for MODEL-O.

In the actual experiment, four jigs were used to fix the substrate on the working plate during deposition, and they were released after the deposition was completed. Accordingly, the imposition of the boundary conditions in the WAAM model was divided into two stages, as shown in Fig.3.8 and 3.9. In the first stage, the role of the jigs was considered until all layers were deposited (Fig.3.8(a) and Fig.3.9(a)). In the second stage, the jig boundary condition was removed and replaced with a three-point boundary condition (Fig.3.8(b) and Fig.3.9(b)).

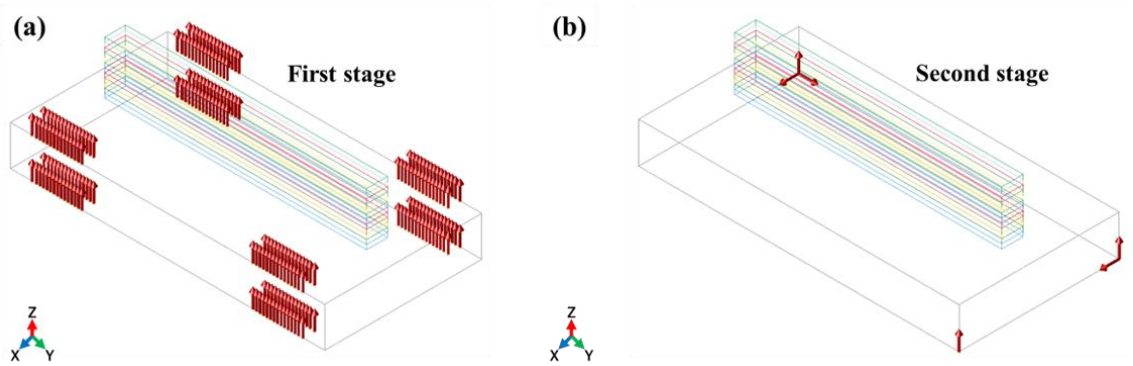

Fig. 3.8. Boundary conditions in WAAM models for MODEL-I: (a) first stage, (b) second stage.

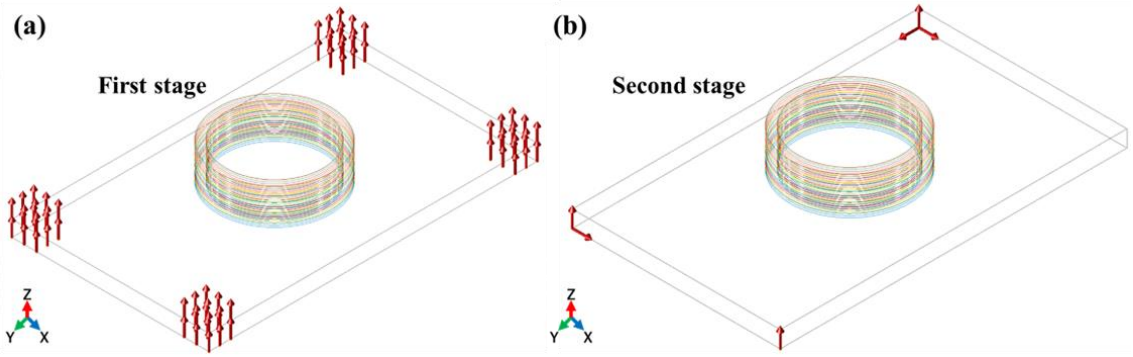

Fig. 3.9. Boundary conditions in WAAM models for MODEL-O: (a) first stage, (b) second stage.

3.3.2. Material properties and heat source model

In the thermal analysis, the density, specific heat, thermal conductivity, and coefficient of thermal expansion of the SUS308LSi deposition layers were measured by our research group. All thermal properties of the SUS304 substrate are publicly available[157]. All temperature-dependent thermal properties except the coefficient of thermal expansion are shown in Fig.3.10.

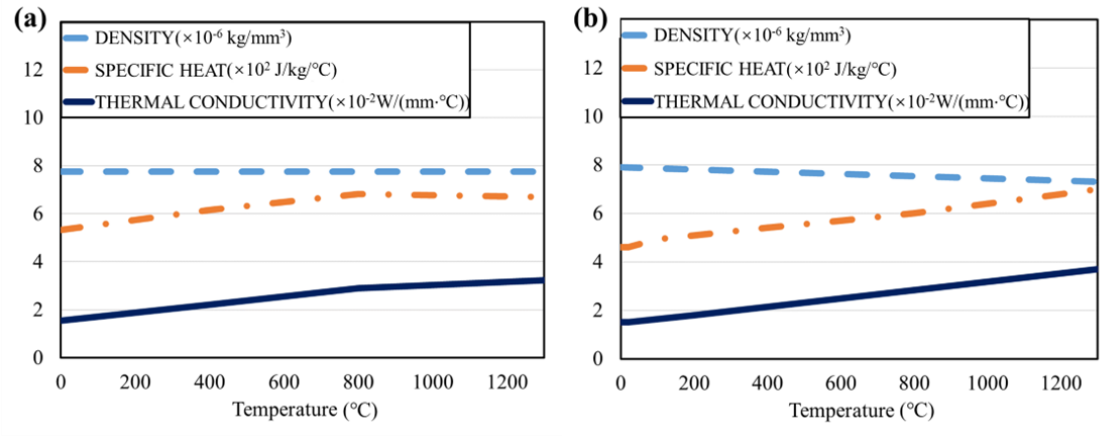

Fig. 3.10. Temperature-dependent thermal properties: (a) SUS308LSi, (b) SUS304.

An elastoplastic material model was used for the mechanical analysis. The Young's modulus, Poisson's ratio, yield stress, strain hardening, and coefficient of thermal expansion of SUS308LSi and SUS304 are required. All the mechanical properties are temperature-dependent and are measured from 0 to 1300 °C, assuming that they remain constant above 1300 °C, as shown in Fig.3.11.

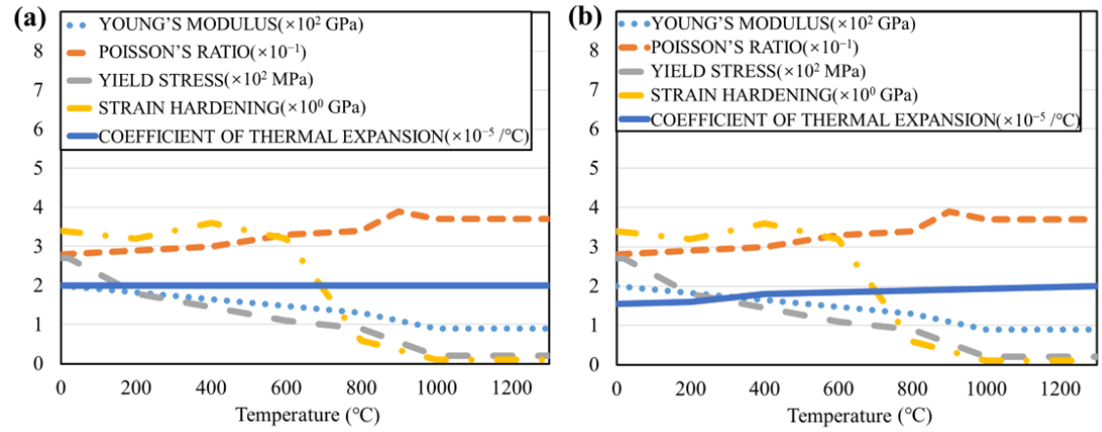

Fig. 3.11. Temperature-dependent mechanical properties: (a) SUS308LSi, (b) SUS304.

Based on the actual experiment, the current, voltage, and velocity of the torch (Section 3.2.1) were applied to the WAAM models. A hemispherical heat source with Gaussian heat distribution in the longitudinal, transverse, and thickness directions, suitable for MODEL-I and MODEL-O, was chosen and described by the following formula:

$$qv = \eta IU \frac{6\sqrt{3}}{\pi\sqrt{\pi}abc} exp\left(-\frac{3x^2}{a^2}\right) exp\left(-\frac{3y^2}{b^2}\right) exp\left(-\frac{3z^2}{c^2}\right) \quad \text{Eq.3.1}$$

where qv denotes the heat source intensity, IU indicates the heat power, η represents the heat efficiency, as well as power *2a*, *2b*, and *c* refer to the length, width, and depth of the heat source, respectively. It is worth noting that for MODEL-I, the trajectory of the heat source is wave-like (Fig.3.1(c)). The wave path requires the implementation of fine meshes, which increases the number of elements and makes the computation expensive. Moreover, it is difficult for a single heat source to cover a wide melting zone and keep the maximum temperature within an acceptable range. Therefore, an equivalent parallel double heat source is proposed in this study to describe the wave path, as shown in Fig.3.12.

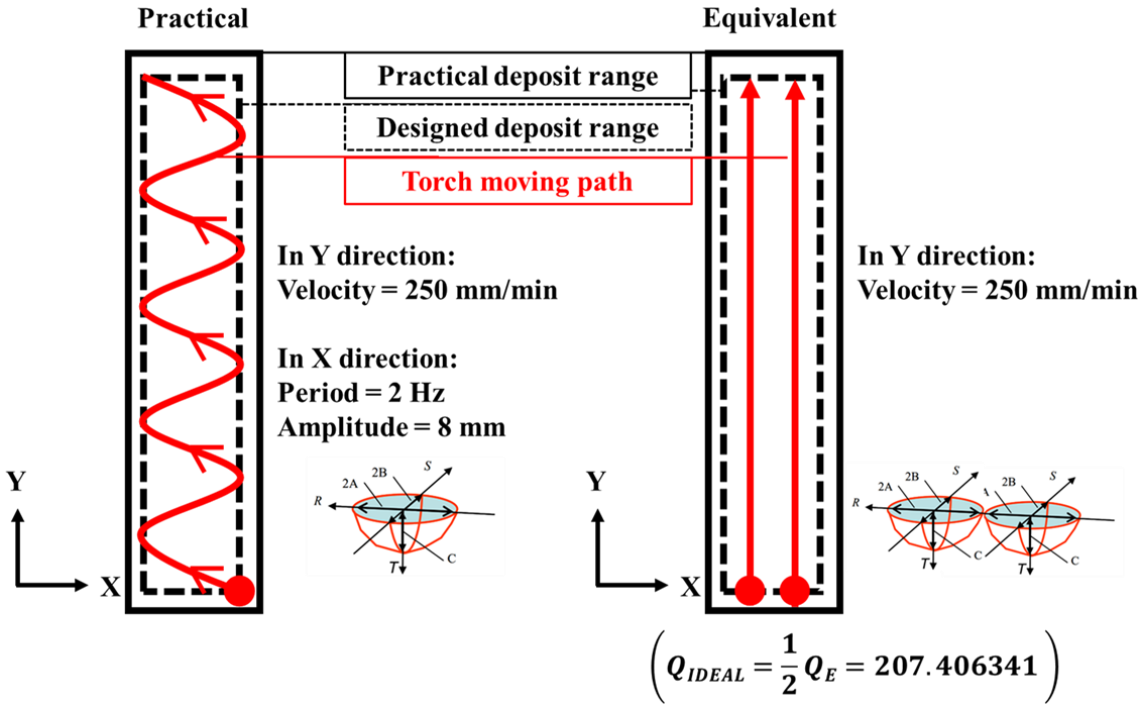

Fig. 3.12. Schematic representation of actual and equivalent parallel double heat source heat sources.

The equivalent parallel double heat source was implemented as follows: The actual heat source was divided into two identical parallel heat sources, each with half of the original heat. The two identical parallel heat sources maintained the same velocity as that of the actual heat source in the Y direction. To demonstrate their validity, single-pass WAAM simulations were performed based on the actual heat source and the equivalent heat source (i.e., the equivalent parallel double heat source and the equivalent single heat source, respectively), as shown in Fig.3.13.

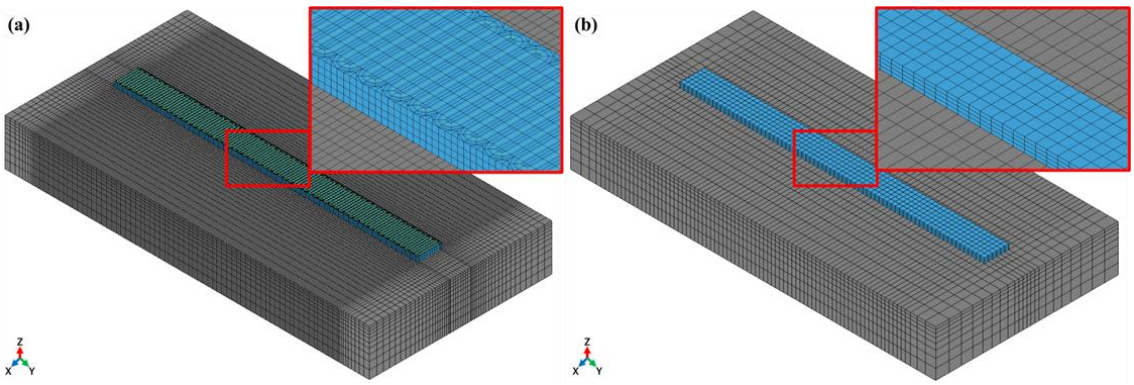

Fig. 3.13. Single-pass WAAM models based on the (a) actual and (b) equivalent parallel double (or single) heat sources.

Fig.3.14 compares the temperature fields with the three heat sources. Red and green represent the melting zone and heat-affected zone, respectively. Both the actual melting zone and heat-affected zone can be accurately reproduced by the equivalent parallel double heat source, which can be clearly seen by comparing Fig.3.14(a) and (b). However, the melting zone based on the equivalent single heat source (Fig.3.14(c)) is significantly different from the actual melting zone, indicating that the wave parameters cannot be directly ignored. The equivalent single heat source is the same as the actual heat source, but the wave parameters are not considered. Thus, the effectiveness of the equivalent parallel double heat source was demonstrated and could be applied in this study.

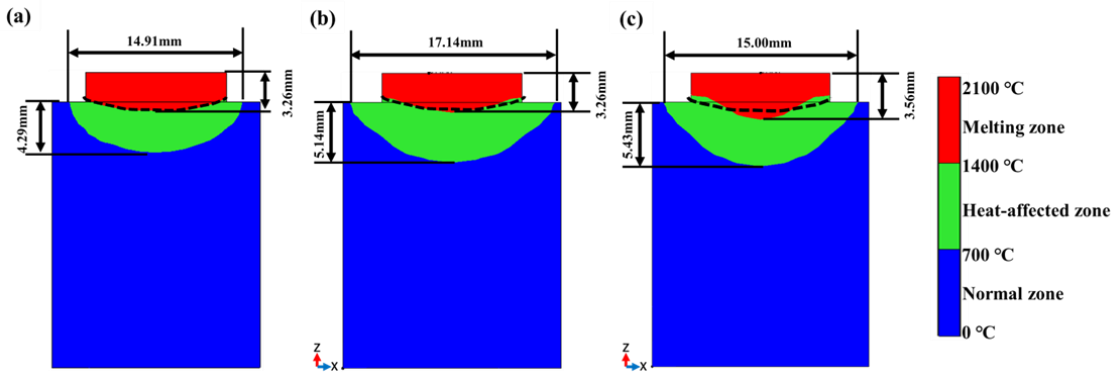

Fig. 3.14. Comparison of temperature fields using the (a) actual heat source, (b) equivalent parallel double heat source, and (c) equivalent single heat source.

3.4. Results and discussions

3.4.1. Experimental results and validation

The contour data of MODEL-I and MODEL-O were input into the contour method calculation program developed by our research group. The residual stress distribution perpendicular to the cut surface was evaluated. Fig.3.15 and 3.16 show the height distributions and the corresponding residual stress distributions for MODEL-I and MODEL-O, respectively.

In MODEL-I, the surface height increases gradually from top to bottom, and the distribution is left-right symmetric (Fig.3.15(a)). Accordingly, tensile residual stress is mainly present near the top of the deposition layers, with a decreasing trend from top to bottom (Fig.3.15(b)). The residual stress distribution is also left-right symmetric. However, the residual stress distribution in the substrate is different. The tensile residual stresses are mainly concentrated near the bottom of the substrate, while the compressive

residual stresses occur on the left and right sides of the substrate. The maximum residual stress in the deposition layer is 300 MPa.

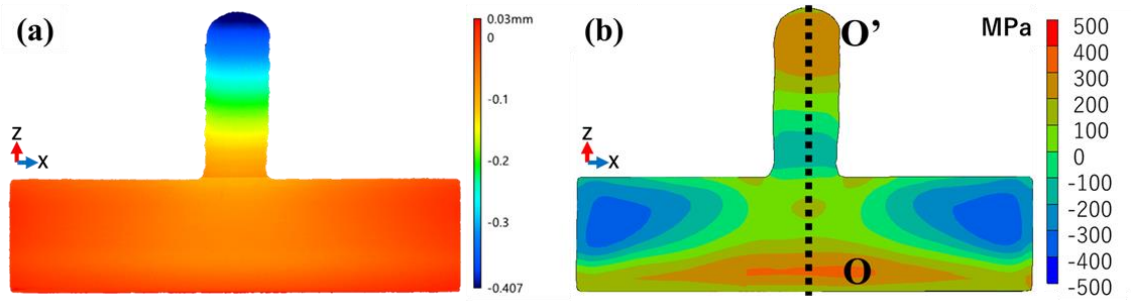

Fig. 3.15. (a) Height distribution and (b) residual stress distribution measured with the contour method for MODEL-I.

Fig.3.16(a) shows the height distribution of MODEL-O; like MODEL-I, the surface height of the deposition layers increases from top to bottom. The overall distribution is symmetrical. However, the surface height of the inner diameter is slightly higher than that of the outer diameter. In the substrate, the surface height decreases from top to bottom. Therefore, the residual stress is distributed symmetrically in the circumferential direction as a whole (Fig.3.16(b)). Tensile residual stresses occur near the top of the deposition layers and decrease along the height direction, whereas compressive residual stresses decrease from the outside to the inside. Compressive and tensile residual stresses occur in the upper and lower halves of the substrate, respectively. The maximum residual stress in the deposition layers is 295 MPa.

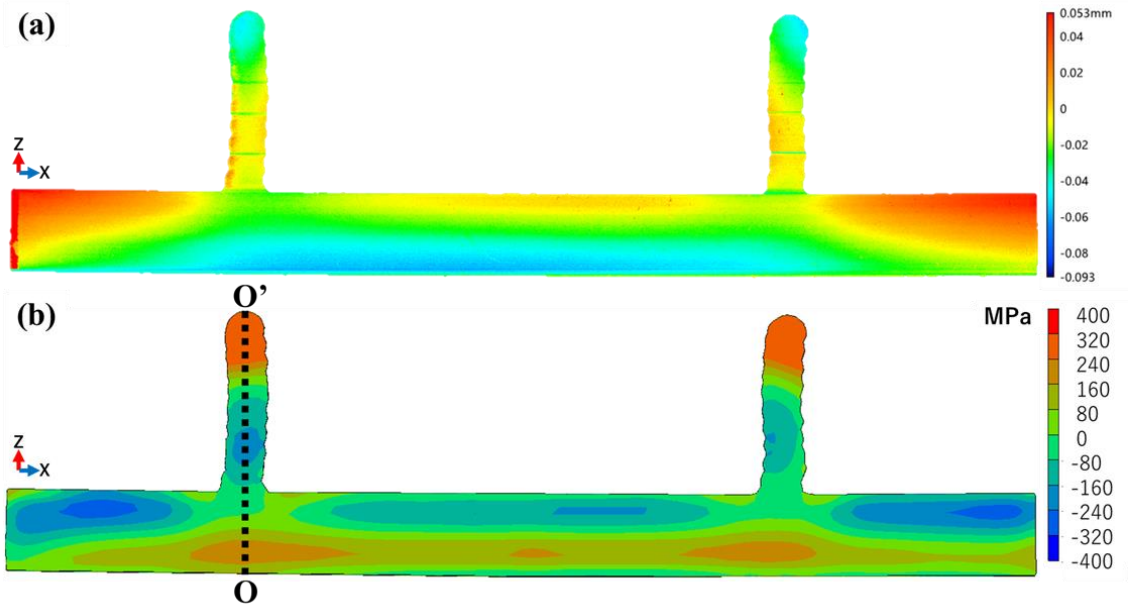

Fig. 3.16. (a) Height distribution and (b) residual stress distribution measured with the contour method for MODEL-O.

Residual stress distribution can be measured by the contour method, but its formation mechanism cannot be revealed experimentally. It is necessary to investigate it with WAAM simulations. Before that, experimental validation is essential. For validation, the residual stresses on O'–O of MODEL-I and MODEL-O were extracted from the measurements and WAAM simulations, respectively. The comparison results are shown in Fig.3.17 and 3.18, respectively. Regardless of MODEL-I or MODEL-O, the simulated residual stress distribution is consistent with the measured one. For MODEL-I (Fig.3.17), there is tensile residual stress at the top of the deposition layers. Along the height direction, the tensile residual stress continues to increase to 300 MPa, then decreases, and finally converts into compressive stress near the bottom of the deposition layers. The compressive residual stress converts to tensile residual stress and then slightly decreases from the top to the bottom of the substrate. The residual stress distribution of O'–O on MODEL-O (Fig.3.18) is similar to that of O'–O of MODEL-I (Fig.3.17). Tensile residual

stress prevails at the top of the deposition layers, which further increases to 300 MPa, then decreases to compressive stress, and finally increases to tensile stress along the height direction of MODEL-O. However, in contrast to MODEL-I, MODEL-O exhibits a greater proportion of compressive residual stress in the deposition layers. As a note, the simulated and measured residual stress curves cannot be completely overlapped due to the unavoidable thickness deviation of each deposition layer in the WAAM simulations and the actual experiments. The thickness of each layer was set the same in the simulation but inevitably varied slightly in practice.

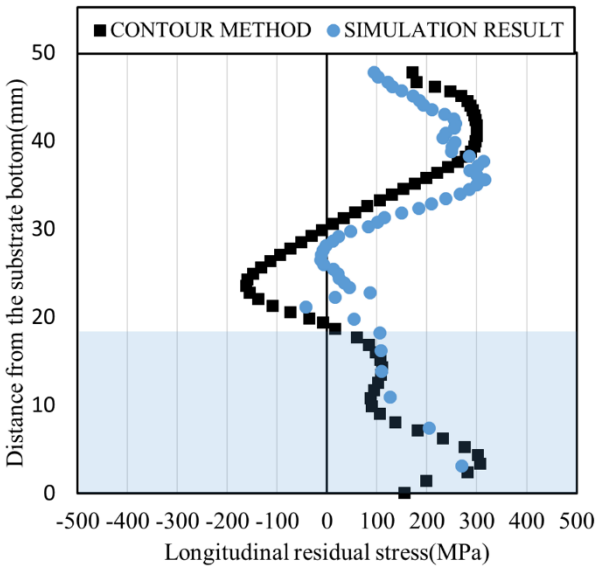

Fig. 3.17. Comparison of residual stress distribution on O'–O measured with the contour method and simulated with WAAM models in MODEL-I.

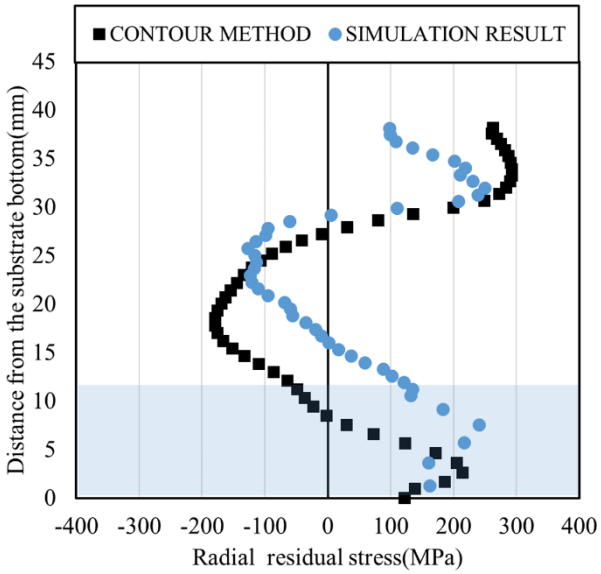

Fig. 3.18. Comparison of residual stress distributions measured with the contour method and simulated with WAAM models in MODEL-O.

3.4.2. Formation mechanism of residual stress

3.4.2.1. MODEL-I

Fig.3.19 shows the temperature fields of MODEL-I. The transient temperature distribution after deposition of the first layer (i.e., layer1) shows that both the deposition layer and a small portion of the substrate melted, indicating an effective joining between them, as shown in Fig.3.19 (a). Moreover, the joining between each deposition layer was confirmed by checking the transient temperature distribution after the deposition of layer2, layer3, …, layer12. An example in Fig.3.19 (b) shows the transient temperature distribution after the deposition of layer4. Finally, the history of the maximum temperature distribution in Fig.3.19 (c) shows that all deposition layers have reached a molten state, which is consistent with the experimental result.

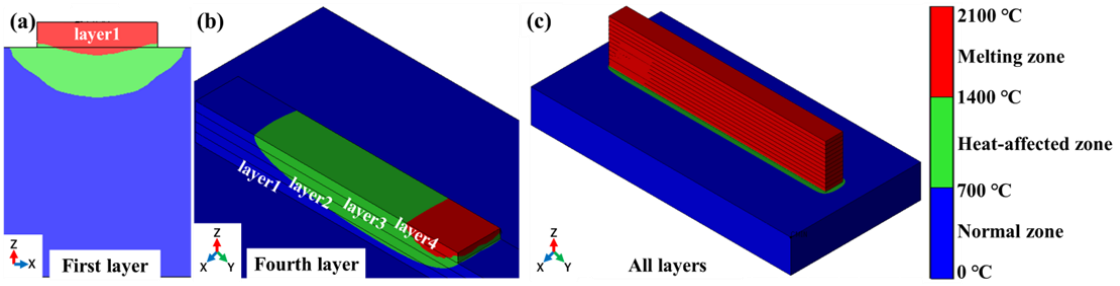

Fig. 3.19. Transient temperature distributions after depositing the (a) first and (b) fourth layers, and (c) history of maximum temperature distribution after depositing all layers in MODEL-I.

The overall and cross-sectional residual stress distributions in MODEL-I are shown in Fig.3.20. The overall distribution (Fig.3.20(a)) shows that the tensile residual stresses occur in the middle of the deposition layers and at the two ends of the first deposition layer, while the compressive residual stresses are mainly present near the two sides of the substrate and at the two ends of the last deposition layer. The overall distribution is symmetrical. The residual stress distribution on the cross-section (Fig.3.20(b)) is the same as that measured by the contour method (Fig.3.15(b) and Fig.3.17). The simulated and measured residual stress distributions are identical to ensure the accuracy of the simulation. The simulation results show that tensile residual stress occurs at the top of the deposition layers, which initially increases and then decreases to compressive stress near the bottom of the deposition layers. This distribution is left-right symmetric. The presence of tensile residual stress is attributed to the cooling shrinkage of molten SUS308LSi during the WAAM, whereas the maximum value is not at the top of the deposition layers because the constraint by the substrate gradually weakens with increasing deposition height. After the deposition of one layer, the melting and heat-affected zones covered two and four layers, respectively (Fig.3.19 (b)). Therefore, it is plausible that the maximum

tensile residual stress occurs in layer6–layer8 (Fig.3.20(b)). However, due to the stress balance, compressive residual stresses also occur near the bottom of the deposition layers. In the substrate, large tensile and compressive residual stresses occur near the bottom and top regions, respectively. This distribution is mainly due to the bending caused by the cooling shrinkage of the deposition layers (Fig.3.20(c)).

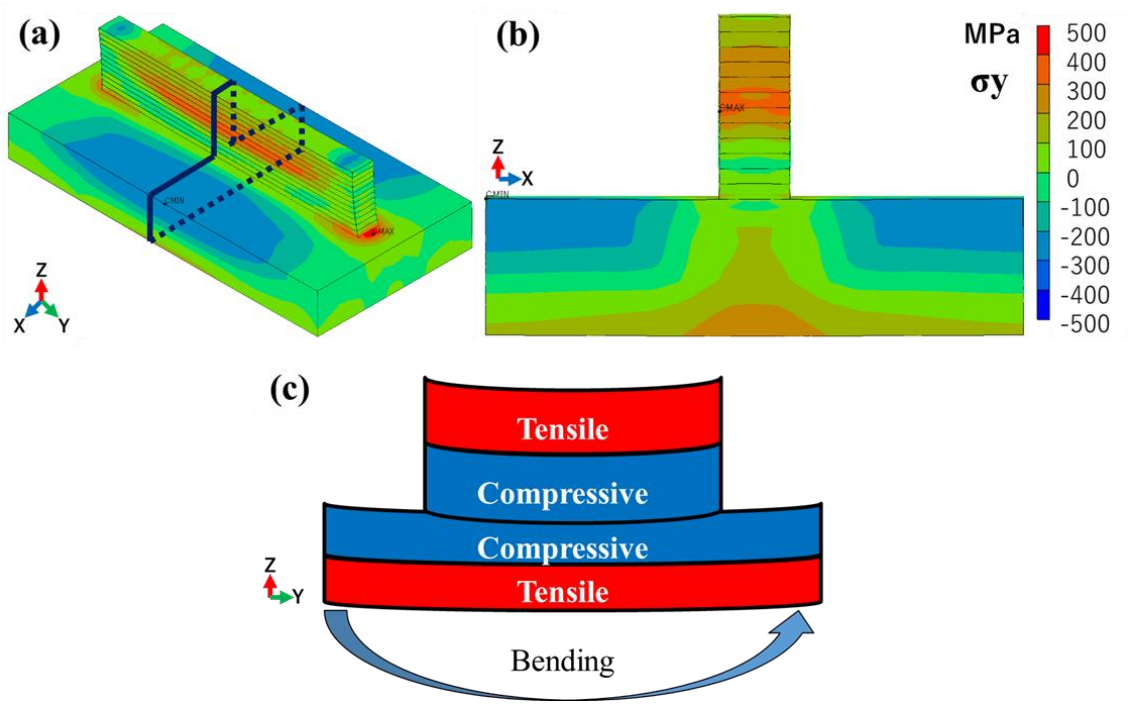

Fig. 3.20. Overall (a) and cross-sectional (b) residual stress distributions in MODEL-I. (c) A schematic diagram explaining the residual stress formation.

3.4.2.2. MODEL-O

Fig.3.21 shows the temperature fields of MODEL-O. The transient temperature distributions after depositing the first (Fig.3.21(a)) and fifth (Fig.3.21(b)) layers indicate that the heat input is sufficient for melting between the deposition layer and the substrate, as well as between adjacent deposition layers. In addition, all deposition layers reached the melting point during the WAAM process, as shown in Fig.3.21(c).

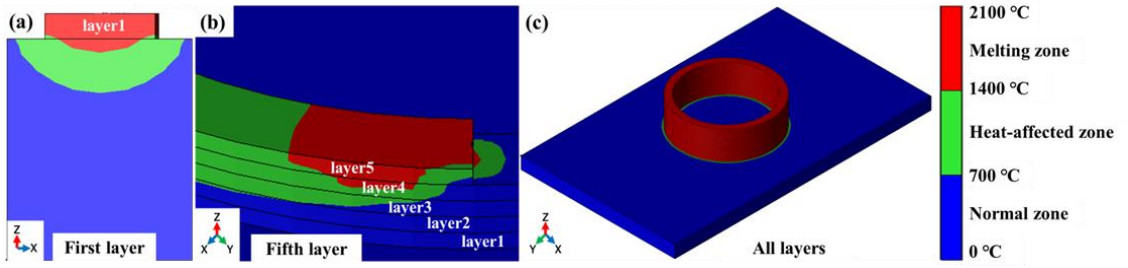

Fig. 3.21. Transient temperature distributions after the deposition of the (a) first and (b) fifth layers, and (c) history of maximum temperature distribution after the deposition of all layers in MODEL-O.

Fig.3.22 shows the overall and cross-sectional residual stress distribution in MODEL-O. The cross-section is at the same location as the measurement. Like MODEL-I, the overall distribution is symmetric (Fig.3.22(a)). The cross-sectional residual stress distribution is shown in Fig.3.22(b). As with MODEL-I, the tensile residual stress occurs at the top of the deposition layers, increasing to a maximum and then decreasing to compressive stress near the bottom of the deposition layers. The melting and heat-affected zones extend over two and three layers, respectively (Fig.3.21(b)), and it is plausible that the maximum tensile residual stress occurs in layer15–layer17 (Fig.3.22(b)). In the substrate, there are tensile and compressive residual stresses near the bottom and top regions, respectively. It is not repeatedly explained. However, this stress distribution in the deposition layers is asymmetric. In particular, the compressive residual stress is higher on the inner surface than that on the outer surface. The main reason for this is that although the inner and outer surfaces shrink together, the inner surface is compressed by the cooling shrinkage of the outer surface, resulting in additional compressive residual stress on the inner side. A simple example of this is shown in Fig.3.22(c). The outer radius and inner radius are defined as R+3 (mm) and R−3 (mm), respectively. The outer radius is

assumed to shrink to R+2 (mm), and the inner radius shrinks to R−4 (mm); therefore, the strains of both surfaces can be calculated as follows:

$$Strain_{outer} = \frac{2\pi(R+3)-2\pi(R+2)}{2\pi(R+3)} = \frac{1}{R+3} \quad \text{Eq.3.2}$$

$$Strain_{inner} = \frac{2\pi(R-3)-2\pi(R-4)}{2\pi(R-3)} = \frac{1}{R-3} \quad \text{Eq.3.3}$$

$$Strain_{outer} < Strain_{inner} \quad \text{Eq.3.4}$$

The strain on the inner surface is greater than that on the outer surface. Therefore, the inner surface was pressed by the outer surface, and compressive residual stresses were generated.

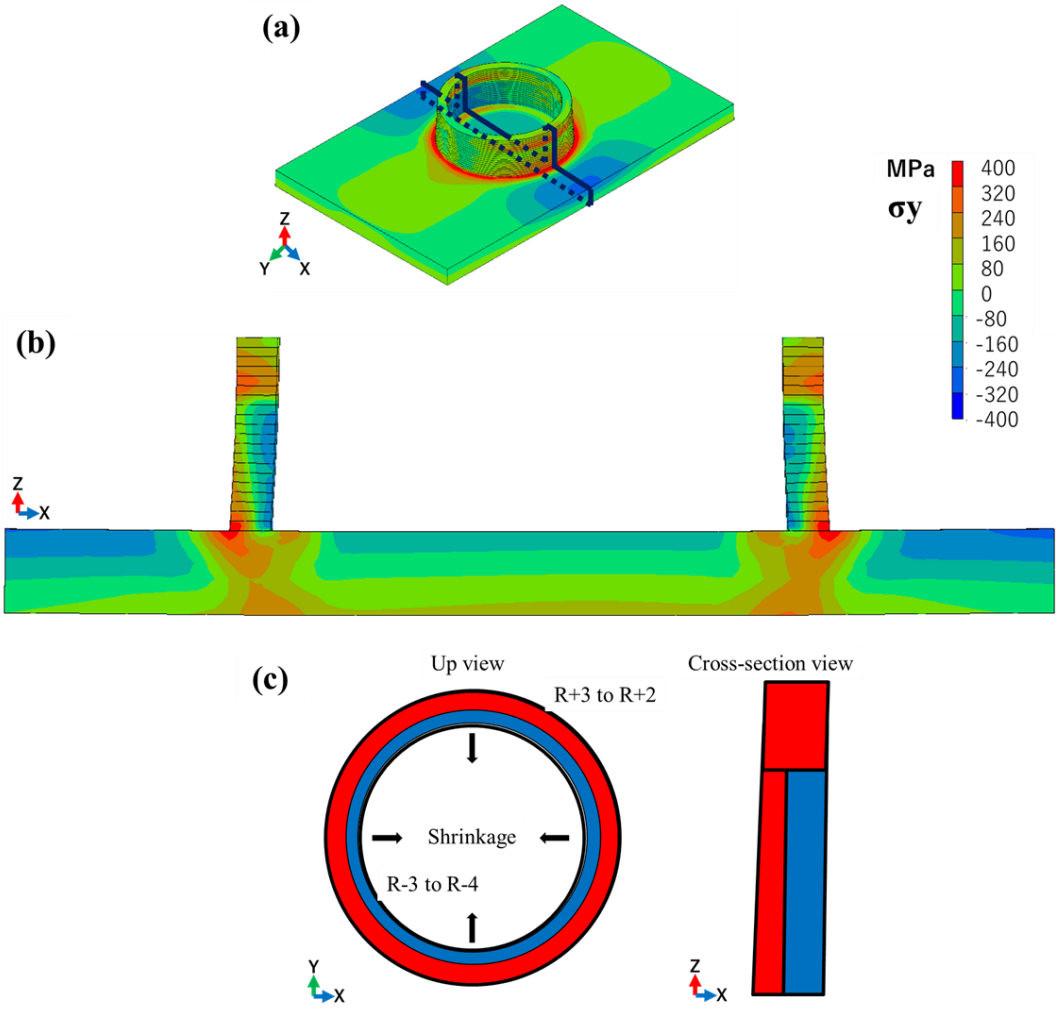

Fig. 3.22. Overall (a) and cross-sectional (b) residual stress distributions in MODEL-O. (c) A schematic diagram explaining the residual stress formation.

3.4.3. Distribution characteristics related to deposition variables

For WAAM, the residual stresses in the deposition layers are of interest. In particular, the variation pattern of residual stress as a function of deposition height and shape needs to be understood. This is of great importance for the fast and accurate calculation of residual stresses in future large-scale WAAM components. Therefore, the residual stress distributions were quantitatively analyzed after the deposition of each layer of MODEL-I or MODEL-O.

Fig.3.23(a) shows the residual stress distributions after depositing layer1, layer2, …, layer12 of MODEL-I. After the deposition of 1-layer, there is a uniform tensile residual stress of about 300 MPa in the deposition layers due to the constraints from the substrate. As the number of deposition layers increases, the uniform distribution breaks down. After the deposition of 2- to 7-layers, only tensile residual stresses occur, but the stress near the top decreases as the substrate constraint weakens. After depositing more than 7-layers, the tensile residual stress decreases near the bottom and even turns into compressive stress due to the stress balance. Releasing the jig leads to a decrease in the tensile residual stress at the top of the deposition layers and an increase in the tensile residual stress in the layer7. To explain this increase, we extracted the history of the von Mises stress, longitudinal stress, equivalent plastic strain, and temperature at the node in layer7, as shown in Fig.3.23(b). It is evident that both the von Mises stress and the longitudinal stress drop immediately after the jigs are released. In general, this trend continues until the end of the experiment. However, the transient temperature is still about 300 °C, indicating that layer7 continues to shrink during subsequent cooling, eventually causing an increase in tensile residual stress. The cooling shrinkage from 1200 to 6000 s is elastic, as the

equivalent plastic strain does not change. Consequently, the deposition height may affect the WAAM residual stress distribution. However, for MODEL-I, the tensile residual stress is present at the top and increases in some layers below, and this distribution pattern is independent of the deposition height.

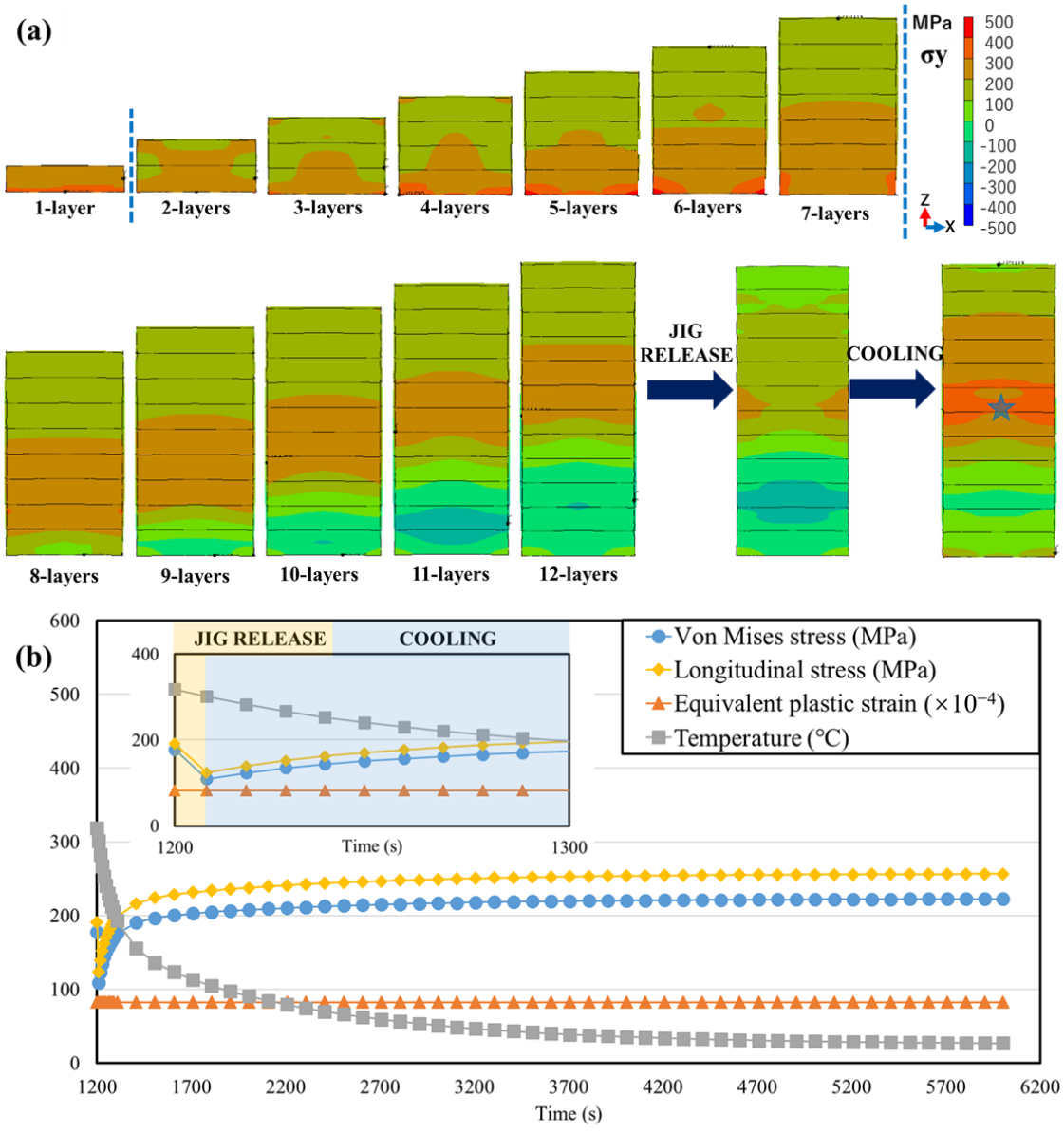

Fig. 3.23. (a) Residual stress distributions in MODEL-I after deposition from 1-layer to 12-layers, and subsequent jig release. (b) History variables at the node marked in Fig. 3.23(a).

To better understand the distribution characteristics in MODEL-I, the residual stresses on each central axis in Fig.3.23(a) are extracted, as shown in Fig.3.24. The detailed description is as follows: In all cases, the tensile residual stress occurs at the top of the deposition layers. For deposition height less than 15 mm (i.e., 7-layers), the residual stress increases from the top to the bottom but remains at 200–300 MPa. This distribution is no exception to the deposition of 1-layer. However, when the deposition height exceeds 15 mm, the residual stress first increases and then decreases from top to bottom. When the deposition height is sufficient to 20 mm (i.e., 9-layers), compressive residual stress can also occur. This suggests that, for MODEL-I, the tensile residual stress is present at the top and continues to increase inside the component, and this distribution pattern is independent of the deposition height. Moreover, the corresponding distribution region is identified within 15 mm below the top.

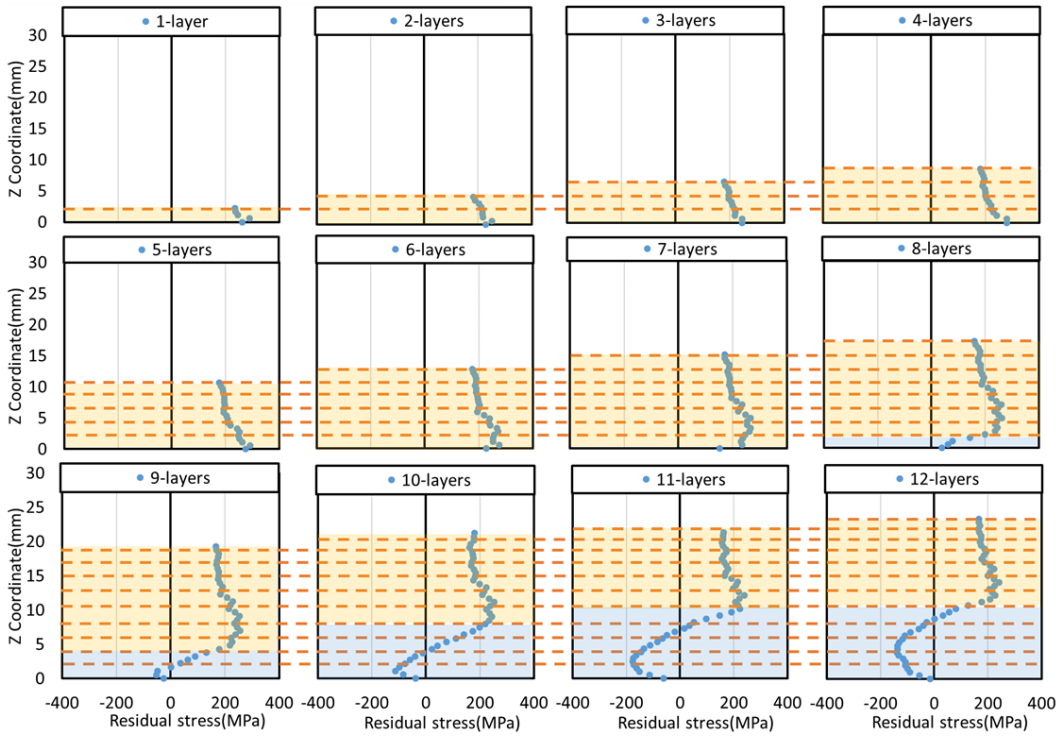

Fig. 3.24. Residual stresses on the central axis of MODEL-I after deposition from 1-layer to 12-layers, subsequently. They are extracted from Fig. 3.23(a).

Fig.3.25 shows the residual stress distributions after deposition of layer1, layer2, …, layer20 of MODEL-O. The variation of distribution characteristics is similar to that of MODEL-I. The tensile residual stress is present at the top of the deposition layers, which increases from top to bottom after deposition of 1- to 8-layers. After deposition of more than 8-layers, the tensile residual stress first increases and then decreases from top to bottom and can even turn into compressive residual stress. The effect of jig release is negligible. It is worth noting, however, that in contrast to MODEL-I, the compressive residual stress on the inside is significantly higher than on the outside as the deposition height increases. This difference is closely related to the deposition shape, as discussed in Section 3.4.2. Consequently, both deposition height and shape affect the WAAM residual stress distribution. An adequate deposition height results in compressive residual stresses in the deposition layer, while the deposition shape from the wall to the pipe results in an asymmetric distribution of residual stress. It should be noted that the tensile residual stress at the top of the deposition layers continues to increase inside the component, regardless of the deposition height and shape.

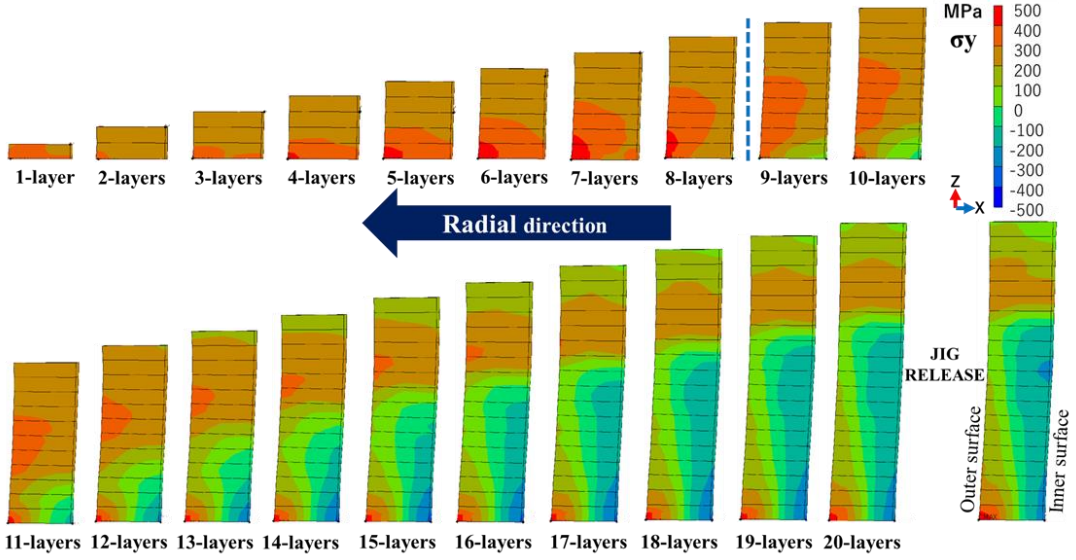

Fig. 3.25. Residual stress distributions in MODEL-O after deposition from 1-layer to 20-layers, and subsequent jig release.

To better understand the distribution characteristics in MODEL-O, the residual stresses on each central axis in Fig.3.25 are extracted, as shown in Fig.3.26. The comparison results show that the tensile residual stress increases from top to bottom for deposition height of less than 10 mm (i.e., 8-layers) and ranges from 200 to 300 MPa. This distribution is also observed for deposition heights greater than 10 mm within about 10 mm from the top. However, at a deposition height greater than 10 mm, the tensile residual stress decreases near the bottom and changes to compressive residual stress. This supports the assumption that the tensile residual stress exists at the top of the deposition layers and continues to increase towards the interior of the component, regardless of the deposition height and shape. Additionally, the corresponding distribution region in MODEL-O is identified to be within about 10 mm from the top surface.

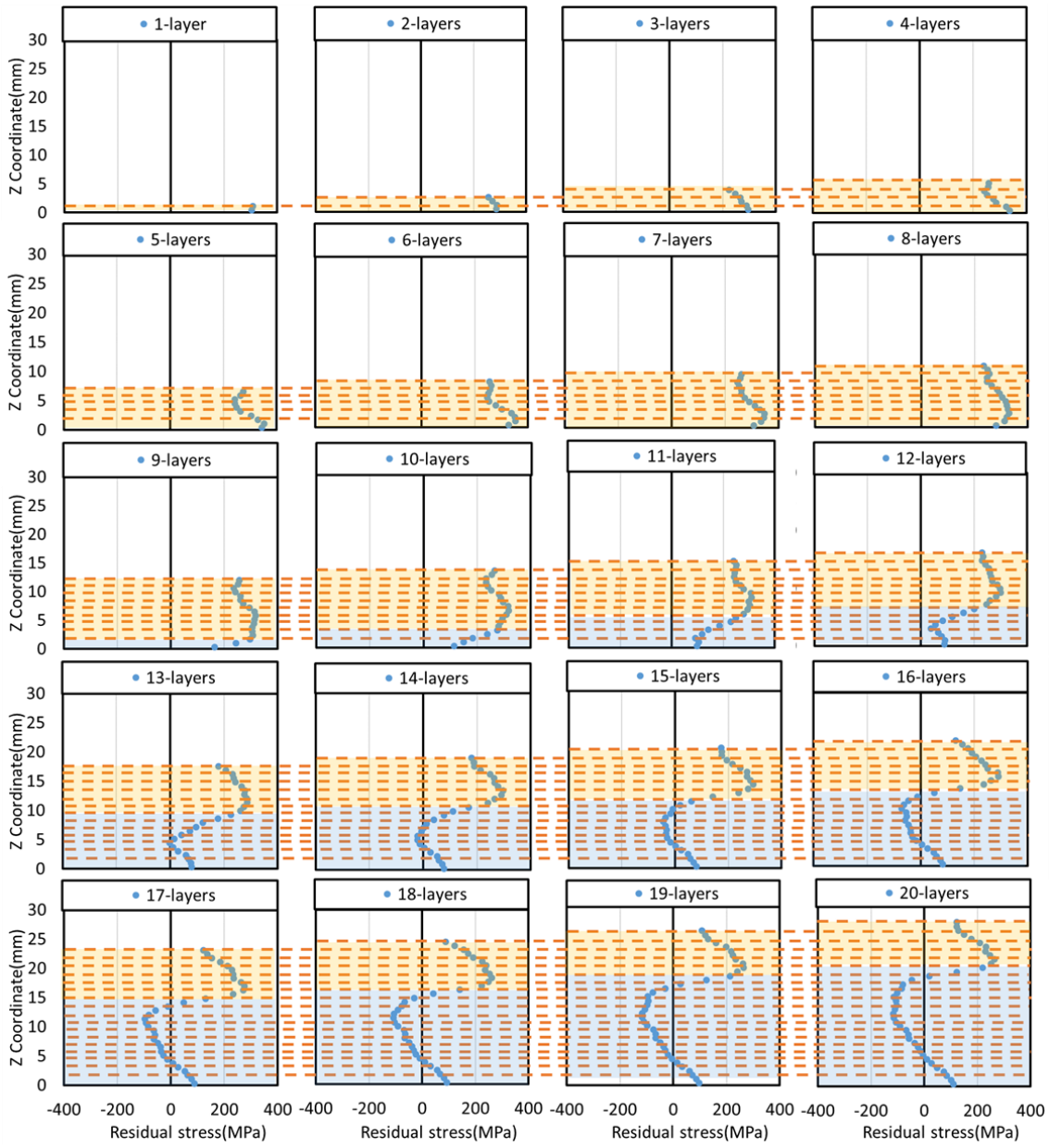

Fig. 3.26. Residual stresses on the central axis of MODEL-O after deposition from 1-layer to 20-layers, subsequently. They are extracted from Fig. 3.25.

3.5. Conclusions

In this study, two typical structures, i.e., a wall and pipe, were successfully fabricated by WAAM. A thermomechanical coupling WAAM model was developed to study the mechanism of residual stress formation and its relationship with the deposition height and shape. This forms the basis for residual stress accelerated calculation of future large-scale WAAM components. The main conclusions are as follows.

(1) The residual stress distributions in MODEL-I and MODEL-O were measured and reproduced by the contour method and the WAAM simulation respectively. The validity of the simulation result was evaluated by comparison with the stress measured by the contour method. In addition, an equivalent parallel double heat source was proposed to simplify the wave-like trajectory of the heat source, and it was proved to have good accuracy.

(2) Regardless of MODEL-I or MODEL-O, tensile residual stresses exist at the top of the deposition layers, reaching a maximum value (~300 MPa) at the position of several layers below the top, which is mainly attributed to the cooling shrinkage of the deposited materials and the constraint difference from the substrate. Tensile and compressive residual stresses occur in the substrate near the bottom and top regions, respectively, which are attributed to the bending of the substrate.

(3) When the deposition height is larger than a certain size (about 10 mm in the wall model and 15 mm in the pipe model), the distribution of the longitudinal residual stress reaches a quasi-stable state with a tensile-compressive-tensile pattern from the top of the deposition layers to the bottom of the substrate. However, when the deposition height is smaller than a certain size, there are only tensile residual stresses in the deposition layers.

Chapter 4. The study of residual stress due to wire and arc additive manufacturing using low transformation temperature material

4.1. Introduction

High heat input in wire and arc additive manufacturing (WAAM) tends to result in high tensile residual stress, which adversely affects performance and service reliability. However, low-transformation-temperature (LTT) materials are susceptible to compressive residual stresses due to their low phase-transformation point. Here, the LTT material 10Cr-10Ni was used as the deposited material to fabricate a pipe structure, and the contour method was applied to measure the residual stress distribution in the cross-section. A thermomechanical coupling analysis model was developed to investigate the residual stress generation mechanism in 10Cr-10Ni (LTT) during the WAAM process. The simulated deformation and residual stress distributions agree well with the measurements. Through simulation analysis of the deposition of different layers, we found the key to the generation of compressive residual stresses in the LTT layers lies in whether there is a transformation from austenite to martensite during the final thermal cycle. When the deposition height exceeded 5.405 mm (approximately four layers), compressive residual stresses were only generated in the last four LTT layers and transformed into tensile residual stresses in the other layers. This results in a concept called the effective region, which can be used as a guide for reducing stress in WAAM using LTT materials.

4.2. Materials and methods

4.2.1. Materials and WAAM process

A mature LTT material, 10Cr-10Ni, was selected as the deposition material for the WAAM process. The LTT welding wire was deposited on a 300 × 150 × 12 mm substrate made of SUS304. The four corners of the substrate were fixed to the working platform using jigs. The chemical compositions of the two materials and the phase-transformation temperatures of the LTT welding wire are listed in Table 4.1.

Table 4.1 Chemical compositions and the phase transformation temperature of 10Cr-10Ni (LTT).

	Chemical composition (mass%)									**Transformation temperature**	
	C	**Si**	**Mn**	**P**	**S**	**Ni**	**Cr**	**Mo**	**Nb**	**Start (°C)**	**Finish (°C)**
10Cr-10Ni	0.026	0.32	0.07	0.010	0.006	10.00	10.00	0.13	0.005	$M_s = 180$	$M_f < 0$
SUS304	0.08	1.00	0.19	0.045	0.03	8.00 ~10.50	18.00 ~20.00	-	-	-	-

The current, voltage, wire feed speed, and torch-moving speed were set to 149 A, 14.5 V, 6.5 m/min, and 16.667 mm/s, respectively. The deposition section consisted of 20 layers, and the torch path was a circle with a radius of 40 mm. The average thickness and width of each layer were 1.35 mm and 6 mm, respectively. Fig.4.1 shows an actual image of the WAAM specimen and a schematic diagram describing the dimensions of the substrate and deposition layer. The room temperature on the day of the experiment was 25 °C. To ensure that phase transformation could take place in all layers of the deposition

part, the temperature of the deposition part was controlled to below 50 °C before the next layer was deposited.

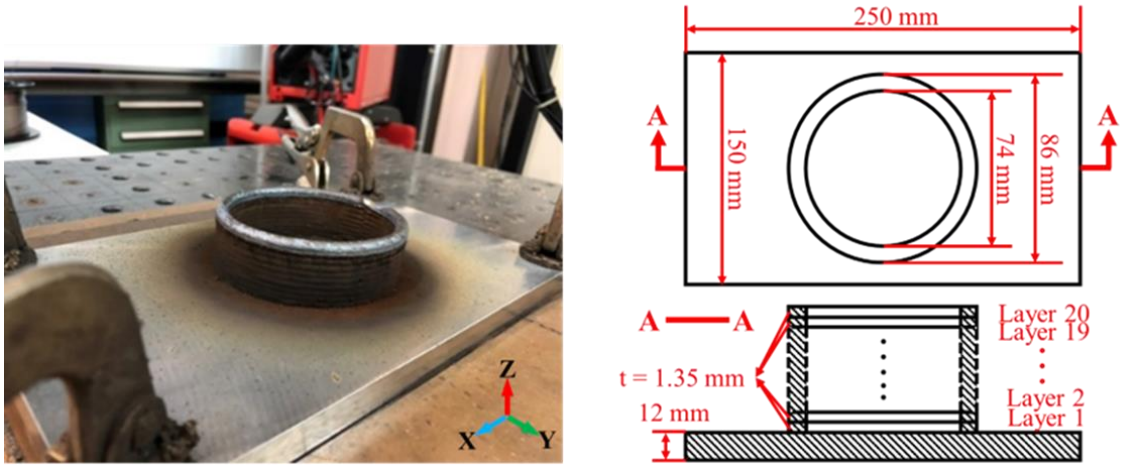

Fig. 4.1. The image of the WAAM specimen and its dimensions.

4.2.2. Measurement of the deformation

In the WAAM process, the large heat input caused by each deposition layer leads to deformation accumulation on the substrate; one of the main types of deformation is substrate bending. This has a significant effect on the shape accuracy of the deposited part. A Keyence VR5200 instrument was used to measure the deformation. The sampling interval was set to 0.1 mm to capture the surface height distribution of the substrate bottom surface. The two bottom surfaces of the substrate were measured separately, as the specimen was cut for contour measurements. The final substrate deformation after cutting was determined by stitching the two measurements.

4.2.3. Residual stress measurement

In circumferential additive manufacturing, the constraints in the circumferential direction are obviously stronger than in the other two directions. Therefore, the residual stresses in the circumferential direction are the major component and the most important aspect to be investigated. To measure this, the specimen was cut by wire electrical discharge machining (WEDM) at the symmetrical section, and the surface profiles of the cross-sections were measured directly by KEYENCE VR5000. The measurement interval was set to 0.1 mm. The measured data were then entered into the contour method program to calculate the residual stress.

4.3. Numerical modeling

4.3.1. Geometry modeling

In this study, the WAAM simulations were performed using the in-house software JWRIAN-Hybrid. The geometry and meshing of the finite element (FE) model are shown in Fig. 4.2. Our previous study showed that the deposited part shrank significantly in the height direction after WAAM [6]. The measured average height of each layer was 1.35 mm, and the shrinkage in the pre-simulation was 5.19%. Therefore, the average height of each layer in the FE model was set to 1.42 mm. The actual substrate sizes were created with the radius and width of 40 and 6 mm, respectively, for each deposition layer. Moreover, to express the geometry of the deposition part close to the practical shape, which is high in the middle and low on both sides, a curved surface was used as the interface between the deposition layers.

The model was meshed with a fully integrated 8-node hexahedral solid element with 26555 nodes and 21760 elements. For the deposition part, a fine mesh of 0.675 mm was used to ensure that the residual stress distribution characteristics of the 10Cr-10Ni (LTT) could be reproduced. In other areas, a coarse mesh was used to reduce the calculation time. The mesh convergence test was performed, and the result indicated the mesh size in this study was suitable. After the thermo-elasto-plastic analysis, the FE model with WAAM residual stress was cut into two pieces from the transverse section, and residual stress release analysis was conducted to obtain the deformed shape for comparison with the experimental one used in the contour method.

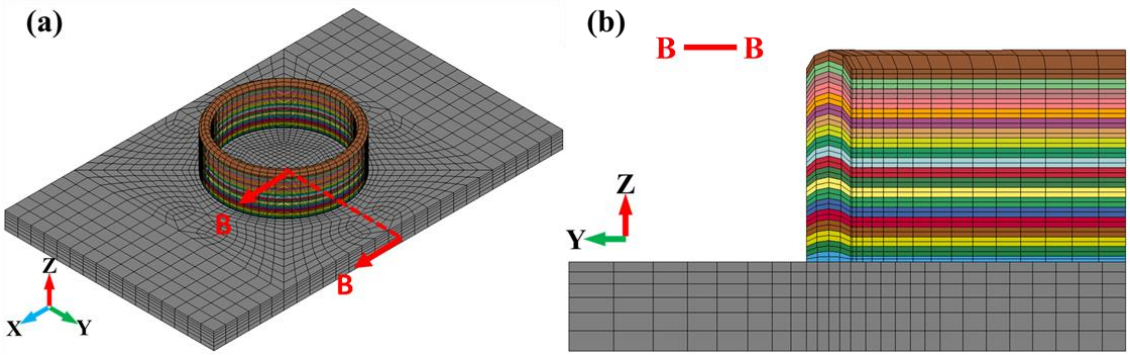

Fig. 4.2. The diagram of the FE model in thermo-elasto-plastic analysis: (a) geometry; (b) detailed cross-sectional meshing.

4.3.2. WAAM and boundary condition

WAAM was implemented using metal inert gas (MIG) welding under the process conditions listed in Table 4.2. Pure Ar gas with a flow rate of 25 L/min was used as shielding gas. As shown in Fig. 4.3, a hemisphere heat source model with C equal to 6 mm was used, where C was the radius. The volumetric heat density used a Gauss

distribution in three directions of the welding wire coordinate system, and current, voltage, and speed were kept consistent with those in the experiment.

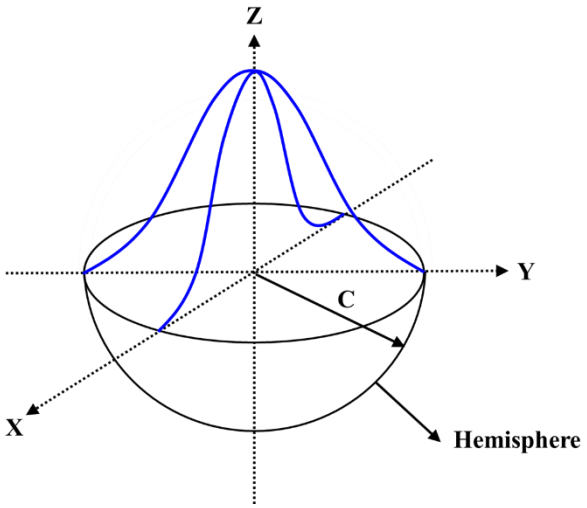

Fig. 4.3. Diagram of hemisphere heat source model with Gauss distribution.

The deposition path was established at the center of the top surface of each layer, with all layers starting from the same location at different heights. For one layer, the deposition took 15.07 s, and in the remaining 184.93 s, the layer cooled down to below 50 °C. The temperature on the deposition surface of each layer was measured by the contact thermometer before the next deposition. For the whole 20 layers, the time required was 4000 s, and the total design calculation time was 6000 s.

Table 4.2 The WAAM parameters used in the numerical simulation.

Heating section	Arc Welding Current(I)	Arc Welding Voltage(V)	Arc Welding Speed(mm/s)	Thermal Efficiency
Hemisphere (**Gauss distribution in 3 directions**)	149	14.5	16.667	0.8

In this experiment, the substrate was fixed to the working platform with four grippers. Therefore, in the simulation, the four nodes on the top surface of the substrate were fixed

in the X, Y, and Z directions during the first period. To better reflect the residual stress distribution, this boundary condition was released 4000 s after the deposition was completed and replaced with a normal 3-point boundary condition to calculate the unclamping deformation of the substrate, as shown in Fig. 4.4. The red arrows indicate that motion is fixed in the direction in which it points. The cutting simulation is based on the final state of the thermomechanical analysis.

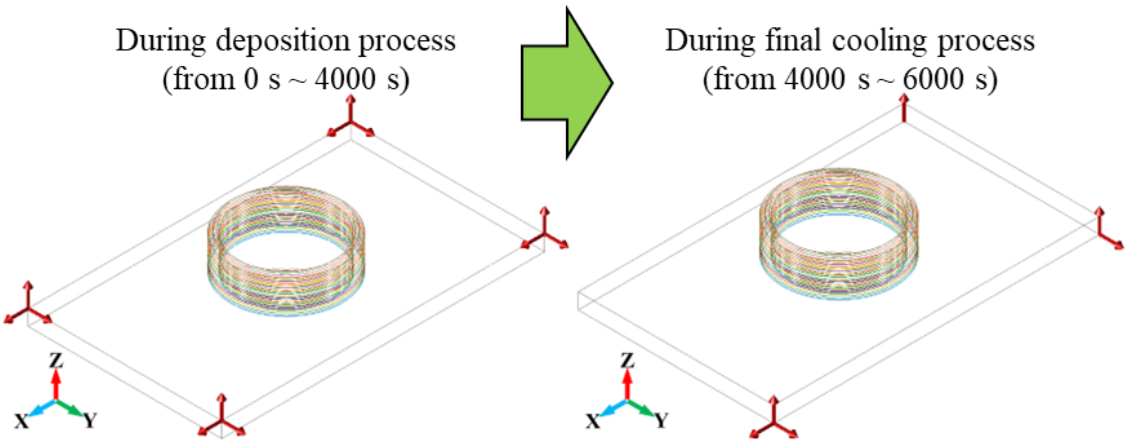

Fig. 4.4. The boundary conditions in the different periods, i.e., deposition and final cooling processes.

4.3.3. Material properties

The simulation process using JWRIAN-Hybrid is divided into thermal and mechanical analyses. Physical quantities such as stress, strain, and deformation can be calculated based on the thermal analysis results. Therefore, the material properties were divided into two sections. In thermal analysis, specific heat, thermal conductivity, and density vary with temperature, so these properties of 10Cr-10Ni (LTT) were measured at 24 °C, 400 °C, 800 °C, and 1200 °C. The thermal properties of the SUS304 were taken from a previous study[157]. Fig. 4.5 summarizes the thermal properties of the two materials.

Temperature-dependent properties, such as Young's modulus, Poisson's ratio, yield stress, hardening coefficient, and coefficient of thermal expansion, are needed for mechanical analysis and calculation. Most of these properties were taken from previous studies, except for the coefficient of thermal expansion of 10Cr-10Ni (LTT). The material model for 10Cr-10Ni (LTT) used in this study reproduces the phase transformation primarily by distinguishing the transient coefficient of thermal expansion during heating and cooling. The volume expansion rate caused by the phase transformation is over 0.5%. This variation in the coefficient of thermal expansion is described by the strain-temperature curve shown in Fig. 4.6, and all mechanical properties are shown in Fig. 4.7.

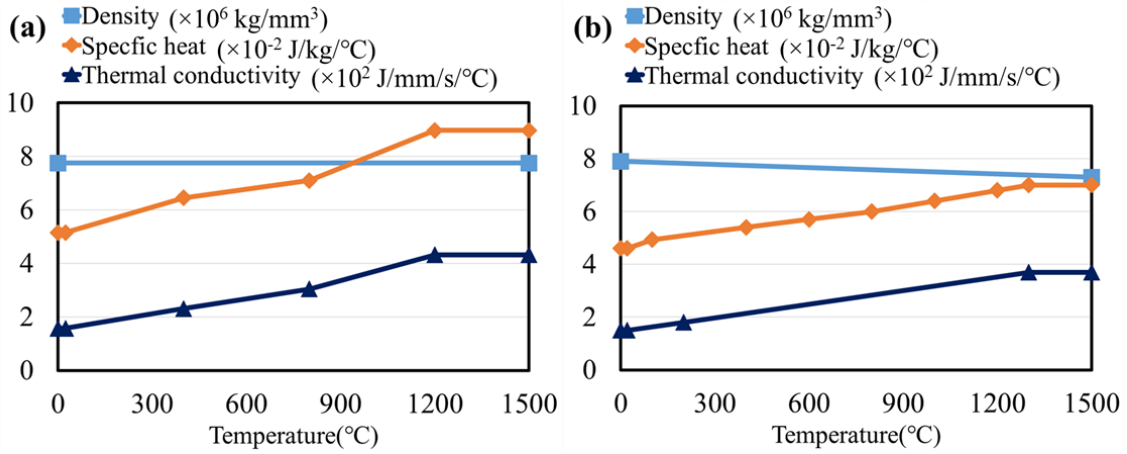

Fig. 4.5. The temperature-dependent thermal properties: (a) 10Cr-10Ni (LTT); (b) SUS304.

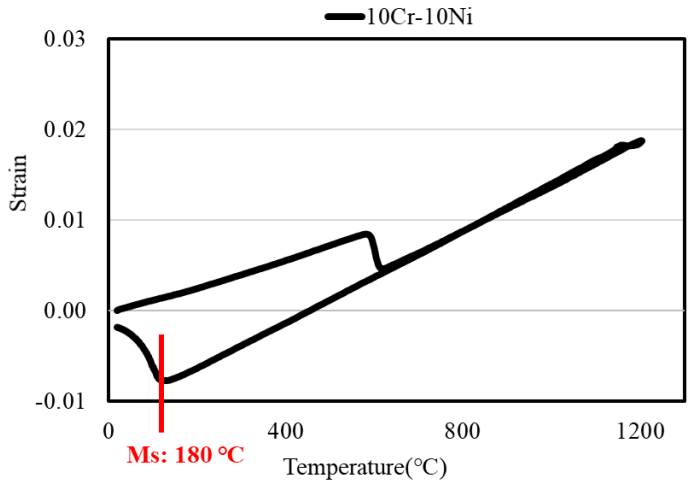

Fig. 4.6. The strain-temperature curve showing the phase transformation of 10Cr-10Ni (LTT).

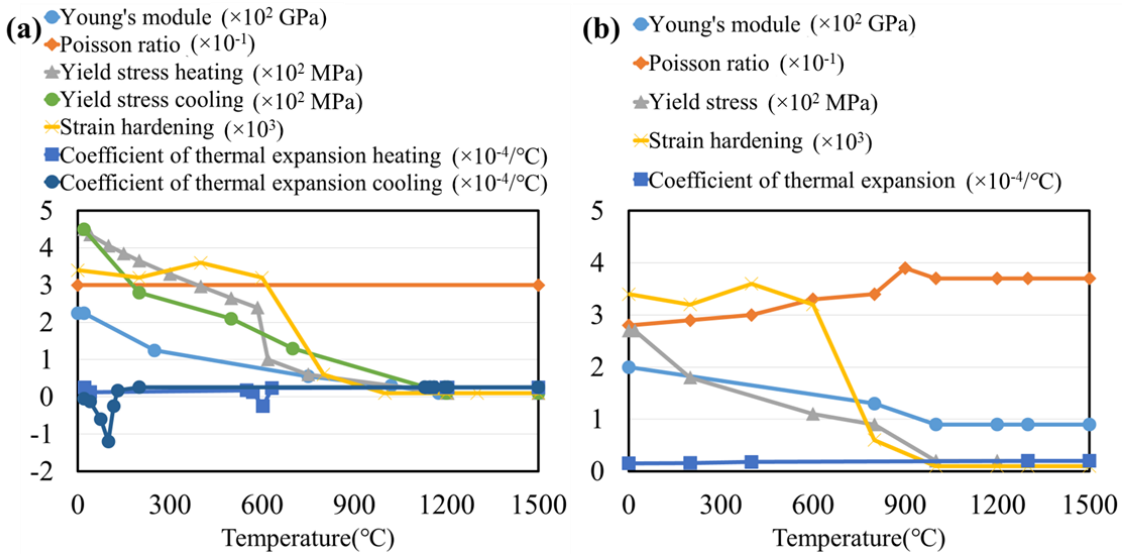

Fig. 4.7. The temperature-dependent mechanical properties: (a) 10Cr-10Ni (LTT); (b) SUS304.

4.4. Results and discussions

4.4.1. Thermal analysis

Fig.4.8(a) shows the history of the maximum temperature after WAAM and illustrates that all depositional layers melted and solidified during the process. Further details are shown in Fig.4.8(b), where the cross-sections are examined after the deposition of different layers to check the connections between each layer. After the deposition of the first layer, the molten zone included the deposition part and a portion of the substrate, indicating successful bonding between the first deposition layer and the substrate. Similarly, after the deposition of the 10^{th} or 20^{th} layer, all the deposition layers were completely melted and bonded together, which is consistent with the experiment.

To better understand the temperature variations in each layer, five representative layers 1, 5, 10, 15, and 20 were selected and their temperature profiles are plotted in Fig.4.9. For example, when the 1^{st} layer is deposited, the temperature reaches a maximum and then drops to the interpass temperature. During the thermal cycle, both austenite and martensite transformations occurred. During the deposition of the 2^{nd} layer, the peak temperature of the 1^{st} layer was lower than that of the previous layer; nevertheless, phase transformations occurred in both layers. During the deposition of the 3^{rd} and 4^{th} layers, the temperature of the 1^{st} layer continues to decrease, and both austenite and martensite transformations occur. During the deposition of the 5^{th} layer, the peak temperature of the 1^{st} layer falls below the austenite transformation temperature (Ac1), which corresponds to 630 °C. In this situation, the martensite could not transform to austenite during heating, so no martensite transformation occurred during cooling. A similar heating cycle took place in layers 2–20.

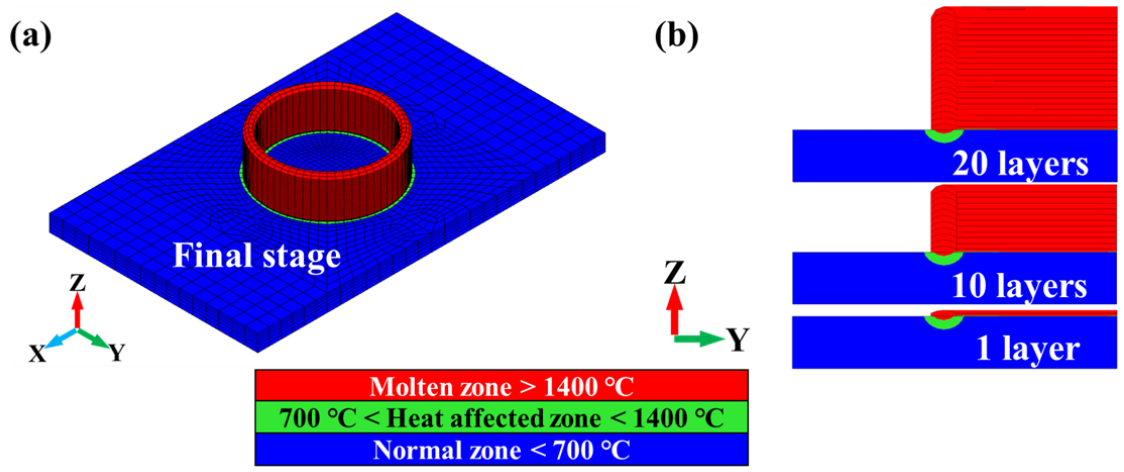

Fig. 4.8. Histories of the maximum temperature distribution during (a) the entire WAAM process and (b) after deposition of the 1st, 10th, and 20th layers.

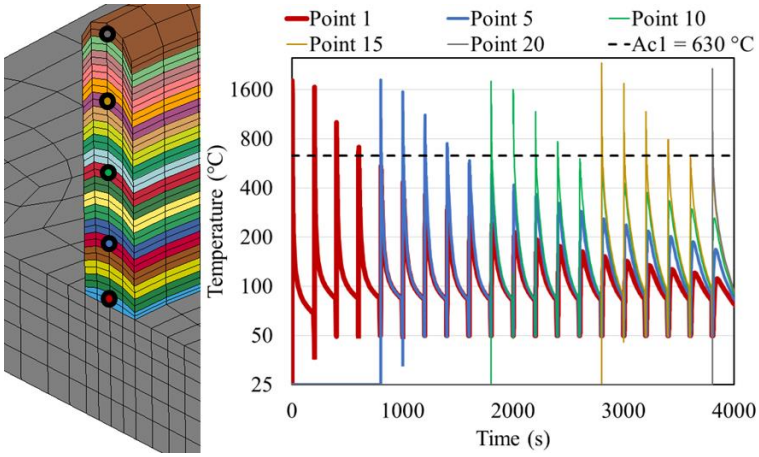

Fig. 4.9. Transient temperature histories for the center areas of the 1st, 5th, 15th, and 20th layers.

4.4.2. Deformation analysis

The experimental and simulated cross-section profiles are shown in Fig.4.10. For a more accurate comparison, the deformations before and after cutting were included. The experimental and simulated results agreed well, and the effect of cutting on the

deformation was negligible. Fig.4.11(a) shows the displacement contour of the bottom surface of the substrate in the Z-direction obtained from the measurements. The measured area exhibits an axisymmetric distribution. The edge of the substrate exhibits significant warping, with a maximum deformation of 1.0 mm. The substrate was relatively flat in a circular area with a radius of approximately 40 mm (exactly at the location of the WAAM) in the central portion, whereas outside this area, the deformation gradient increased. The simulated deformation contours of the bottom surface of the substrate in the Z-direction before and after cutting are shown in Fig.4.11(b) and (c), respectively. Significant deformations were consistently observed around the substrate edges, starting from the WAAM locations. The entire substrate was bent in both the X and Y directions, with a more pronounced deformation gradient in the X direction than in the Y direction. To better capture the deformation characteristics, a diagram with a deformation scale factor of 20 in the Z-direction is shown in Fig.4.11(d). The simulated deformation pattern agrees very well with the measured pattern, confirming the high accuracy of the simulations.

For further quantitative analysis, we extracted the Z-displacement data along the symmetry axis of the substrate from the measurements and simulations, as shown in Fig.4.11(d), and plotted them in Figs.4.12(a) and (b), respectively. The size of the central platform area was consistent in the measurements and simulations, whereas there were significant deformations outside the platform area. As for the distribution in the X-direction, the simulation had a maximum relative deformation value of 0.9 mm before cutting, whereas the unclamping deformation after cutting was approximately 0.02 mm. In this experiment, the maximum value of relative deformation is 0.94 mm. Similarly, for the distribution in the Y-direction, the simulated and measured maximum relative deformation values after cutting are 0.30 mm and 0.41 mm, respectively. The unclamping

deformation was also about 0.02 mm. The deviation between simulation and measurement is about 0.12 mm, which corresponds to 1 % of the substrate thickness, confirming the high simulation accuracy.

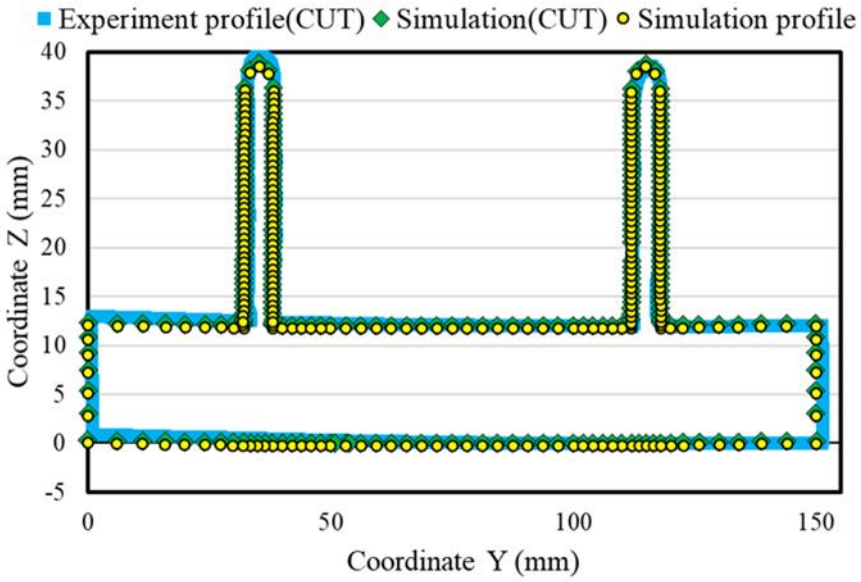

Fig. 4.10. Comparison of experimental and simulated cross-section profiles before and after cutting.

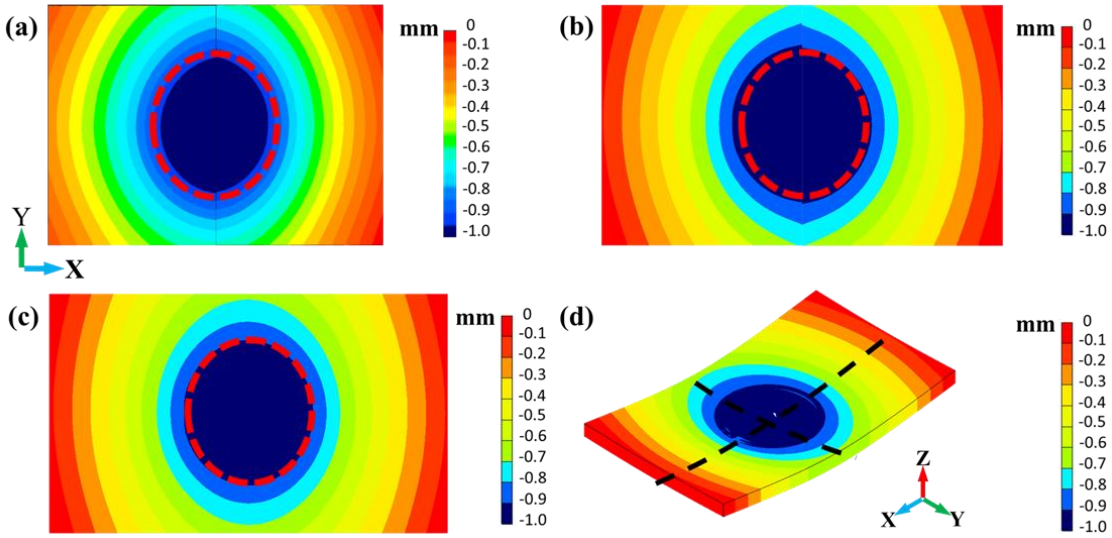

Fig. 4.11. Z-displacement contours of the substrate bottom surface after WAAM: (a) measured results and simulated results (b) after and (c) before cutting. (d) The Z-displacement from Fig.4.11(d) is magnified by 20 times for visualization.

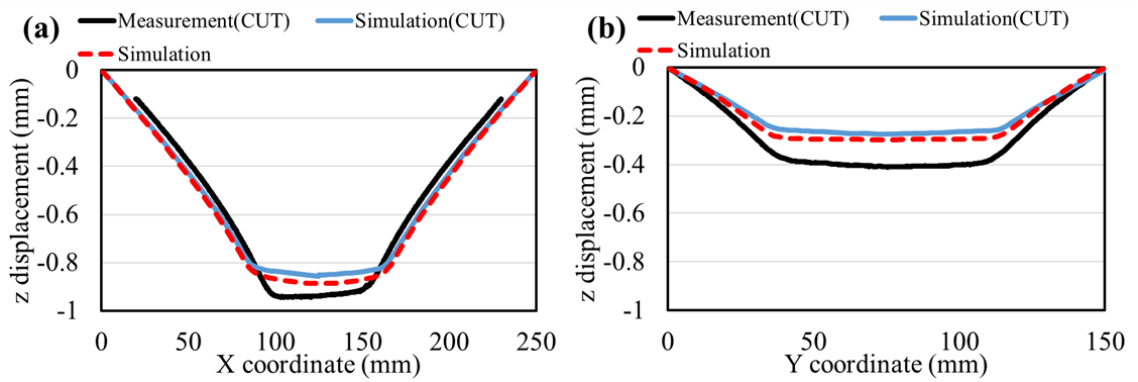

Fig. 4.12. Z-displacement distributions along the symmetry axis of the substrate from the measurement and simulations: (a) X-direction; (b) Y-direction.

4.4.3. Residual stress analysis

The residual stresses discussed in this section are circumferential residual stresses. Fig.4.13 shows images of the two cross-sections and the corresponding height profiles of the surfaces. On both surfaces, the deposition area was obviously lower than that of the substrate, and the highest areas were located on both sides of the substrate. The height distribution is consistent. However, due to the large size of the specimen and the sudden change in the cross-section during cutting, damage often occurs at the junction between the deposition part and the substrate, so the calculation of residual stress in the nearby area may be affected. The cross-sections of this specimen are complicated compared to those of other contour test specimens. In particular, the contours of the deposition region were irregular and could not be easily approximated by simple geometric shapes. To account for the geometric effect when calculating with the contour method, the model used was created based on the actual cross-section, as shown in Fig.4.14. The mesh size near the cross-section was 0.35 mm.

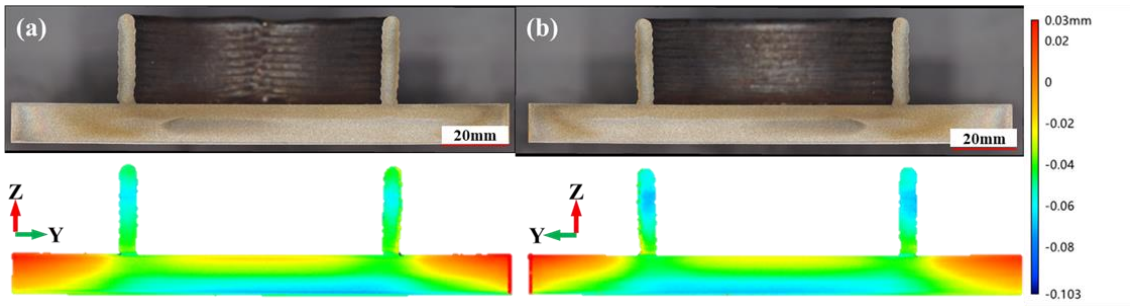

Fig. 4.13. Images and surface height profiles of (a) left and (b) right cross-sections.

The surface height profiles were entered into the FE model, and the residual stress distribution normal to the cross-section was reproduced by an elastic calculation. Fig.4.15(a) shows the residual stress distribution in the circumferential direction obtained by the contour method. For comparison, the simulated residual stress distributions in the YZ and XZ planes are shown in Fig.4.15(b) and (c), respectively. Both the measured and simulated results show that the residual stresses are symmetrically distributed in the circumferential direction. There are obvious compressive residual stresses at the top of the deposition region. The compressive residual stresses at the top changed dramatically into tensile stresses towards the interior (a few layers below). Within the substrate, compressive residual stresses occurred at the upper surface of the substrate edge. Residual stresses in the central area of the substrate were nearly zero, and the tensile residual stresses occurred mainly in the lower half of the substrate. These results are consistent with the bending deformation mentioned in Section 4.4.2. The transverse residual stress distribution on the YZ and XZ plane are shown in Fig.4.14(d) and (e). The results indicated that the transverse residual stress value was smaller than the one in the circumferential direction, mainly around -100MPa to 100MPa. There was no manifest compressive residual or tensile residual stress in the deposition part. The obvious tensile

residual stress, about 300MPa, occurred at the interface of the deposition part and substrate.

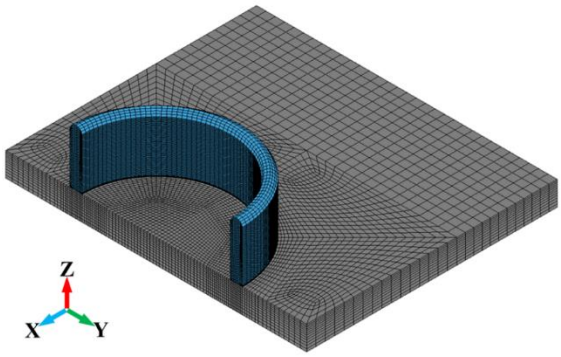

Fig. 4.14. FE model was created based on the actual cross-section to reproduce the residual stress using the contour method.

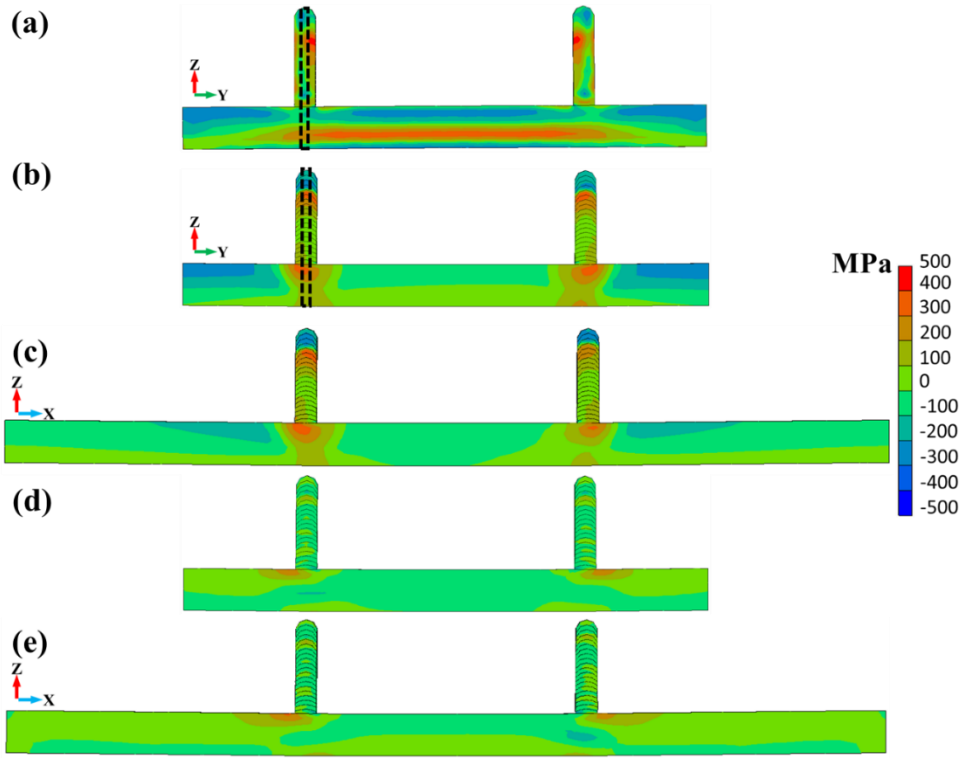

Fig. 4.15. Circumferential residual stress distributions on cross-sections: (a) YZ plane obtained by the contour method; (b) simulated YZ plane; (c) simulated XZ plane; Transverse residual stress distributions on cross-section: (d) simulated YZ plane; (e) simulated XZ plane.

For a better comparison between simulation and measurement, the average residual stresses are plotted in Fig.4.16 along the height direction in the dashed-line area in Fig.4.15. In both cases, compressive residual stresses were generated at the top of the deposition part, while tensile residual stresses occurred directly below. From top to bottom, the maximum compressive residual stress (~ -200 MPa) occurs at Z = 37.5 mm in the measurement, whereas it occurs at Z = 35 mm in the simulation. In both cases, after reaching the maximum compressive residual stress, the residual stress underwent a rapid change from compressive to tensile stress and reached the maximum tensile residual stress with decreasing height. The maximum tensile residual stress (~ 200MPa) occurred at Z = 29 mm and 32 mm, respectively, in the measurements and simulations. Subsequently, the residual stresses in both began to decrease simultaneously until Z = 20 mm.

The difference is in the lower portion, where the measurement showed slight compressive residual stresses, whereas the simulation showed more tensile residual stresses. The most likely reason for this discrepancy in the contour method measurement is cutting damage at the interface between the deposit and the substrate. In this study, the discrepancy near the damaged area was considered acceptable.

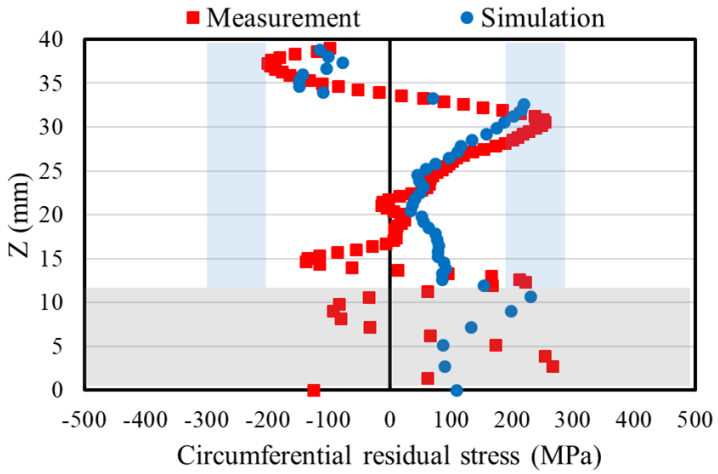

Fig. 4.16. Comparison of measured and simulated average residual stresses along the height direction in the dashed line area in Fig.4.15.

In the focal areas, the simulation and measurement results were mutually verifiable, and the final results were generally consistent with our expectations. The 10Cr-10Ni (LTT) material can generate compressive residual stresses in the WAAM parts. However, the areas where compressive residual stresses are generated are conditional and not distributed throughout the entire structure. To clarify these conditions, the simulation was further detailed and the entire WAAM process was divided into several stages for analysis. Fig.4.17 shows the distributions of residual stresses in the circumferential direction after deposition of the initial five layers. The tensile strains propagate throughout the deposition region at the end of the deposition of the 4th layer due to the volume expansion of the martensite transformation and deposited layers and the substrate prevent the volume expansion. Although volume expansion could still occur, the volume would be smaller compared to the unconstrained condition, leading to compression and compressive residual stresses. During the deposition of the 5th layer, the 2nd to 5th layers still reached the austenite transformation temperature, but the 1st layer does not meet this

temperature condition (Fig.4.9). During the cooling stage, the layers only generate compressive residual stresses from the 2nd to 5th layers due to a martensite phase transformation. Thus, the compressive residual stresses remain in the last four layers and the 1st layer transforms into tensile residual stresses.

Fig.4.18 shows the distribution of residual stresses in the circumferential direction after the deposition of the 5th, 10th, 15th, and 20th layers, as well as unclamping deformation. The residual stresses after deposition of the 20th layer were similar to those after unclamping deformation, indicating that the unclamping deformation effect was small in this case. Moreover, the residual stress distribution mode reached a steady state when the 10th, 15th, and 20th layers were deposited. In the last four layers, the tensile strain concentrations resulted in compressive residual stresses. That is, only when the temperature exceeds Ac1, martensite transformation occur during the cooling stage, resulting in compressive residual stresses. As shown in Fig.4.9, the location that can ultimately generate compressive residual stresses continues to move upward as the number of layers increases but always remains within the last four layers. Therefore, the key to generating compressive residual stresses by 10Cr-10Ni (LTT) under multiple thermal cycles, such as WAAM, is to complete the previous austenite transformation. To determine the effective depth (simply named by ED or D) of 10Cr-10Ni (LTT) in this study, the circumferential residual stress distributions along the height direction are plotted in Fig.4.17 and Fig.4.18. Except for the cases where the initial four layers were deposited, the average ED of the 10Cr-10Ni (LTT) in this study was 5.405 mm, which corresponds to the ED. The residual stress distribution patterns are shown in Fig.4.19. When the deposition height (DH) is lower than ED, the entire deposition section exhibits only compressive residual stresses. When the DH was higher than the ED, 10Cr-10Ni

(LTT) could only generate compressive residual stresses in the zone where the depth from the top of the deposition section was equal to the ED. According to the previous study on the residual stress distributions in different WAAM structures, this conclusion for 10Cr-10Ni (LTT) can also be applied to other WAAM structures.

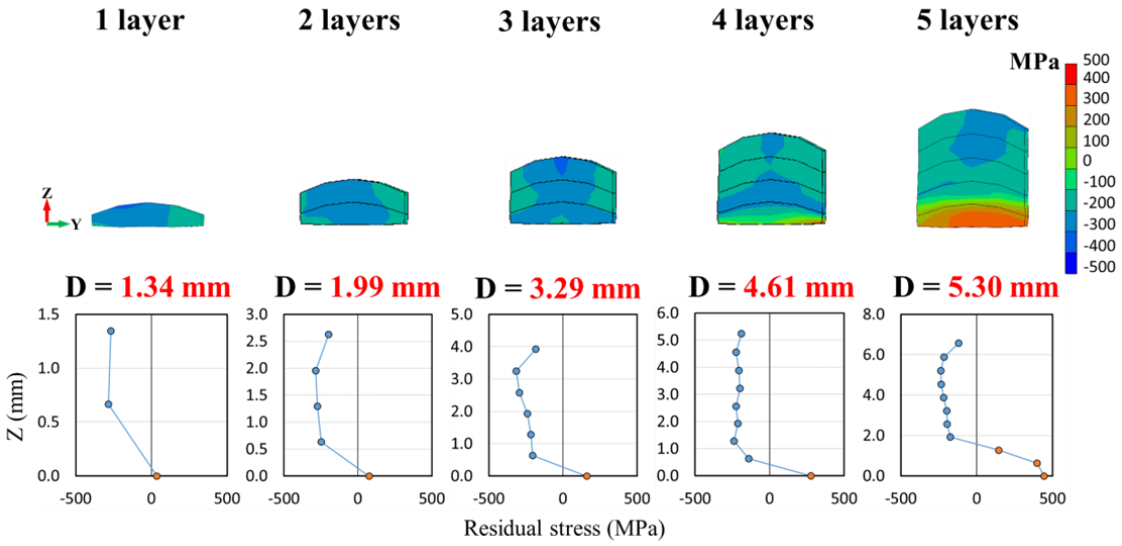

Fig. 4.17. Compressive residual stress and its effective depth D in the half cross-section after depositing the 1st, 2nd, 3rd, 4th, and 5th layers.

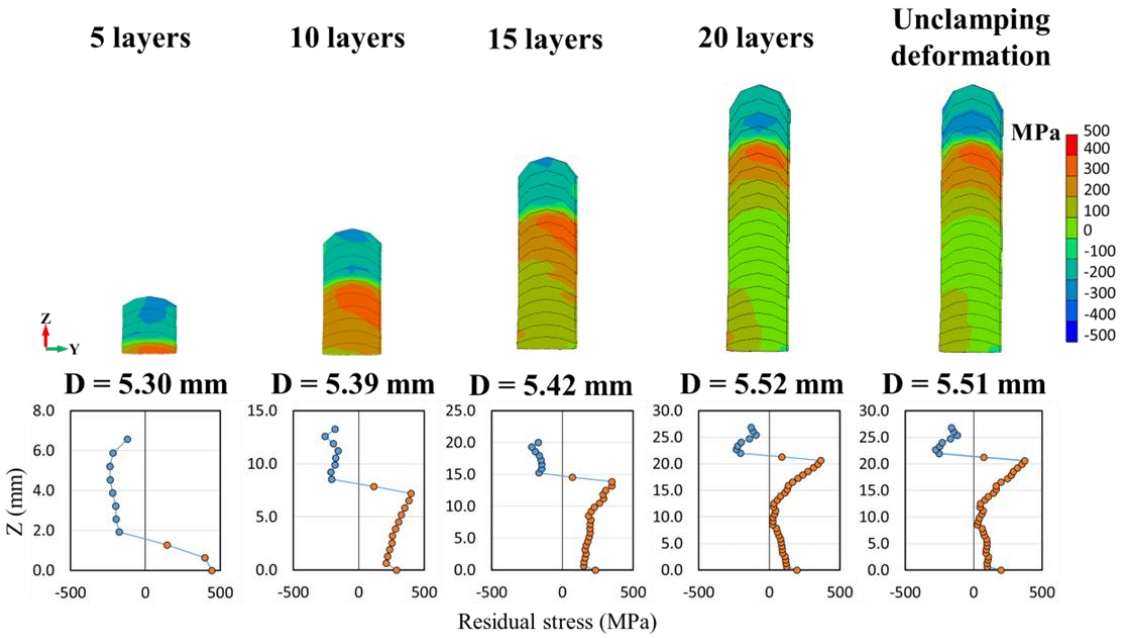

Fig. 4.18. Compressive residual stress and its effective depth D in the half cross-section after depositing the 5th, 10th, 15th, and 20th layers and the unclamping deformation.

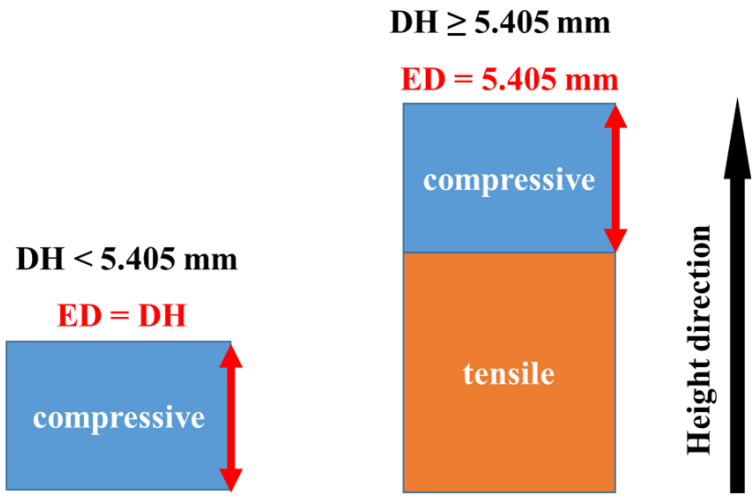

Fig. 4.19. Schematic diagram illustrating the distribution pattern of LTT residual stresses in WAAM.

4.5. Conclusions

In this study, an LTT material (10Cr-10Ni) was used as the feedstock in WAAM to fabricate a pipe structure on a SUS304 substrate. The deformation of the substrate and the distribution of residual stress in the circumferential direction were quantitatively analyzed by a combination of experiments and simulations. More importantly, the distribution characteristics and formation mechanism of the LTT residual stress in WAAM were elucidated based on established simulations. The main conclusions are as follows:

(1) The 10Cr-10Ni (LTT) pipe structure was successfully fabricated by WAAM, and each layer achieved metallurgical bonding with adjacent layers. Moreover, the heat source of WAAM causes the peak temperature of the four layers to exceed Ac1, and then they undergo phase transformation during cooling.

(2) The overall deformation of the WAAM specimens was small. The deformation mainly occurs on the substrate. The substrate exhibited a flat center and warped edges. The transition from flat to warped depended on where the deposition occurred. Both the simulated and actual deformations were in good agreement, demonstrating the high simulation accuracy.

(3) The simulated residual stress distribution agreed well with that measured by the contour method, further supporting the high accuracy of the simulations. The compressive residual stresses were concentrated near the top of the deposition section and shifted inward toward the tensile residual stresses. The maximum compressive and tensile residual stresses were -200 MPa and 200 MPa, respectively.

(4) The formation mechanism of the 10Cr-10Ni (LTT) residual stress in WAAM was revealed. Compressive residual stresses were generated only when the peak temperature in the target region exceeded Ac1 during the last thermal cycle. Moreover, the depth causing compressive residual stresses due to 10Cr-10Ni (LTT) was constant, i.e., ED = 5.405 mm in this study. This finding has significant implications for future applications of 10Cr-10Ni (LTT) materials in WAAM.

Chapter 5. Interpass temperature strategies for compressive residual stresses in cladding low-transformation-temperature material 16Cr8Ni via wire arc additive manufacturing

5.1. Introduction

Low-transformation-temperature (LTT) materials induce compressive residual stresses within an effective depth in wire arc additive manufacturing (WAAM), which is well suited for cladding applications. However, this role was found to be sensitive to the phase transformation sequence. We developed an LTT material—16Cr8Ni (16Cr8Ni-LTT)—and to explore its potential, it was clad onto a KA36 substrate via WAAM. Three different interpass temperature strategies were designed as follows: (1) no interpass temperature control; (2) interpass temperature controlled at approximately 270 ℃ above the martensite transformation start temperature (Ms = 200 ℃) for simultaneous phase transformation; and (3) interpass temperature controlled at approximately 50 ℃ below the martensite transformation finish temperature (Mf = 60 ℃) for sequential phase transformation. A thermal elastic–plastic numerical model considering the phase transformation-induced plasticity (TRIP) was developed using in-house software, JWRAIN-Hybrid, to reproduce the temperature field and residual stresses of 16Cr8Ni-LTT cladding. X-ray diffraction (XRD) and contour methods were employed for residual stress measurements. The high accuracy of the model was validated in terms of the temperature, deformation, and residual stress. The reproduced maximum historical temperature distributions were combined with hardness tests to identify the depths and temperatures of the heat-affected zone (HAZ). The measured maximum compressive

residual stresses induced by the three interpass temperature strategies for cladding 16Cr8Ni-LTT were −503, −420, and −720 MPa. Moreover, irrespective of the adopted interpass temperature strategy, both longitudinal and transverse residual stresses were compressive in the 16Cr8Ni-LTT cladding. This study provides scientific insights into LLT-induced compressive residual stresses and highlights the superiority and flexibility of cladding LTT materials via WAAM for improving the resistance of large metal components to fatigue and corrosion.

5.2. Materials and methods

5.2.1. Materials

16Cr8Ni-LTT and KA36 were selected as the wire-feed material and base metal (BM) for the WAAM-based cladding experiments. The 16Cr8Ni-LTT wire is a welding consumable developed by Osaka University and Kobe Steel, Ltd., Japan for all repair welding positions, with a diameter is 1.2 mm. According to our previous study[158], 16Cr8Ni-LTT underwent dilution when welded with KA36, with a dilution ratio of 27%. Therefore, the material properties of 16Cr8Ni-LTT with a dilution rate of 27% (16Cr8Ni-LTT-27%) were used in the numerical simulations in this study. KA36 belongs to the category of high-strength shipbuilding structural steels and is renowned for its strength and corrosion resistance, making it widely utilized in the shipbuilding industry. The chemical compositions of the three materials are listed in Table 5.1.

Table 5.1 Chemical composition of 16Cr8Ni-LTT, 16Cr8Ni-LTT-27%, and KA36.

Materials	Chemical compositions (wt.%)						Ms (℃)
	C	Si	Mn	Cr	Ni	Fe	
16Cr8Ni-LTT	0.02	0.34	0.44	16.10	8.20	Bal.	33
16Cr8Ni-LTT-27%	0.07	0.49	0.50	10.90	6.1	Bal.	200
KA36	0.14	0.21	1.10	–	–	Bal.	–

5.2.2. WAAM-based cladding process

The cladding process was performed using an arc welding machine. The 16Cr8Ni-LTT wires were melted and deposited onto a substrate rolled from KA36, measuring 200 mm in length, 100 mm in width, and 20 mm in thickness. Considering the sensitivity of 16Cr8Ni-LTT to the thermal cycle temperature, three specimens were fabricated under different interpass temperature-control strategies, depending on the martensite transformation start and finish temperatures of 16Cr8Ni-LTT. In Case A, there was no interpass temperature control during cladding. Cases B and C were not required to start the next pass until the specimen temperature cooled to 270 ℃ (simultaneous phase transformation) and 50 ℃ (sequential phase transformation), respectively. The recorded experimental parameters and images of the three cases are presented in Table 5.2 and Fig.5.1, respectively.

Table 5.2 Specific cladding parameters for Cases A, B, and C.

	Pass	Current (A)	Voltage (V)	Velocity (mm/s)	Arc time (s)	Interpass temperature (℃)
Case A	1	200	32	3.34	59	None
	2	200	32	3.34	59	
	3	200	32	3.34	60	
	4	200	32	3.34	60	
	5	200	32	3.34	58	
	6	200	32	3.34	59	
	7	200	32	3.34	60	
	8	200	32	3.34	61	
Case B	1	200	32	3.34	60	≈ 270 ℃
	2	200	32	3.34	61	
	3	200	32	3.34	59	
	4	200	32	3.34	60	
	5	200	32	3.34	60	
	6	200	32	3.34	60	
	7	200	32	3.34	59	
	8	200	32	3.34	60	
Case C	1	196	32.9	3.34	55	≈ 50 ℃
	2	195	32.9	3.34	55	
	3	191	32.9	3.34	55	
	4	198	33	3.34	55	
	5	193	33	3.34	55	
	6	196	32.9	3.34	55	
	7	194	32.9	3.34	55	

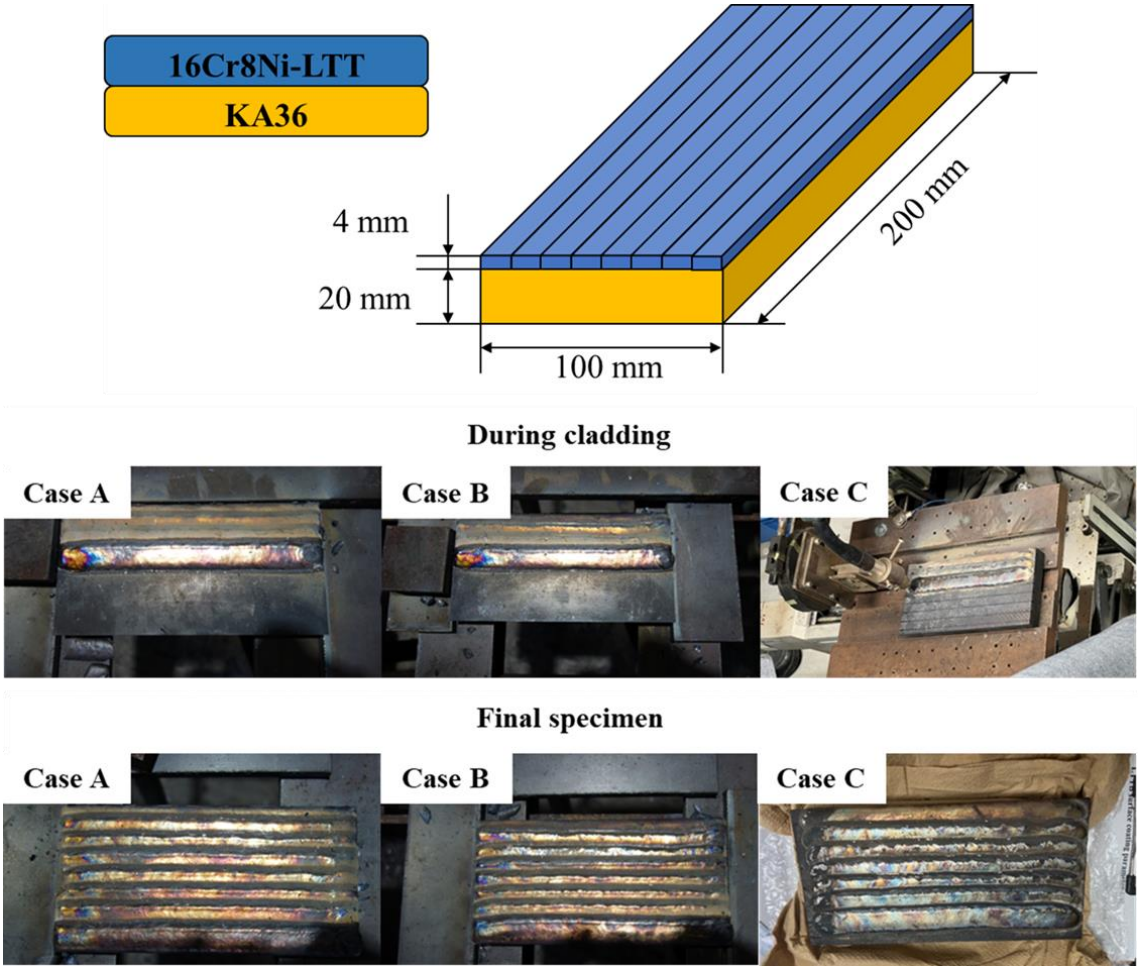

Fig. 5.1. Schematic diagram of cladding specimen dimensions and images during and after cladding for Cases A, B, and C.

5.2.3. Characterization and measurement methods

The TELEDYNE FLIR thermal graph camera recorded the cooling-temperature history for Case C. The emissivity values of KA36 and 16Cr8Ni-LTT were calibrated to 0.95 and 0.25, respectively. The deformation of the substrate bottom surfaces after cladding was measured using a Keyence VR5200 one-shot 3D shape measurement machine, and the deformation profiles and curves were extracted using matching software.

To clarify the heat-affected zone (HAZ), the Vickers hardness was measured over a wide area, including the molten pool, HAZ, and BM, using a Mitsutoyo HM-200 series microhardness tester. XRD and contour methods were employed in this study for residual stress measurements. A μ-X360s portable X-ray residual stress analyzer, equipped with a chromium X-ray tube, was used with the XRD method to scan a rectangular area of the cladding surface to measure the surface residual stress. The interval between scanning points was 4 mm. After being cut using the wire electrical discharge machining method, the Keyence VR5200 was applied to obtain the cross-sectional profile. Thereafter, the measured data were input into a contour method calculation program to obtain the residual stress distribution normal to the cross-section.

5.3. Numerical modeling

5.3.1. Geometric modeling

Three thermo-mechanical coupled FE models with birth-death elements were developed in this study. The geometry and meshing are shown in Fig.5.2. The geometries of the cladding passes were modeled by referring to the actual shapes of the specimens. The cladding passes, and the BM area near the molten pool is meshed with 1 mm elements, whereas the remaining area of the BM is coarsely meshed to save computational resources. All elements were fully integrated 8-node hexahedral solid elements. Cases A and B used the same FE model, with 86,853 nodes and 79,350 solid elements. The FE model for Case C had 82,464 nodes and 75,237 solid elements. The last pass area of Case C remained unclad to identify the residual stress on this surface.

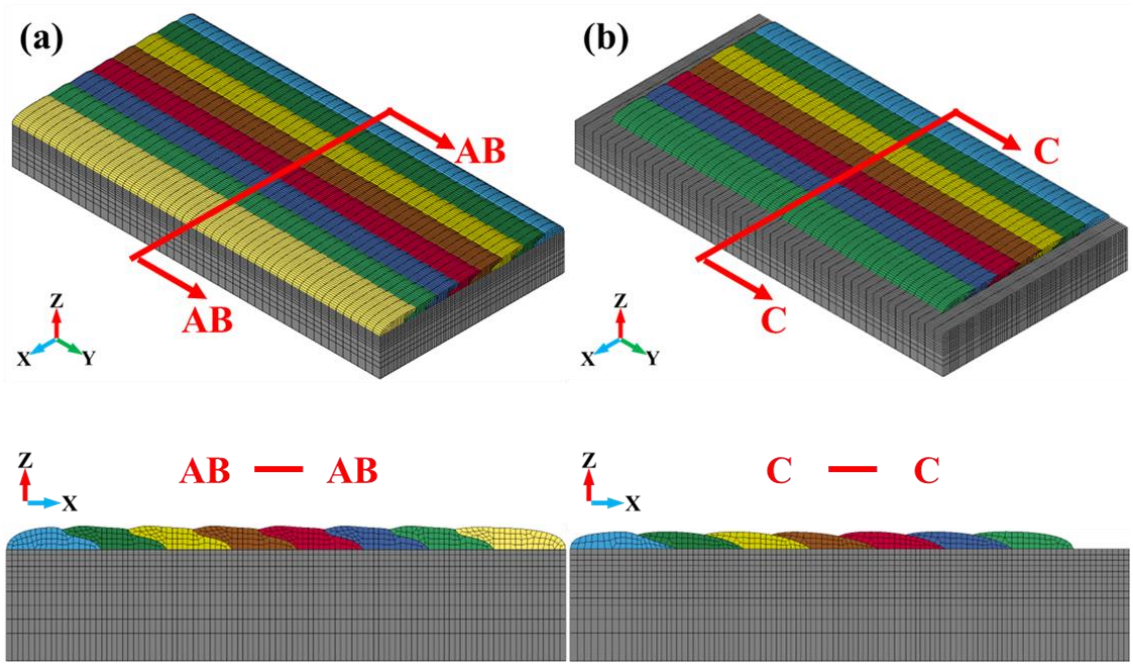

Fig. 5.2. Geometries and meshing of entire FE model and cross-sections: (a) Case A and Case B; (b) Case C.

5.3.2. Process parameters, heat sources, and boundary conditions

The arc-related parameters were set based on these experiments. A semi-ellipsoid heat source with a Gaussian thermal distribution was applied in all the cases, as shown in Fig.5.3. Table 5.3 details the simulation settings for Cases A, B, and C.

Table 5.3 Simulation settings for Cases A, B, and C.

	Current (A)	Voltage (V)	Velocity (mm/s)	Thermal efficiency	Heat source	a (mm)	b (mm)	b (mm)
Case A	200	32	3.334	0.7	Semi-ellipsoid	14	14	6
Case B	200	32	3.334	0.7	Semi-ellipsoid	14	14	6
Case C	193	33	3.334	0.7	Semi-ellipsoid	15	15	5.5

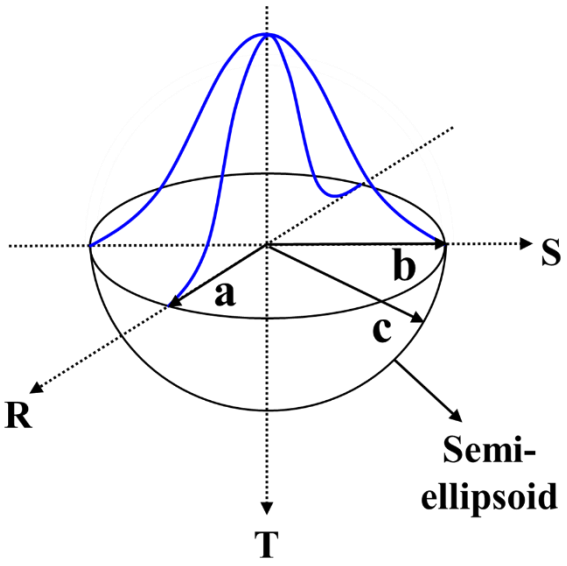

Fig. 5.3. Schematic diagram of a semi-ellipsoid heat-source model with Gaussian thermal distribution in three directions.

The interpass temperature-control strategy for each case was consistent with the experiments, that is, 270 ℃ for Case B and 50 ℃ for Case C. Because no extra jigs were used for the experiments, the substrate was placed on a working plate. Therefore, a three-point fixation with six degrees-of-freedom constraints was applied to the simulations. Fig. 5.4 shows the exact locations of the constrained degrees-of-freedom for each case.

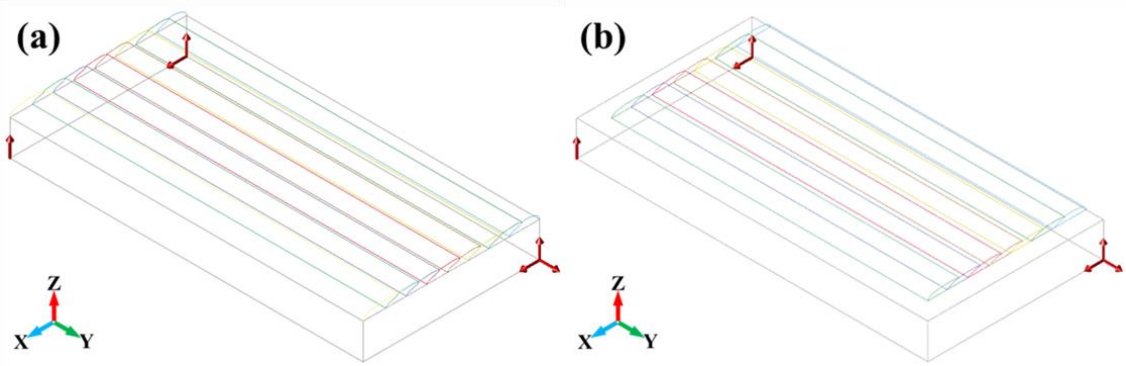

Fig. 5.4. Specific boundary settings for (a) Case A, Case B, and (b) Case C.

5.3.3. Material parameters of cladding layer and substrate

Simulations with the in-house software, JWRIAN-Hybrid, require thermal and mechanical material parameters. Hence, the temperature-dependent material properties of 16Cr8Ni-LTT-27% and KA36 were measured. In the adopted elastoplastic material model, for a more accurate calculation of the stress field, stress-strain curves at different temperatures were utilized instead of yield stress and strain-hardening-coefficient curves.

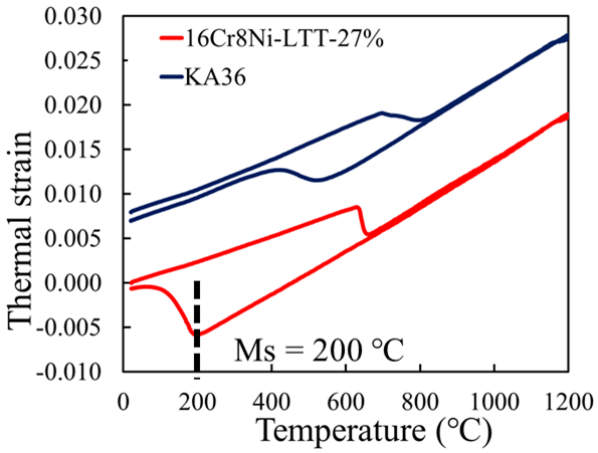

Fig. 5.5. Thermal strain versus temperature curves for 16Cr8Ni-LTT-27% and KA36.

The effect of phase transformation on the stress was reflected by the instantaneous coefficient of thermal expansion. The thermal-expansion curves of both materials were measured, and the results are shown in Fig.5.5. There is an obvious volume expansion of 16Cr8Ni-LTT-27% at approximately 200 °C during the cooling period. During the cooling period of KA36, the volume expansion is slight and starts at approximately 500 °C. All the temperature-dependent material properties are displayed in Fig.5.6 and 5.7.

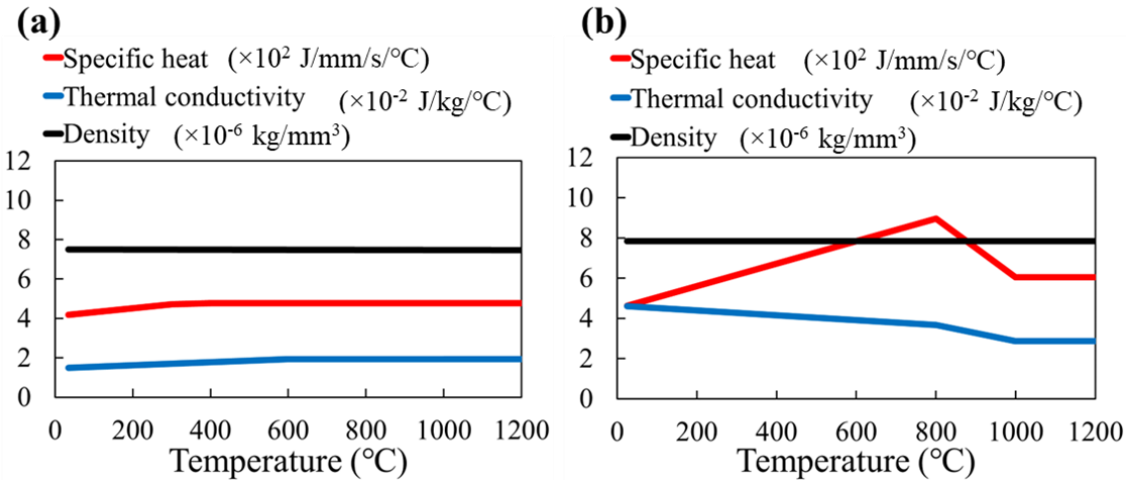

Fig. 5.6. Temperature-dependent thermal properties: (a) 16Cr8Ni-LTT-27%; (b) KA36.

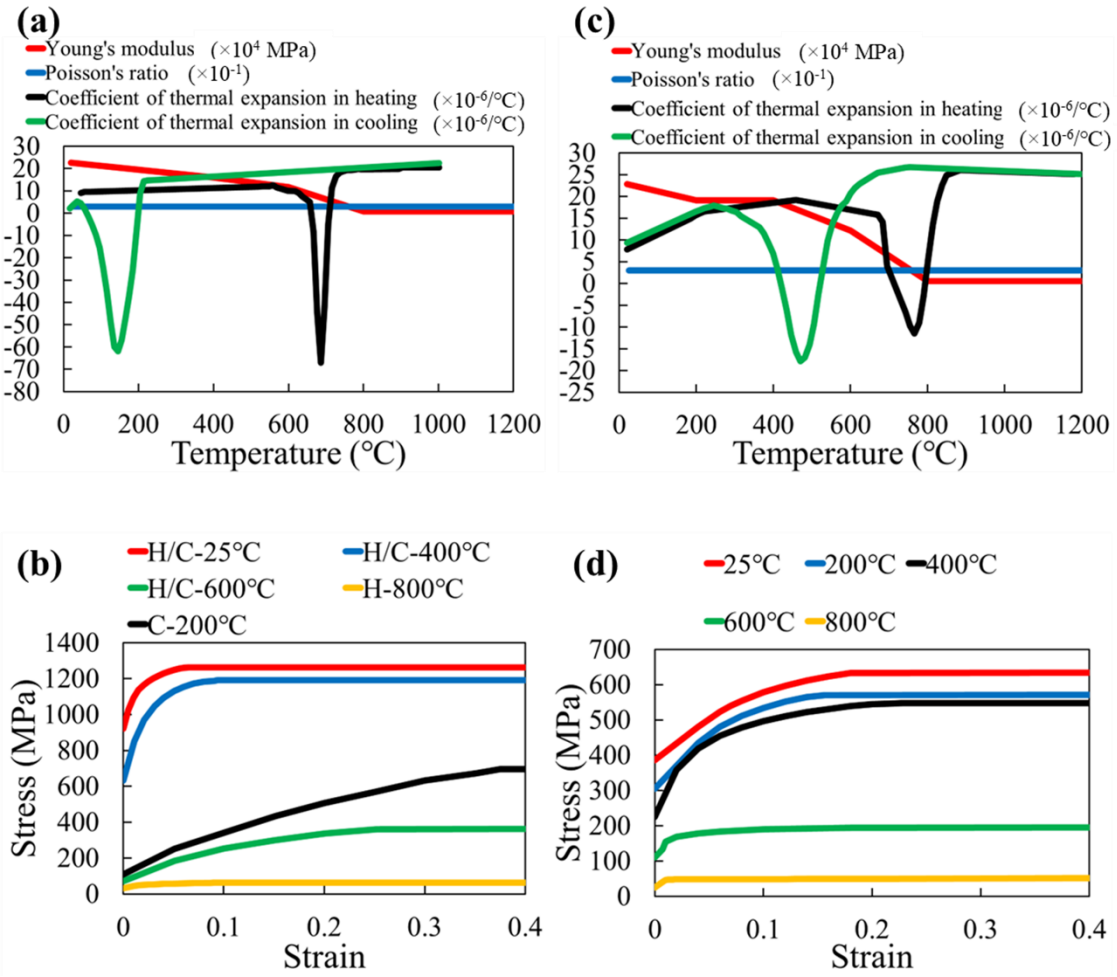

Fig. 5.7. Temperature-dependent mechanical properties and stress–strain curves: (a, b) 16Cr8Ni-LTT-27%; (c, d) KA36.

Air cooling was the dominant factor during the experiments. In Case C, the copper plate was positioned beneath the substrate to expedite cooling, whereas the other surfaces were air-cooled. Copperplate cooling differs from air cooling and can be calculated using the following equations:

$$Q = h \times A \times (T - T_{cold}), \quad \text{Eq.5.1}$$

$$Q = m \times C \times \frac{(T - T_{cold})}{\Delta t}, \quad \text{Eq.5.2}$$

where Q is the heat-transfer rate, h is the heat-transfer coefficient, A is the surface area that transfers heat, T is the temperature of the hot side, T_{cold} is the temperature of the cold side, m is the mass of the substance, C is the specific heat capacity of the substance, and Δt is the time required for the temperature to change. The final input heat-transfer coefficient curves are shown in Fig.5.8.

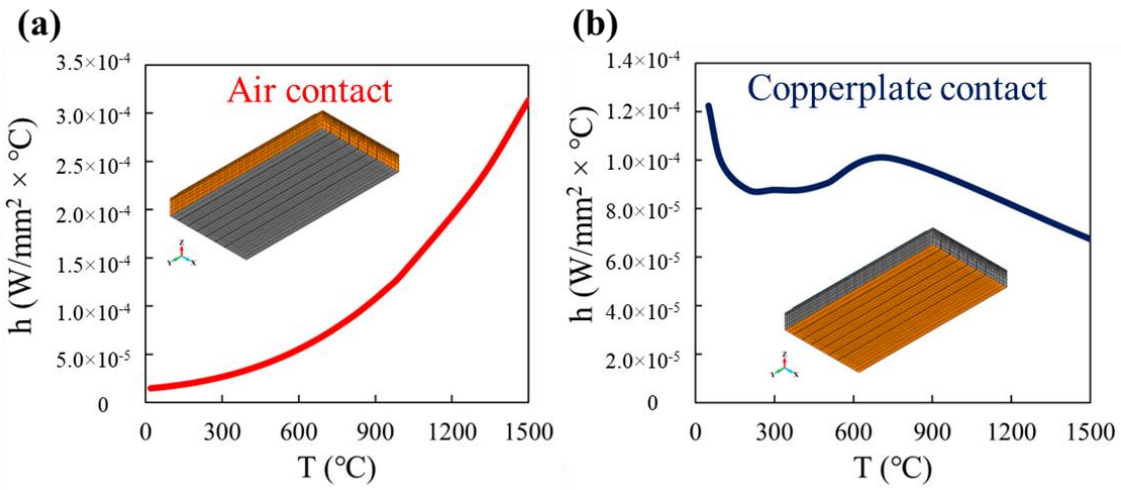

Fig. 5.8. Heat-transfer coefficient versus temperature curves and applied surfaces: (a) air contact and (b) copperplate contact.

5.3.4. Phase transformation-induced plasticity (TRIP) modeling

Phase TRIP refers to a significant increase in the plasticity of a material during a phase transformation. Plastic deformation occurs when the equivalent stress corresponding to an externally applied load is lower than the normal yield stress of the material. According to Yamamoto et al.[159], TRIP appears during the cooling period of LTT materials and must be considered when performing numerical simulations. Thus, using the TRIP modeling in JWRIAN-Hybrid, strain ε is defined as the sum of elastic strain ε^e, plastic strain ε^p, thermal strain ε^{th}, and phase transformation plastic strain ε^{tp}, as follows:

$$\varepsilon = \varepsilon^e + \varepsilon^p + \varepsilon^{th} + \varepsilon^{tp}. \quad \text{Eq.5.3}$$

Regarding the increment of ε^{tp} during the martensite transformation, it can be calculated using the following equations:

$$\{\Delta\varepsilon^{tp}\} = 3 \times K \times \{\sigma'\} \times (1 - f_M) \times \Delta f_M, \quad \text{Eq.5.4}$$

$$\{\sigma'\} = \begin{Bmatrix} \sigma_{XX} - \sigma_{av} \\ \sigma_{YY} - \sigma_{av} \\ \sigma_{ZZ} - \sigma_{av} \\ \tau_{XY} \\ \tau_{YZ} \\ \tau_{ZX} \end{Bmatrix}, \quad \text{Eq.5.5}$$

$$\sigma_{av} = \frac{1}{3} \times (\sigma_{XX} + \sigma_{YY} + \sigma_{ZZ}), \quad \text{Eq.5.6}$$

where f_M is the martensite fraction; K is the coefficient of transformation plasticity; $\{\sigma'\}$ is the deviation stress; and σ_{XX}, σ_{YY}, σ_{ZZ}, τ_{XY}, τ_{YZ}, and τ_{ZX} are the stress components, σ_{av} is the average stress. Based on the above calculations, the phase transformation plasticity can be estimated and applied to improve the mechanical analysis for numerical simulations.

5.4. Results and discussions

5.4.1. Thermal analysis

Fig.5.9 shows the maximum historical temperature distributions for the three cases obtained by thermal analysis. The melting temperature of 16Cr8Ni-LTT-27% is 1,479 °C. It is evident that all the cladding passes underwent melting and solidification processes. In Case C, a distinct heat-transfer condition was applied to the bottom surface (Section 5.3.3). A thermal graph camera recorded the cooling period of the final cladding pass for verification. Fig.5.10(a) shows the measured position, and Fig.5.10(b) compares the measured and simulated cooling-temperature histories. The simulation and measurement results are in good agreement, thereby verifying the accuracy of the thermal analysis model.

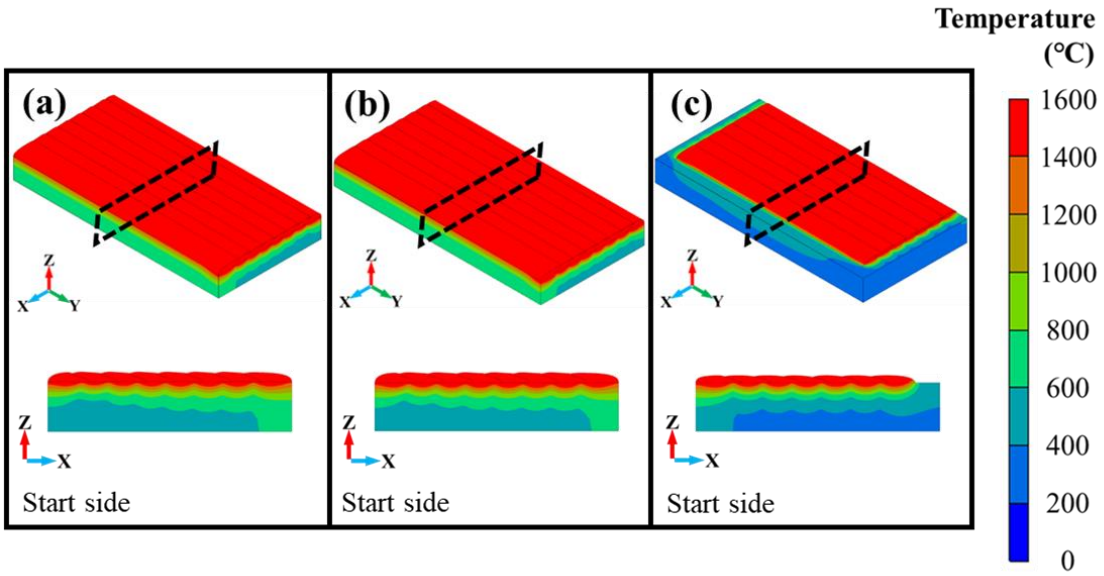

Fig. 5.9. Overall and cross-sectional maximum historical temperature distributions for (a) Case A, (b) Case B, and (c) Case C.

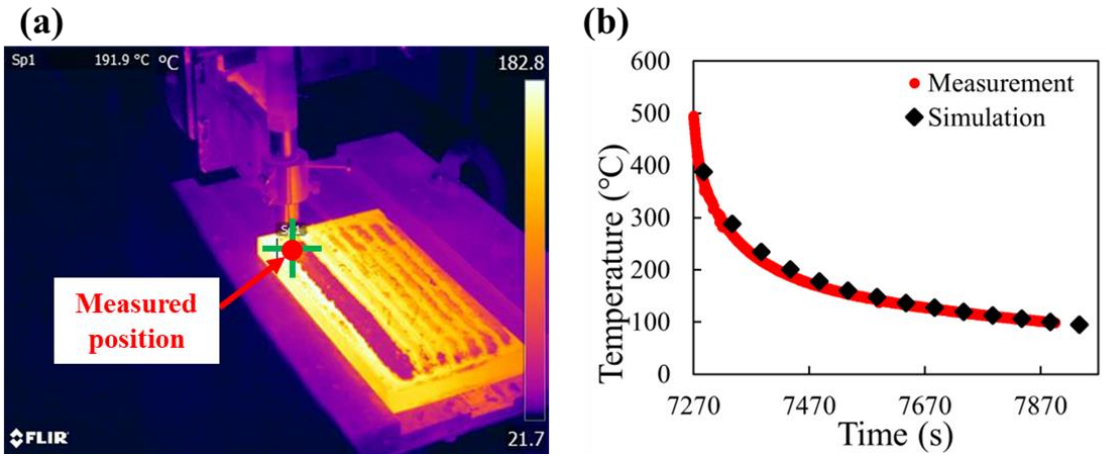

Fig. 5.10. (a) Cooling period of the final cladding pass in Case C via thermal graph camera and (b) comparison with the simulated cooling-temperature history.

Hardness tests were conducted to identify the HAZ depth and temperature. The Vickers hardness contours of the three cases are shown in Fig.5.11. The molten pool has high hardness owing to the martensite produced by the phase transformation. In the BM, a low hardness is observed because the main microstructures of KA36 are ferrite and pearlite. The HAZ hardness ranges between those of the molten pool and BM, and no softening occurs. The average HAZ depths for Cases A, B, and C are 2.25, 2.20, and 2.00 mm, respectively. Compared with the simulation results depicted in Fig.5.12, the HAZ temperature of KA36 ranges from 1,050 °C to its melting point (1,433 °C).

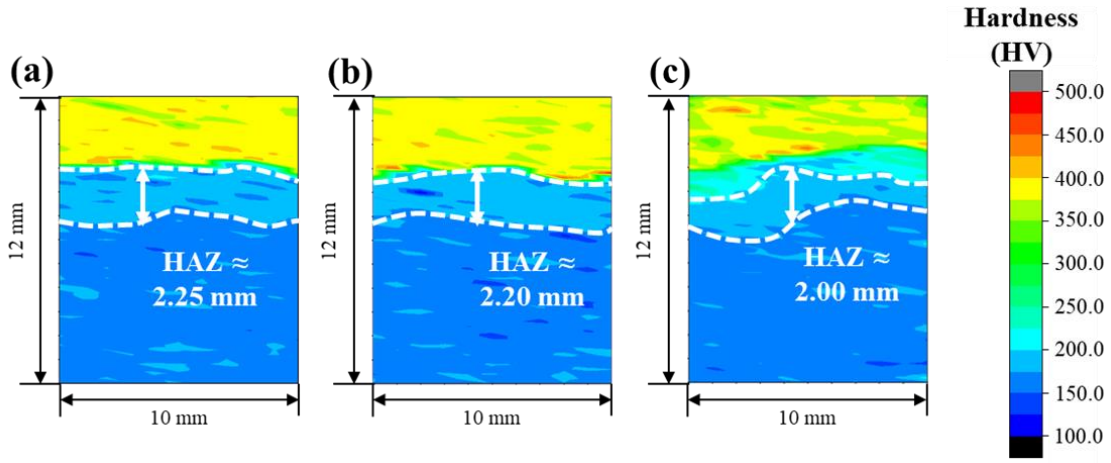

Fig. 5.11. Vickers hardness contours including the molten pool, HAZ, and BM: (a) Case A, (b) Case B, and (c) Case C.

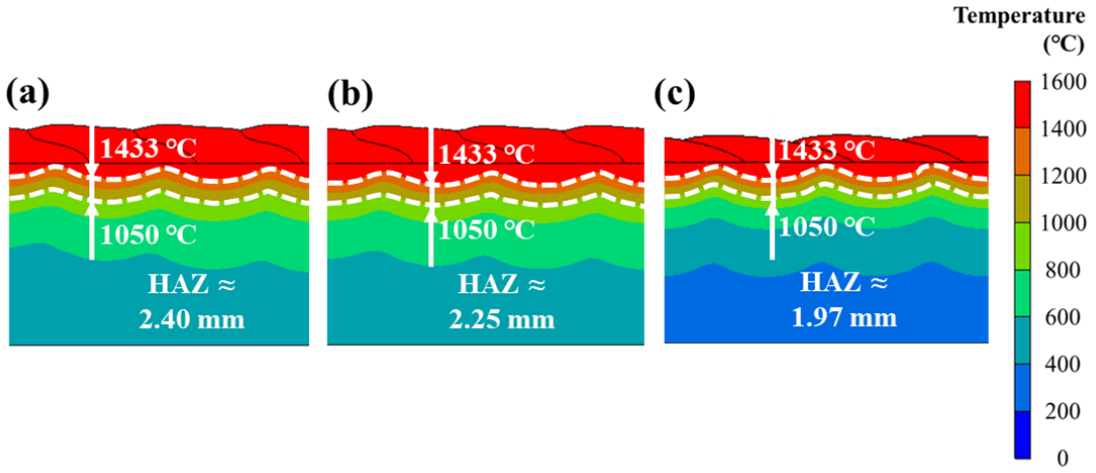

Fig. 5.12. Simulated maximum historical temperature distributions combined with hardness distributions to identify HAZ depths and temperatures: (a) Case A, (b) Case B, and (c) Case C.

5.4.2. Deformation analysis

The substrate deformation was investigated with a focus on the major deformation; that is, the bending deformation in the Z-direction. Fig.5.13 shows a comparison of the

measured and simulated deformation contours in the Z-direction. As can be seen from the measurement results, the deformation patterns are similar in all cases, with the substrate warping upward around the perimeter, and the contour lines of deformation distributed in an elliptical shape. The maximum deformation occurred near the four corners of the substrate. All the above deformation features were reproduced accurately by simulations.

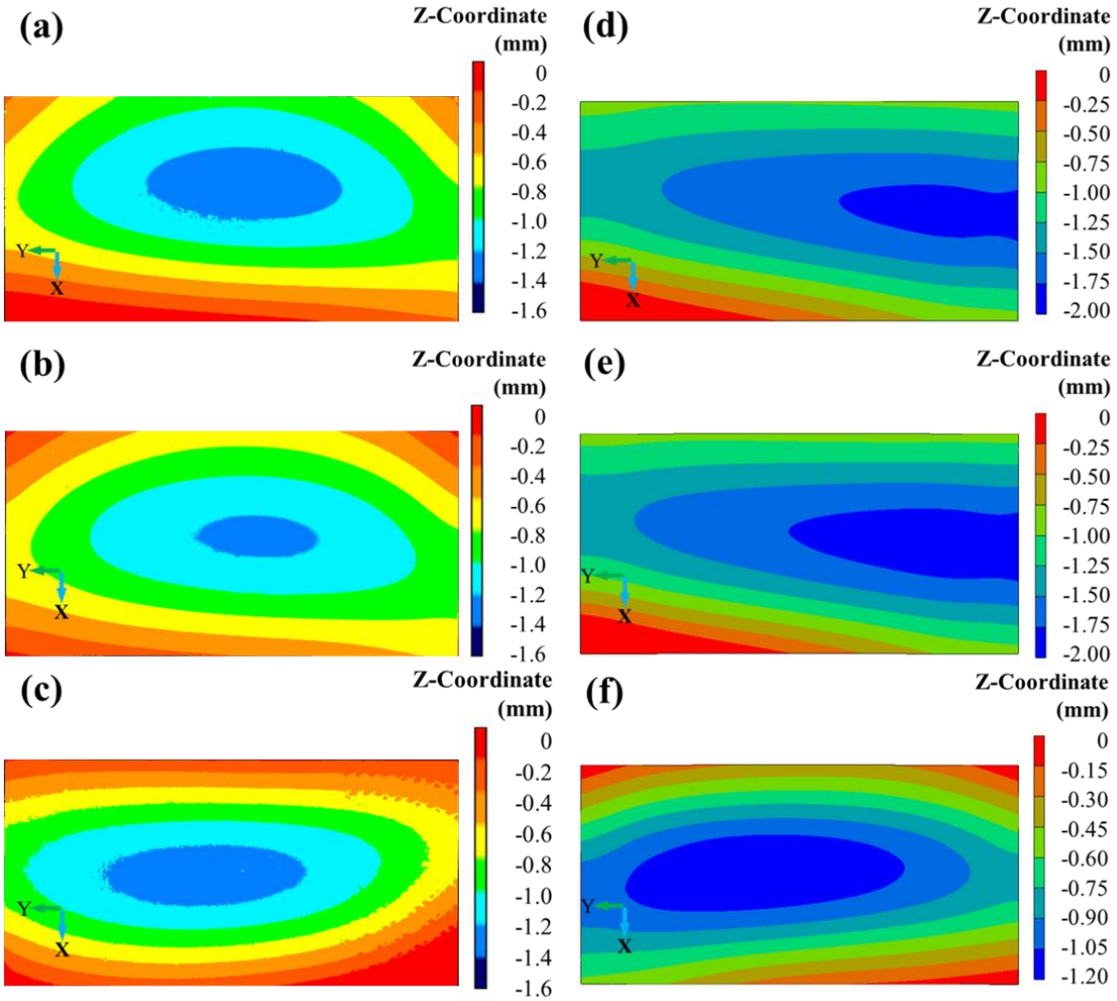

Fig. 5.13. Measured and simulated Z-direction deformation contours of substrate bottom: (a) measured, Case A; (b) measured, Case B; (c) measured, Case C; (d) simulated, Case A; (e) simulated, Case B; (f) simulated, Case C.

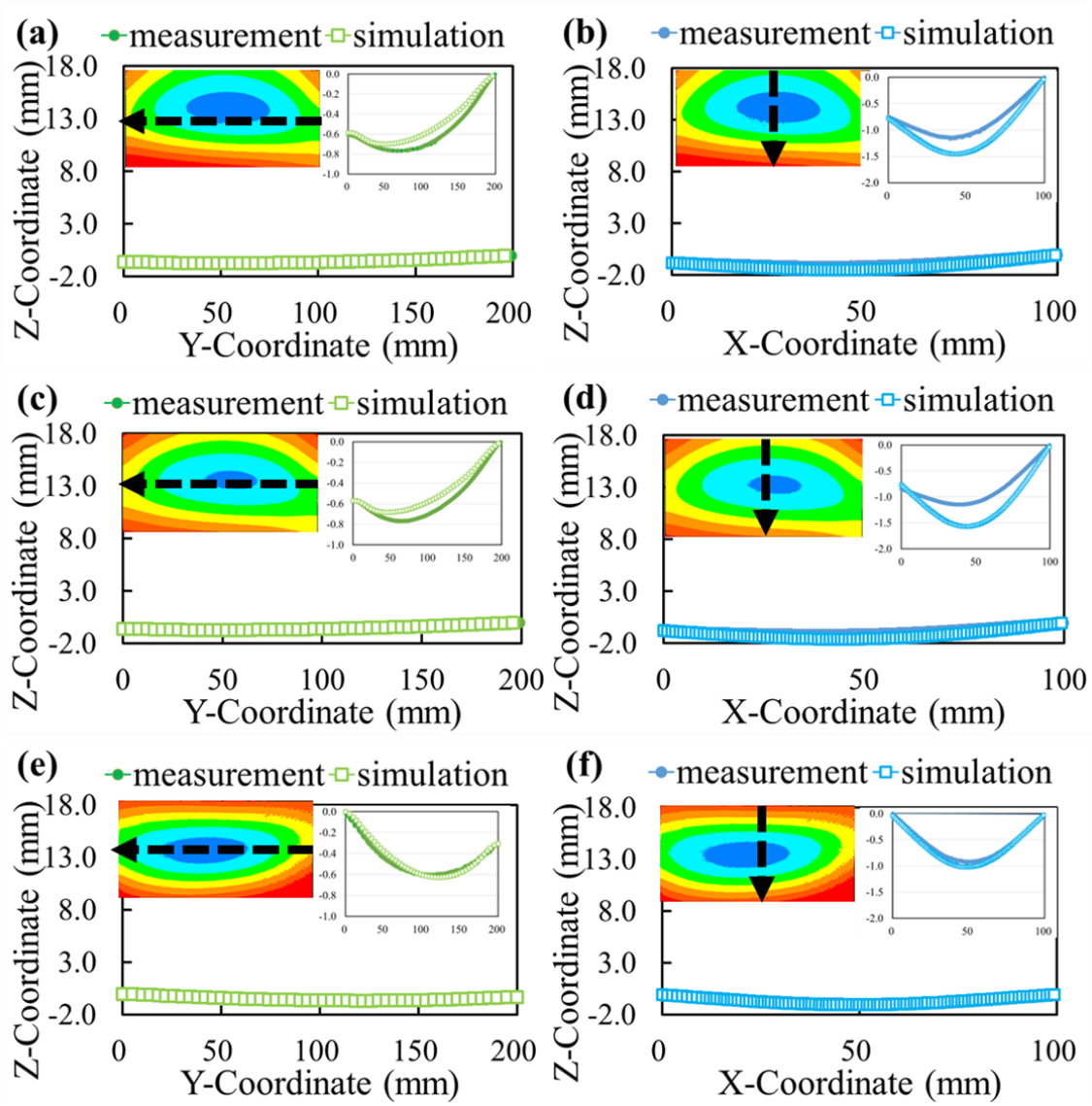

Fig. 5.14. Comparison of measured and simulated Z-direction deformations along the Y- and X-symmetry axes: (a) Y-symmetry axis, Case A; (b) X-symmetry axis, Case A; (c) Y-symmetry axis, Case B; (d) X-symmetry axis, Case B; (e) Y-symmetry axis, Case C; (f) X-symmetry axis, Case C. *The thickness of the substrates was 20 mm.*

For a quantitative comparison between the simulation and measurement results, we extracted the deformation data along the axis of symmetry at the substrate bottom, as shown in Fig.5.14. It is evident that the simulated deformations agreed well with the measured deformations. In Case A, the maximum error between the simulated and

measured deformations in the Z-direction, along the Y-symmetry axis, is approximately 0.1 mm (0.5% of the substrate thickness), whereas the maximum error, along the X-symmetry axis, is approximately 0.3 mm (1.5% of the substrate thickness). In Case B, the maximum error between simulation and measurement for Z-direction deformation is approximately 0.1 mm (0.5% of the substrate thickness) along the Y-symmetry axis, whereas the maximum error is approximately 0.4 mm (2.0% of the substrate thickness) along the X-symmetry axis. The most accurate deformation prediction was provided for Case C. The maximum errors along the Y- and X-symmetry axes were 0.03 mm (0.15% of the substrate thickness) and 0.1 mm (0.5% of the substrate thickness), respectively. The maximum error in all cases was as low as 2.0% of the substrate thickness, indicating high simulation accuracy.

5.4.3. Residual stress analysis

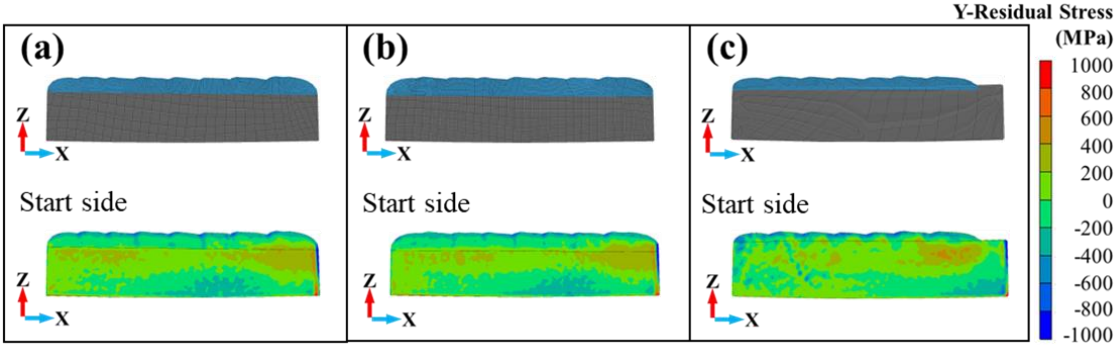

Fig. 5.15. Longitudinal residual stress distributions on the cross-sections measured using the contour method: (a) Case A, (b) Case B, and (c) Case C.

The longitudinal (Y-direction) residual stress distributions on the cross-sections were measured using the contour method, as shown in Fig.5.15. Geometries were created from the actual specimen dimensions for the contour method calculations. A uniform mesh size of 0.5 mm was used for the cross-section. In all cases, the cladding layer exhibited significant compressive residual stress, particularly in the areas near the surface. From

the surface to the bonding interface, the compressive residual stresses gradually decreased and, in some cases, transformed into slight tensile stresses. In the substrate, evident tensile residual stresses existed near both sides of the bonding interface, whereas the residual stresses in the central portion were relatively low. Compressive residual stresses appeared at the center of the substrate bottom, slightly to the right, near the last few cladding passes.

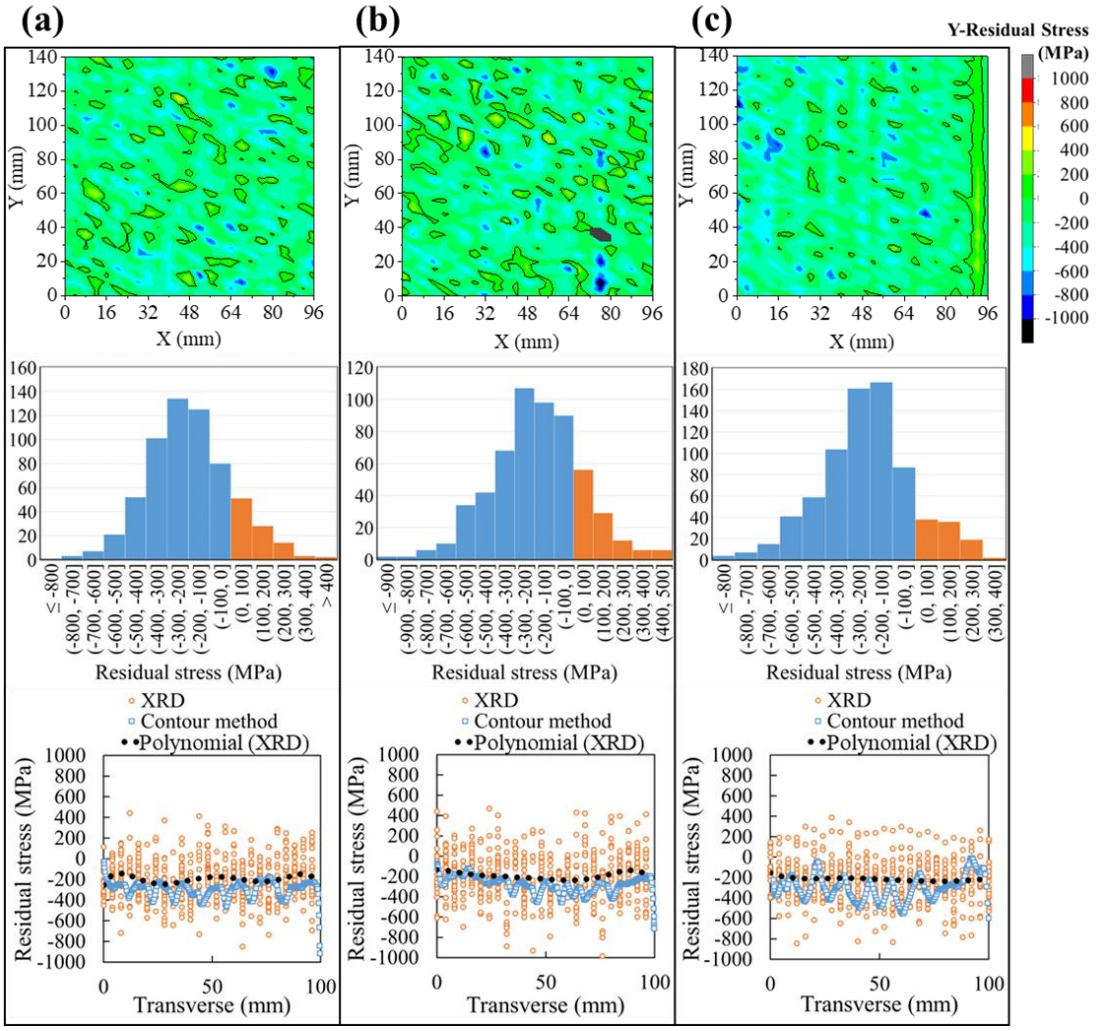

Fig. 5.16. Longitudinal residual stress distributions on the cladding surfaces measured by the XRD method, corresponding stress histograms, and comparison with the contour method measured results: (a) Case A, (b) Case B, and (c) Case C. *The black circles in the contours outline the region of tensile residual stress.*

To verify the contour method measurement results, the longitudinal residual stress distributions on cladding surfaces were measured using the XRD method. The large grain size in the cladding layer made it difficult to measure the stresses, and the measurement error was not controlled within 50 MPa, which formed a limitation of the study. Hence, measurement data with errors exceeding 100 MPa were excluded, after which it was projected onto the corresponding cladding surfaces, as shown in Fig.5.16. To facilitate comparison with the results of the contour method, histograms and polynomial fits (black dotted lines) were applied to process valid measurement data. The circled areas in the contours represent the region of tensile residual stresses, and the remainder indicates compressive residual stresses. As shown in the figure, the measured regions were dominated by compressive residual stresses in all the cases. The unclad surface of Case C exhibited evident tensile residual stresses. In all cases, the residual stresses measured using the XRD method were polynomially fitted and displayed as −200 MPa. The good agreement between the residual stresses measured using the XRD and contour methods supports the validity of the contour method.

Fig.5.17 shows the simulated longitudinal residual stress distributions for the three cases. In all the cases, the cladding surfaces exhibited pronounced compressive residual stresses, which agrees with the results measured by the contour method. The cross-sectional stress distributions show compressive residual stresses up to a depth of 4 mm, essentially covering the entire cladding layer. Cases A, B, and C are similar. The compressive residual stresses in the substrate are concentrated at the bottom center owing to the volume expansion of the cladding layer, whereas the tensile residual stresses appear in the middle and upper portions.

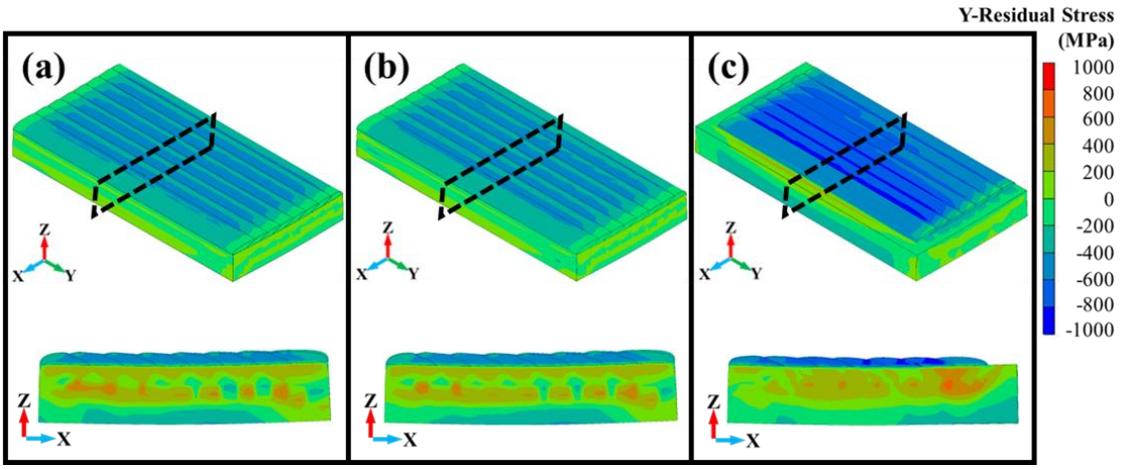

Fig. 5.17. Longitudinal residual stress distributions reproduced by simulations on all specimens and cross-sections: (a) Case A, (b) Case B, and (c) Case C.

To compare the simulation and measurement results further, the longitudinal residual stresses along the black dashed lines in Fig.5.18 were extracted and plotted. In all cases, both the simulated and measured data exhibited high compressive residual stress near the upper surface. As the height decreased, both the simulated and measured data decreased to 0 MPa. In the substrate, both the simulated and measured data showed an increase in tensile residual stress, followed by a decrease, resulting in compressive stress at the bottom. In Case A, the predicted maximum compressive residual stress was −474 MPa, while the measured value was −503 MPa with an error of 5.77 %. In Case B, the predicted maximum compressive residual stress was −475 MPa, while the measured value was −420 MPa with an error of 11.58 %. The compressive residual stress level in the cladding layer of Case C was higher. The predicted maximum compressive residual stress was −711 MPa, while the measured value was −720 MPa with an error of 1.25 %. The simulated residual stresses deviated from the measured values around the HAZ, which may be due to the microstructural changes suggested by the hardness difference in Section

4.1. Because the microstructure of steel is complex and requires more systematic research, this study does not discuss this matter in detail.

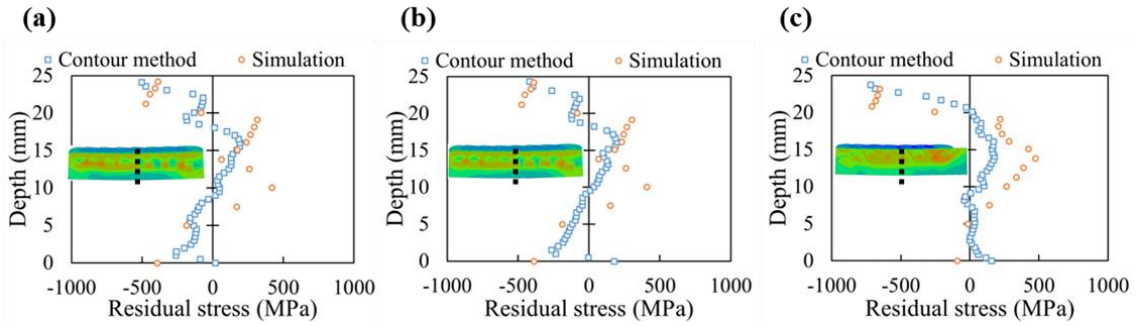

Fig. 5.18. Comparison of simulated and measured longitudinal residual stresses along the Z-direction: (a) Case A, (b) Case B, and (c) Case C.

Fig.5.19 and 20 show the residual stress distributions in the other two directions on the cross-sections. The transverse (X-direction) residual stress distributions were similar to the longitudinal ones. Nonetheless, the transverse constraints were significantly less than the longitudinal constraints owing to the longitudinal cladding and the smaller substrate width. The transverse warping deformations caused by volume expansion of the cladding were weaker. Consequently, no high compressive residual stresses were observed at the bottom of the substrate. The amplitudes of the vertical (Z-direction) residual stresses approached 0 MPa and did not vary significantly with position.

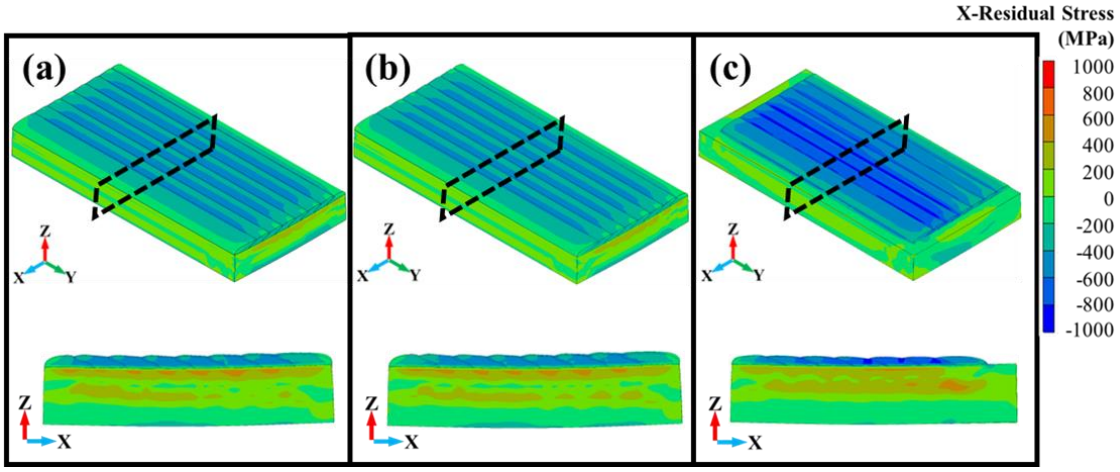

Fig. 5.19. Transverse residual stress distributions reproduced by simulations on all specimens and cross-sections: (a) Case A, (b) Case B, and (c) Case C.

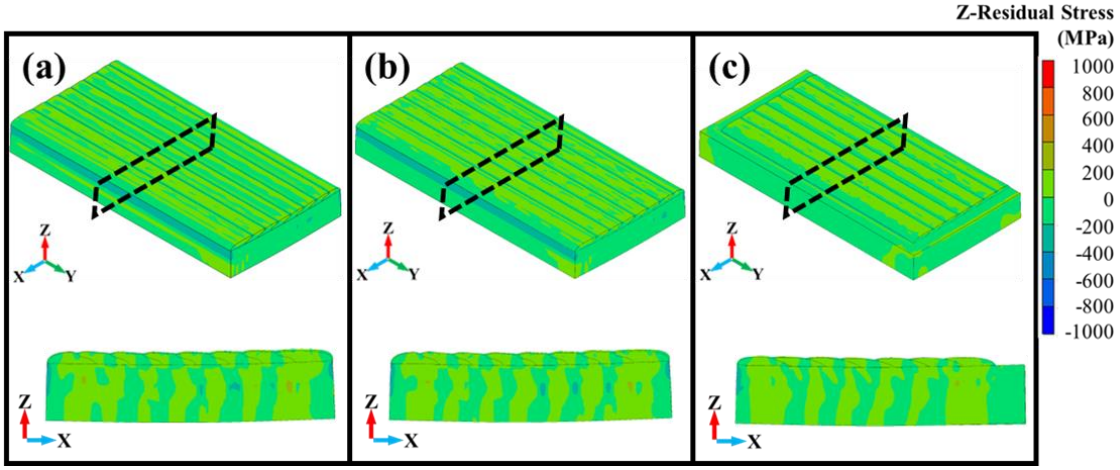

Fig. 5.20. Vertical residual stress distributions reproduced by simulations on all specimens and cross-sections: (a) Case A, (b) Case B, and (c) Case C.

In the three cases, compressive residual stresses in the X- and Y-directions were generated in the cladding layer. Case A was designed under normal manufacturing conditions and did not consider the interpass temperature. Case B had an interpass temperature control that required an interpass temperature above 270 °C. This condition was implemented to synchronize the phase transformation of all the cladding passes,

ensuring that they commenced simultaneously during the final cooling period. The stress-balancing effect can be avoided, and the generation of compressive residual stresses in all the cladding passes is guaranteed. Specifically, Case B is a specification requirement for the use of the 16Cr8Ni-LTT. Considering the dimensions of the object and limitations of the equipment in industrial production, manufacturing conditions without interpass temperature control, such as Case A, have become a more practical solution. It was demonstrated that Case A achieved almost the same effect as Case B. However, owing to the small size of the specimen in this study, the interpass temperature in Case A was stable at approximately 300 ℃ (higher than 270 °C) and the cladding passes can undergo a simultaneous phase transformation. For larger specimens, the temperature gradient on the substrate is more significant, leading to sequential phase transformations [43,44]. Therefore, in Case C, the interpass temperature of 50 ℃ was required to be lower than the martensite transformation finish (Mf) temperature, ensuring that the cladding passes sequentially underwent phase transformation.

To understand Case C better, the temperature and stress histories at the position of the first pass in Fig.5.21 were extracted and plotted. It can be observed that the temperature reaches Ac1 (austenite transformation start temperature) only during the first pass of cladding. After the first pass, the temperature dropped to 50 °C, such that all austenite was transformed into martensite. During subsequent thermal cycles, martensite was retained without austenitic-phase transformation. Thus, 16Cr8Ni-LTT can be regarded as a material in which no phase transformation had occurred. Although no new martensite phase transformation occurred, the initially generated compressive residual stress persisted. The expansion and contraction of the martensite in response to temperature changes resulted in little additional tensile residual stress. The increase in the maximum

tensile stress observed during the second and third thermal cycles is attributable to the stress-balancing effect produced by adjacent subsequent martensite phase transformations. This phenomenon disappears as the cladding process continues. In summary, although 16Cr8Ni-LTT exhibits high sensitivity to thermal cycling, the cladding circumvents the bottleneck that would otherwise exist in WAAM, ensuring that the compressive residual stresses generated throughout the cladding layer are not affected. This allows 16Cr8Ni-LTT to generate compressive residual stresses without the need for strict control of the interpass temperatures, which greatly supports the applicability and availability of 16Cr8Ni-LTT in claddings.

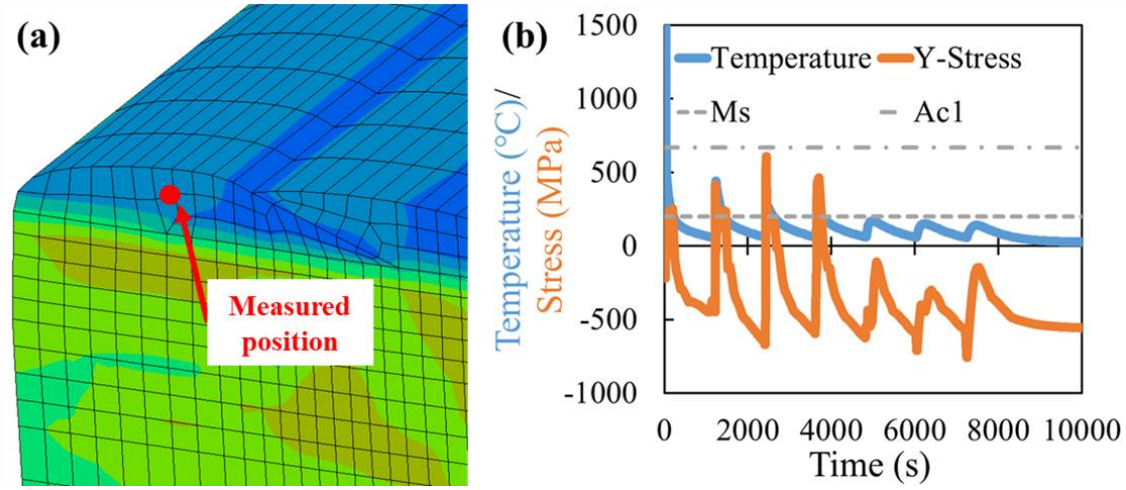

Fig. 5.21. Temperature and longitudinal-stress histories at the middle of the first pass in Case C: (a) measured position and (b) temperature and stress versus time curves.

5.5. Brief discussion of residual stress in the practical pipe cladding

The effectiveness of 16Cr8Ni-LTT cladding on flat plates has been confirmed, but whether 16Cr8Ni-LTT can continue to be useful for pipeline structures with more complex stress states requires further study. In this subsection, the residual stress state of

16Cr8Ni-LTT cladding on the inner wall of a practical metal pipe structure is predicted using a validated finite element model in the absence of experiments. The substrate and cladding materials are consistent with those in this chapter, and the pipe thicknesses are referenced to the substrate thicknesses in this chapter.

Figure 5.21 gives the FE model diagram of the pipe cladding case and a three-point constraint is applied as a boundary condition in the simulation. The inner diameter of the pipe is 194 mm, the outer diameter is 220 mm, the length of the pipe is taken as 50mm, the cladding is carried out five times, the width of one is 10mm, the thickness is 3mm, and the direction of the cladding is along the circumference.

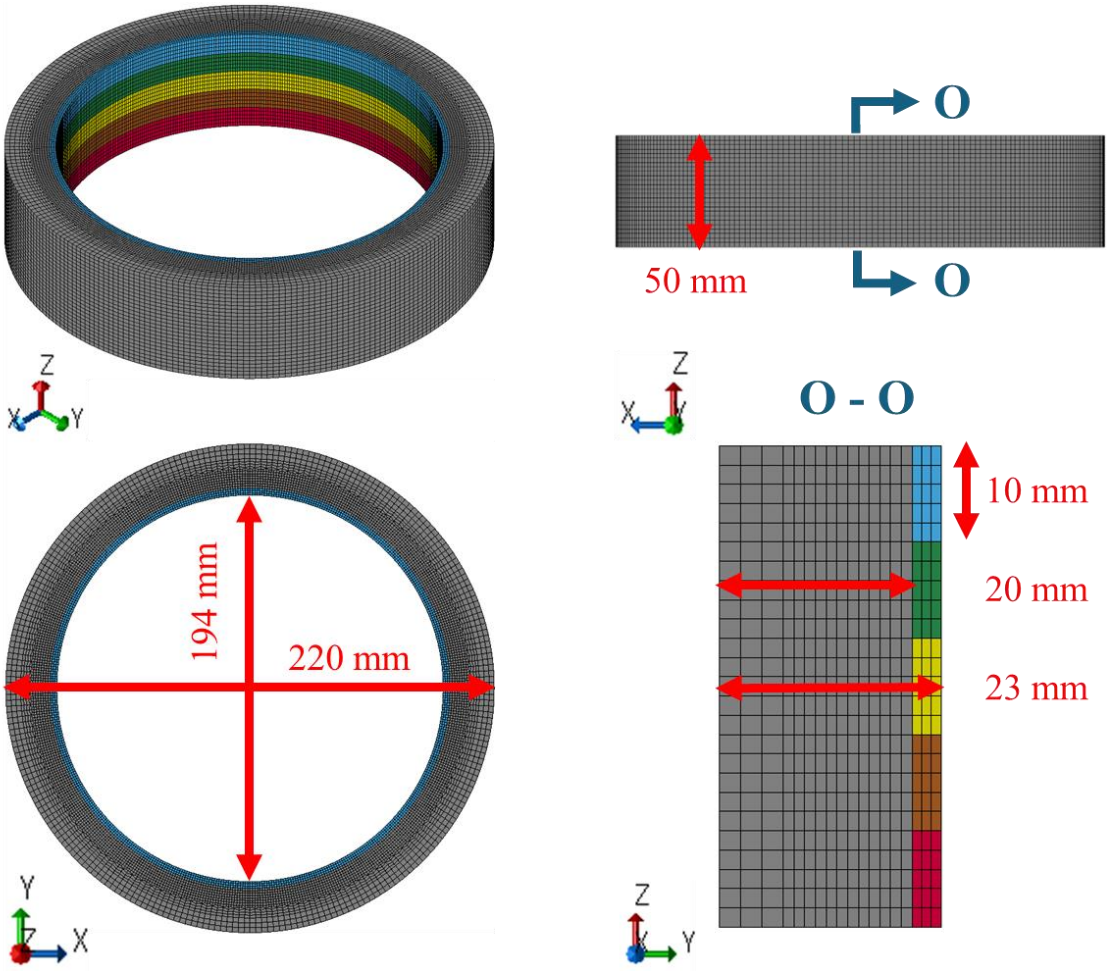

Fig. 5.22. The FE model diagrams of pipe-cladding.

All parameters are referenced in Section 5.3.2, followed by the residual stress analysis. Figure 5.23 illustrates the residual stress distribution in three directions. The residual stress distribution in the X and Y directions of the one-half model indicates that the circumferential residual stresses remain as compressive residual stresses. The distribution in the cross-section is depicted in the residual stress contour at the lower left. The entire cladding is characterized by significant compressive residual stresses, approximately -500 MPa. The substrate near the cladding also exhibits compressive residual stresses, whereas the mid-layer portion is characterized by tensile residual stresses. Eventually, the residual stresses level off in the bottom layer of the substrate. For residual stresses in the direction perpendicular to the observed cross-section, the Z direction, the distribution is similar to that in the X direction, although the overall residual stress level is lower. In contrast, the residual stresses in the Y direction of the observation cross-section are not significant and exhibit a lower level.

Based on the above analysis, it is evident that even in more complex structures, 16Cr8Ni-LTT cladding can still generate sufficient compressive residual stress to optimize the performance of the substrate surface. The stability of the conclusions drawn in this chapter is well-verified. Further experiments are required to validate the accuracy of the simulations and to quantitatively assess the improvement in surface performance.

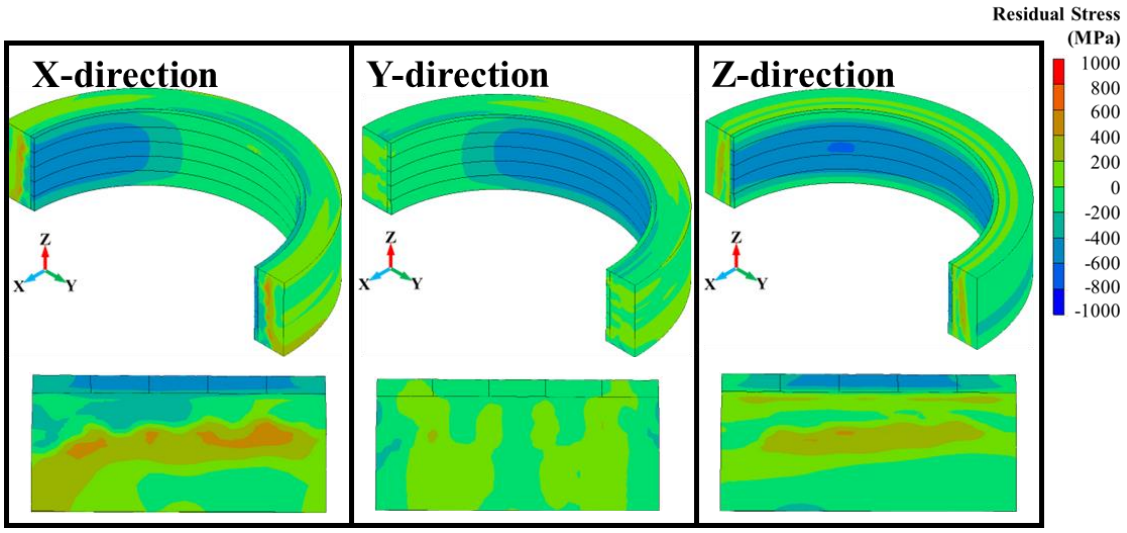

Fig.5.23. The residual stress distribution of pipe cladding in three directions.

5.6. Conclusions

In this study, 16Cr8Ni-LTT was utilized for cladding KA36 substrates using the WAAM technique with three distinct interpass temperature control strategies. These strategies were investigated using experimental measurements and numerical simulations. It is expected to provide scientific insights for eliciting compressive residual stresses through cladding LTT materials via WAAM. The key conclusions are as follows:

(1) The residual stress distributions on the cladding surfaces and cross-sections were measured using XRD and contour methods. The measurement results from both methods agreed well with each other, ensuring the accuracy and reliability of the measurements.

(2) The simulated and measured cooling histories were in good agreement, indicating a high temperature-prediction accuracy of the model. The simulated temperature distributions, combined with hardness testing, were used to identify the HAZ depth and temperature for each case.

(3) The simulated substrate deformations matched the measured deformations well, with all cases exhibiting upward warping on all sides. The deviation of the simulated and measured maximum deflections in each case was within 0.4 mm, which is acceptable compared to the substrate thickness (20 mm).

(4) The high accuracy of the model in predicting residual stresses was validated by comparing the simulated residual stresses with those measured by the contour method in all cases. The error in the maximum compressive residual stress was less than 12%. Both longitudinal and transverse residual stresses were compressive in cladding LTT materials.

(5) Interpass temperature-control strategies were also investigated. It was determined that strictly controlling the interpass temperature above Ms to achieve simultaneous phase transformations in all passes is not necessary for compressive residual stresses when cladding LTT materials.

This study provides scientific insights into LLT-induced compressive residual stresses and highlights the superiority and flexibility of cladding LTT materials via WAAM for improving the resistance of large metal components to fatigue and corrosion.

Chapter 6. Conclusions and suggestions for future work

Wire Arc Additive Manufacturing (WAAM) has gained prominence as a method for fabricating large-scale metal components with reduced material waste and production time. Central to WAAM's challenges is the control of residual stresses and deformation characteristics, crucial for structural integrity. The utilization of Low Transformation Temperature (LTT) materials has emerged as a promising approach to address these challenges. This paper synthesizes findings from various studies on WAAM and LTT materials to draw conclusions and suggest avenues for future work.

In Chapter 3:

I. Successfully fabricated wall and pipe parts using WAAM.
II. Developed a thermomechanical coupling WAAM model to study residual stress formation and its relationship with deposition height and shape.
III. Concluded that tensile residual stresses exist at deposition layers, with a maximum value of approximately 300 MPa several layers below the top.
IV. Identified a quasi-stable state of residual stress distribution with a tensile-compressive-tensile pattern in structures with larger deposition heights.

In Chapter 4:

I. Used an LTT material (10Cr-10Ni) in WAAM to fabricate pipe structures and analyzed substrate deformation and residual stress distribution.
II. The compressive residual stresses were concentrated near the top of the deposition section. The maximum compressive residual stress was -200 MPa.
III. The thickness causing compressive residual stresses due to LTT was about 6 mm in the tube part.

In Chapter 5:

I. Utilized 16Cr8Ni-LTT for cladding KA36 substrates via WAAM with different interpass temperature control strategies.
II. Validated residual stress distributions and substrate deformations through experimental measurements and numerical simulations.
III. Concluded that compressive residual stresses in cladding LTT materials can be achieved without strictly controlling interpass temperatures above Ms, offering insights into improving resistance to fatigue and corrosion.

In conclusion, this dissertation provides a comprehensive analysis of residual stress distributions, deformation characteristics, and phase transformations in WAAM-fabricated components using LTT materials. The findings contribute significantly to advancing knowledge in the field and lay a foundation for continued innovation and improvement in WAAM production.

In future research, I think the following aspects have the value of being investigated. First, the current simulation of phase change materials mainly relies on the instantaneous thermal expansion coefficient. However, the corresponding residual stresses calculated at the junction of phase-change materials and non-phase-change materials have an unnatural transition. There is a large discrepancy with the experimental results. In order to improve the accuracy of the simulation, on the one hand, the existing material model can be corrected. On the other hand, the variation of material properties within the heat affected zone is also an important aspect. This involves further observation and identification of the microstructure of the heat-affected zone and recalibration of the material properties. Secondly, although some progress has been made in the application of LTT materials in cladding, how to evaluate the mechanical properties of the finished products is still in the

investigation stage. Especially for the fatigue performance, corrosion resistance needs to design specialized experiments for verification. Thirdly, the application of LTT remains in the rationalized condition, and there is a lack of research on the cladding of actual shaped parts. For example, cladding on pipe walls involves more complex processes and conditions, and further research is needed to determine whether the results in the ideal mode can be achieved. Considering the dilution phenomenon of LTT in cladding, experiments, and simulations for different substrates are also very important.

References

[1] Prakash KS, Nancharaih T, Rao VVS. ScienceDirect Additive Manufacturing Techniques in Manufacturing-An Overview. 2017.

[2] Huang SH, Liu P, Mokasdar A, Hou L. Additive manufacturing and its societal impact: A literature review. International Journal of Advanced Manufacturing Technology 2013;67:1191–203. https://doi.org/10.1007/s00170-012-4558-5.

[3] Bikas H, Stavropoulos P, Chryssolouris G. Additive manufacturing methods and modeling approaches: A critical review. International Journal of Advanced Manufacturing Technology 2016;83:389–405. https://doi.org/10.1007/s00170-015-7576-2.

[4] Bourell D, Kruth JP, Leu M, Levy G, Rosen D, Beese AM, et al. Materials for additive manufacturing. CIRP Ann Manuf Technol 2017;66:659–81. https://doi.org/10.1016/j.cirp.2017.05.009.

[5] Javaid Mohd, Haleem A. Additive manufacturing applications in medical cases: A literature based review. Alexandria Journal of Medicine 2018;54:411–22. https://doi.org/10.1016/j.ajme.2017.09.003.

[6] Huang SH, Liu P, Mokasdar A, Hou L. Additive manufacturing and its societal impact: A literature review. International Journal of Advanced Manufacturing Technology 2013;67:1191–203. https://doi.org/10.1007/s00170-012-4558-5.

[7] Delgado Camacho D, Clayton P, O'Brien WJ, Seepersad C, Juenger M, Ferron R, et al. Applications of additive manufacturing in the construction industry – A forward-looking review. Autom Constr 2018;89:110–9. https://doi.org/10.1016/j.autcon.2017.12.031.

[8] Gao W, Zhang Y, Ramanujan D, Ramani K, Chen Y, Williams CB, et al. The status, challenges, and future of additive manufacturing in engineering. CAD Computer Aided Design 2015;69:65–89. https://doi.org/10.1016/j.cad.2015.04.001.

[9] Kristiawan RB, Imaduddin F, Ariawan D, Ubaidillah, Arifin Z. A review on the fused deposition modeling (FDM) 3D printing: Filament processing, materials, and printing parameters. Open Engineering 2021;11:639–49. https://doi.org/10.1515/eng-2021-0063.

[10] Dizon JRC, Espera AH, Chen Q, Advincula RC. Mechanical characterization of 3D-printed polymers. Addit Manuf 2018;20:44–67. https://doi.org/10.1016/j.addma.2017.12.002.

[11] Sanchez S, Smith P, Xu Z, Gaspard G, Hyde CJ, Wits WW, et al. Powder Bed Fusion of nickel-based superalloys: A review. Int J Mach Tools Manuf 2021;165. https://doi.org/10.1016/j.ijmachtools.2021.103729.

[12] Chatham CA, Long TE, Williams CB. A review of the process physics and material screening methods for polymer powder bed fusion additive manufacturing. Prog Polym Sci 2019;93:68–95. https://doi.org/10.1016/j.progpolymsci.2019.03.003.

[13] Bartlett JL, Li X. An overview of residual stresses in metal powder bed fusion. Addit Manuf 2019;27:131–49. https://doi.org/10.1016/j.addma.2019.02.020.

[14] Sanaei N, Fatemi A, Phan N. Defect characteristics and analysis of their variability in metal L-PBF additive manufacturing. Mater Des 2019;182. https://doi.org/10.1016/j.matdes.2019.108091.

[15] Dev Singh D, Mahender T, Raji Reddy A. Powder bed fusion process: A brief review. Mater Today Proc, vol. 46, Elsevier Ltd; 2021, p. 350–5. https://doi.org/10.1016/j.matpr.2020.08.415.

[16] Pazhamannil RV, Govindan P. Current state and future scope of additive manufacturing technologies via vat photopolymerization. Mater Today Proc, vol. 43, Elsevier Ltd; 2020, p. 130–6. https://doi.org/10.1016/j.matpr.2020.11.225.

[17] Al Rashid A, Ahmed W, Khalid MY, Koç M. Vat photopolymerization of polymers and polymer composites: Processes and applications. Addit Manuf 2021;47. https://doi.org/10.1016/j.addma.2021.102279.

[18] Zhang F, Zhu L, Li Z, Wang S, Shi J, Tang W, et al. The recent development of vat photopolymerization: A review. Addit Manuf 2021;48. https://doi.org/10.1016/j.addma.2021.102423.

[19] Meenakshisundaram V, Sturm LD, Williams CB. Modeling A Scanning-Mask Projection Vat Photopolymerization System For Multiscale Additive Manufacturing. J Mater Process Technol 2020;279. https://doi.org/10.1016/j.jmatprotec.2019.116546.

[20] Wu X, Teng J, Ji X, Xu C, Ma D, Sui S, et al. Research progress of the defects and innovations of ceramic vat photopolymerization. Addit Manuf 2023;65. https://doi.org/10.1016/j.addma.2023.103441.

[21] Pagac M, Hajnys J, Ma QP, Jancar L, Jansa J, Stefek P, et al. A review of vat photopolymerization technology: Materials, applications, challenges, and future trends of 3d printing. Polymers (Basel) 2021;13:1–20. https://doi.org/10.3390/polym13040598.

[22] Hayes B, Hainsworth T, MacCurdy R. Liquid–solid co-printing of multi-material 3D fluidic devices via material jetting. Addit Manuf 2022;55. https://doi.org/10.1016/j.addma.2022.102785.

[23] Elkaseer A, Chen KJ, Janhsen JC, Refle O, Hagenmeyer V, Scholz SG. Material jetting for advanced applications: A state-of-the-art review, gaps and future directions. Addit Manuf 2022;60. https://doi.org/10.1016/j.addma.2022.103270.

[24] Mueller J, Shea K, Daraio C. Mechanical properties of parts fabricated with inkjet 3D printing through efficient experimental design. Mater Des 2015;86:902–12. https://doi.org/10.1016/j.matdes.2015.07.129.

[25] Yang H, Lim JC, Liu Y, Qi X, Yap YL, Dikshit V, et al. Performance evaluation of ProJet multi-material jetting 3D printer. Virtual Phys Prototyp 2017;12:95–103. https://doi.org/10.1080/17452759.2016.1242915.

[26] Tee YL, Tran P, Leary M, Pille P, Brandt M. 3D Printing of polymer composites with material jetting: Mechanical and fractographic analysis. Addit Manuf 2020;36. https://doi.org/10.1016/j.addma.2020.101558.

[27] Li M, Du W, Elwany A, Pei Z, Ma C. Metal binder jetting additive manufacturing: A literature review. Journal of Manufacturing Science and Engineering, Transactions of the ASME 2020;142. https://doi.org/10.1115/1.4047430.

[28] Ziaee M, Crane NB. Binder jetting: A review of process, materials, and methods. Addit Manuf 2019;28:781–801. https://doi.org/10.1016/j.addma.2019.05.031.

[29] Stevens E, Schloder S, Bono E, Schmidt D, Chmielus M. Density variation in binder jetting 3D-printed and sintered Ti-6Al-4V. Addit Manuf 2018;22:746–52. https://doi.org/10.1016/j.addma.2018.06.017.

[30] Mostafaei A, Elliott AM, Barnes JE, Li F, Tan W, Cramer CL, et al. Binder jet 3D printing—Process parameters, materials, properties, modeling, and challenges. Prog Mater Sci 2021;119. https://doi.org/10.1016/j.pmatsci.2020.100707.

[31] Mostafaei A, Stevens EL, Ference JJ, Schmidt DE, Chmielus M. Binder jetting of a complex-shaped metal partial denture framework. Addit Manuf 2018;21:63–8. https://doi.org/10.1016/j.addma.2018.02.014.

[32] Kumar A, Bai Y, Eklund A, Williams CB. Effects of Hot Isostatic Pressing on Copper Parts Fabricated via Binder Jetting. Procedia Manuf, vol. 10, Elsevier B.V.; 2017, p. 935–44. https://doi.org/10.1016/j.promfg.2017.07.084.

[33] Himmer T, Nakagawa T, Anzai M. Lamination of metal sheets. vol. 39. n.d.

[34] Zhang Y, He X, Han J, Du S, Zhang J. Al 2 O 3 Ceramics Preparation by LOM (Laminated Object Manufacturing). vol. 17. 2001.

[35] Paul BK, Voorakarnam V. Effect of layer thickness and orientation angle on surface roughness in laminated object manufacturing. J Manuf Process 2001;3:94–101. https://doi.org/10.1016/S1526-6125(01)70124-7.

[36] Bhatt PM, Kabir AM, Peralta M, Bruck HA, Gupta SK. A robotic cell for performing sheet lamination-based additive manufacturing. Addit Manuf 2019;27:278–89. https://doi.org/10.1016/j.addma.2019.02.002.

[37] Svetlizky D, Das M, Zheng B, Vyatskikh AL, Bose S, Bandyopadhyay A, et al. Directed energy deposition (DED) additive manufacturing: Physical characteristics, defects, challenges and applications. Materials Today 2021;49:271–95. https://doi.org/10.1016/j.mattod.2021.03.020.

[38] Tavlovich B, Shirizly A, Katz R. EBW and LBW of additive manufactured H6AI4V products. Weld J 2018;97:179s–90s. https://doi.org/10.29391/2018.97.016.

[39] Mishra GK, Paul CP, Rai AK, Agrawal AK, Rai SK, Bindra KS. Experimental investigation on Laser Directed Energy Deposition based additive manufacturing

of Al2O3 bulk structures. Ceram Int 2021;47:5708–20. https://doi.org/10.1016/j.ceramint.2020.10.157.

[40] Tümer M, Pixner F, Vallant R, Domitner J, Enzinger N. Mechanical and microstructural properties of S1100 UHSS welds obtained by EBW and MAG welding. Welding in the World 2022;66:1199–211. https://doi.org/10.1007/s40194-022-01276-7.

[41] Carroll BE, Otis RA, Borgonia JP, Suh JO, Dillon RP, Shapiro AA, et al. Functionally graded material of 304L stainless steel and inconel 625 fabricated by directed energy deposition: Characterization and thermodynamic modeling. Acta Mater 2016;108:46–54. https://doi.org/10.1016/j.actamat.2016.02.019.

[42] Huang CA, Wang TH, Lee CH, Han WC. A study of the heat-affected zone (HAZ) of an Inconel 718 sheet welded with electron-beam welding (EBW). Materials Science and Engineering: A 2005;398:275–81. https://doi.org/10.1016/j.msea.2005.03.029.

[43] Bhardwaj T, Shukla M, Paul CP, Bindra KS. Direct Energy Deposition - Laser Additive Manufacturing of Titanium-Molybdenum alloy: Parametric studies, microstructure and mechanical properties. J Alloys Compd 2019;787:1238–48. https://doi.org/10.1016/j.jallcom.2019.02.121.

[44] Raut LP, Taiwade R V. Wire Arc Additive Manufacturing: A Comprehensive Review and Research Directions. J Mater Eng Perform 2021;30:4768–91. https://doi.org/10.1007/s11665-021-05871-5.

[45] Singh SR, Khanna P. Wire arc additive manufacturing (WAAM): A new process to shape engineering materials. Mater Today Proc, vol. 44, Elsevier Ltd; 2021, p. 118–28. https://doi.org/10.1016/j.matpr.2020.08.030.

[46] Li JLZ, Alkahari MR, Rosli NAB, Hasan R, Sudin MN, Ramli FR. Review of wire arc additive manufacturing for 3d metal printing. International Journal of Automation Technology 2019;13:346–53. https://doi.org/10.20965/ijat.2019.p0346.

[47] Williams SW, Martina F, Addison AC, Ding J, Pardal G, Colegrove P. Wire + Arc additive manufacturing. Materials Science and Technology (United Kingdom) 2016;32:641–7. https://doi.org/10.1179/1743284715Y.0000000073.

[48] Nandan G, Kumar G, Arora KS, Kumar A. MIG and CMT brazing of aluminum alloys and steel: A review. Mater Today Proc 2022;56:481–8. https://doi.org/10.1016/j.matpr.2022.02.166.

[49] Singh S, Kumar V, Kumar S, Kumar A. Variant of MIG welding of similar and dissimilar metals: A review. Mater Today Proc 2022:3550–5. https://doi.org/10.1016/j.matpr.2021.11.287.

[50] Srinivasan D, Sevvel P, John Solomon I, Tanushkumaar P. A review on Cold Metal Transfer (CMT) technology of welding. Mater Today Proc 2022;64:108–15. https://doi.org/10.1016/j.matpr.2022.04.016.

[51] Raj D, Singari RM, Vipin M. Study and analyses of arc length correction and mechanical properties on weld bead geometry for AA6061T6 by CMT process. Mater Today Proc 2022;56:3475–83. https://doi.org/10.1016/j.matpr.2021.11.122.

[52] Karhu M, Kujanpää V. Gas tungsten arc process optimization and assessment for robotized position welding of austenitic stainless steel edge joints. CIRP J Manuf Sci Technol 2022;36:12–22. https://doi.org/10.1016/j.cirpj.2021.10.012.

[53] Tseng KH, Hsu CY. Performance of activated TIG process in austenitic stainless steel welds. J Mater Process Technol 2011;211:503–12. https://doi.org/10.1016/j.jmatprotec.2010.11.003.

[54] Sahoo A, Tripathy S. Development in plasma arc welding process: A review. Mater Today Proc, vol. 41, Elsevier Ltd; 2019, p. 363–8. https://doi.org/10.1016/j.matpr.2020.09.562.

[55] NUMERICAL INVESTIGATIONS OF THE INFLUENCE OF DESIGN PARAMETERS, GAS COMPOSITION AND ELECTRIC CURRENT IN PLASMA ARC WELDING-Peer-reviewed Section. n.d.

[56] Li H, Zou J, Yao J, Peng H. The effect of TIG welding techniques on microstructure, properties and porosity of the welded joint of 2219 aluminum alloy. J Alloys Compd 2017;727:531–9. https://doi.org/10.1016/j.jallcom.2017.08.157.

[57] Wu CS, Wang L, Ren WJ, Zhang XY. Plasma arc welding: Process, sensing, control and modeling. J Manuf Process 2014;16:74–85. https://doi.org/10.1016/j.jmapro.2013.06.004.

[58] Chen X, Su C, Wang Y, Siddiquee AN, Konovalov S, Jayalakshmi S, et al. Cold Metal Transfer (CMT) Based Wire and Arc Additive Manufacture (WAAM) System. Journal of Surface Investigation 2018;12:1278–84. https://doi.org/10.1134/S102745101901004X.

[59] Prado-Cerqueira JL, Diéguez JL, Camacho AM. Preliminary development of a Wire and Arc Additive Manufacturing system (WAAM). Procedia Manuf 2017;13:895–902. https://doi.org/10.1016/j.promfg.2017.09.154.

[60] Nagamatsu H, Sasahara H, Mitsutake Y, Hamamoto T. Development of a cooperative system for wire and arc additive manufacturing and machining. Addit Manuf 2020;31. https://doi.org/10.1016/j.addma.2019.100896.

[61] Busachi A, Erkoyuncu J, Colegrove P, Martina F, Ding J. Designing a WAAM based manufacturing system for defence applications. Procedia CIRP, vol. 37, Elsevier B.V.; 2015, p. 48–53. https://doi.org/10.1016/j.procir.2015.08.085.

[62] Ding D, He F, Yuan L, Pan Z, Wang L, Ros M. The first step towards intelligent wire arc additive manufacturing: An automatic bead modelling system using machine learning through industrial information integration. J Ind Inf Integr 2021;23. https://doi.org/10.1016/j.jii.2021.100218.

[63] Wang J, Pan Z, Ma Y, Lu Y, Shen C, Cuiuri D, et al. Characterization of wire arc additively manufactured titanium aluminide functionally graded material: Microstructure, mechanical properties and oxidation behaviour. Materials Science and Engineering: A 2018;734:110–9. https://doi.org/10.1016/j.msea.2018.07.097.

[64] Lin Z, Song K, Yu X. A review on wire and arc additive manufacturing of titanium alloy. J Manuf Process 2021;70:24–45. https://doi.org/10.1016/j.jmapro.2021.08.018.

[65] Thapliyal S. Challenges associated with the wire arc additive manufacturing (WAAM) of aluminum alloys. Mater Res Express 2019;6. https://doi.org/10.1088/2053-1591/ab4dd4.

[66] Dhinakaran V, Ajith J, Fathima Yasin Fahmidha A, Jagadeesha T, Sathish T, Stalin B. Wire Arc Additive Manufacturing (WAAM) process of nickel based superalloys-A review. Mater Today Proc, vol. 21, Elsevier Ltd; 2020, p. 920–5. https://doi.org/10.1016/j.matpr.2019.08.159.

[67] Jin W, Zhang C, Jin S, Tian Y, Wellmann D, Liu W. Wire arc additive manufacturing of stainless steels: A review. Applied Sciences (Switzerland) 2020;10. https://doi.org/10.3390/app10051563.

[68] Shi X, Ma S, Liu C, Wu Q, Lu J, Liu Y, et al. Selective laser melting-wire arc additive manufacturing hybrid fabrication of Ti-6Al-4V alloy: Microstructure and mechanical properties. Materials Science and Engineering: A 2017;684:196–204. https://doi.org/10.1016/j.msea.2016.12.065.

[69] Szost BA, Terzi S, Martina F, Boisselier D, Prytuliak A, Pirling T, et al. A comparative study of additive manufacturing techniques: Residual stress and microstructural analysis of CLAD and WAAM printed Ti-6Al-4V components. Mater Des 2016;89:559–67. https://doi.org/10.1016/j.matdes.2015.09.115.

[70] Ng CH, Bermingham MJ, Kent D, Dargusch MS. High stability and high strength β-titanium alloys for additive manufacturing. Materials Science and Engineering: A 2021;816. https://doi.org/10.1016/j.msea.2021.141326.

[71] Wang F, Williams S, Colegrove P, Antonysamy AA. Microstructure and mechanical properties of wire and arc additive manufactured Ti-6Al-4V. Metall Mater Trans A Phys Metall Mater Sci 2013;44:968–77. https://doi.org/10.1007/s11661-012-1444-6.

[72] Kennedy JR, Davis AE, Caballero AE, Williams S, Pickering EJ, Prangnell PB. The potential for grain refinement of Wire-Arc Additive Manufactured (WAAM) Ti-6Al-4V by ZrN and TiN inoculation. Addit Manuf 2021;40. https://doi.org/10.1016/j.addma.2021.101928.

[73] Qi Z, Qi B, Cong B, Sun H, Zhao G, Ding J. Microstructure and mechanical properties of wire + arc additively manufactured 2024 aluminum alloy

components: As-deposited and post heat-treated. J Manuf Process 2019;40:27–36. https://doi.org/10.1016/j.jmapro.2019.03.003.

[74] Campatelli G, Campanella D, Barcellona A, Fratini L, Grossi N, Ingarao G. Microstructural, mechanical and energy demand characterization of alternative WAAM techniques for Al-alloy parts production. CIRP J Manuf Sci Technol 2020;31:492–9. https://doi.org/10.1016/j.cirpj.2020.08.001.

[75] Çam G. Prospects of producing aluminum parts by wire arc additive manufacturing (WAAM). Mater Today Proc 2022;62:77–85. https://doi.org/10.1016/j.matpr.2022.02.137.

[76] Wang H, Jiang W, Ouyang J, Kovacevic R. Rapid prototyping of 4043 Al-alloy parts by VP-GTAW. J Mater Process Technol 2004;148:93–102. https://doi.org/10.1016/j.jmatprotec.2004.01.058.

[77] Ouyang JH, Wang H, Kovacevic R. Rapid prototyping of 5356-aluminum alloy based on variable polarity gas tungsten arc welding: Process control and microstructure. Materials and Manufacturing Processes 2002;17:103–24. https://doi.org/10.1081/AMP-120002801.

[78] Lan B, Wang Y, Liu Y, Hooper P, Hopper C, Zhang G, et al. The influence of microstructural anisotropy on the hot deformation of wire arc additive manufactured (WAAM) Inconel 718. Materials Science and Engineering: A 2021;823. https://doi.org/10.1016/j.msea.2021.141733.

[79] Wu B, Qiu Z, Pan Z, Carpenter K, Wang T, Ding D, et al. Enhanced interface strength in steel-nickel bimetallic component fabricated using wire arc additive manufacturing with interweaving deposition strategy. J Mater Sci Technol 2020;52:226–34. https://doi.org/10.1016/j.jmst.2020.04.019.

[80] Ke WC, Oliveira JP, Cong BQ, Ao SS, Qi ZW, Peng B, et al. Multi-layer deposition mechanism in ultra high-frequency pulsed wire arc additive manufacturing (WAAM) of NiTi shape memory alloys. Addit Manuf 2022;50. https://doi.org/10.1016/j.addma.2021.102513.

[81] Zeng Z, Cong BQ, Oliveira JP, Ke WC, Schell N, Peng B, et al. Wire and arc additive manufacturing of a Ni-rich NiTi shape memory alloy: Microstructure and mechanical properties. Addit Manuf 2020;32. https://doi.org/10.1016/j.addma.2020.101051.

[82] Tanvir ANM, Ahsan MRU, Ji C, Hawkins W, Bates B, Kim DB. Heat treatment effects on Inconel 625 components fabricated by wire + arc additive manufacturing (WAAM)—part 1: microstructural characterization. International Journal of Advanced Manufacturing Technology 2019. https://doi.org/10.1007/s00170-019-03828-6.

[83] Laghi V, Palermo M, Gasparini G, Veljkovic M, Trombetti T. Assessment of design mechanical parameters and partial safety factors for Wire-and-Arc Additive Manufactured stainless steel. Eng Struct 2020;225. https://doi.org/10.1016/j.engstruct.2020.111314.

[84] Wang L, Xue J, Wang Q. Correlation between arc mode, microstructure, and mechanical properties during wire arc additive manufacturing of 316L stainless steel. Materials Science and Engineering: A 2019;751:183–90. https://doi.org/10.1016/j.msea.2019.02.078.

[85] Le VT, Mai DS, Doan TK, Paris H. Wire and arc additive manufacturing of 308L stainless steel components: Optimization of processing parameters and material

properties. Engineering Science and Technology, an International Journal 2021;24:1015–26. https://doi.org/10.1016/j.jestch.2021.01.009.

[86] Tofail SAM, Koumoulos EP, Bandyopadhyay A, Bose S, O'Donoghue L, Charitidis C. Additive manufacturing: scientific and technological challenges, market uptake and opportunities. Materials Today 2018;21:22–37. https://doi.org/10.1016/j.mattod.2017.07.001.

[87] Tabatabaeian A, Ghasemi AR, Shokrieh MM, Marzbanrad B, Baraheni M, Fotouhi M. Residual Stress in Engineering Materials: A Review. Adv Eng Mater 2022;24. https://doi.org/10.1002/adem.202100786.

[88] Kudryavtsev YF. Residual Stress, 2008, p. 371–88. https://doi.org/10.1007/978-0-387-30877-7_15.

[89] McClung RC. A literature survey on the stability and significance of residual stresses during fatigue. Fatigue Fract Eng Mater Struct 2007;30:173–205. https://doi.org/10.1111/j.1460-2695.2007.01102.x.

[90] Cheng X, Fisher JW, Prask HJ, Gnäupel-Herold T, Yen BT, Roy S. Residual stress modification by post-weld treatment and its beneficial effect on fatigue strength of welded structures. Int J Fatigue, vol. 25, 2003, p. 1259–69. https://doi.org/10.1016/j.ijfatigue.2003.08.020.

[91] Shen C, Reid M, Liss KD, Pan Z, Ma Y, Cuiuri D, et al. Neutron diffraction residual stress determinations in Fe3Al based iron aluminide components fabricated using wire-arc additive manufacturing (WAAM). Addit Manuf 2019;29. https://doi.org/10.1016/j.addma.2019.06.025.

[92] Shen C, Ma Y, Reid M, Pan Z, Hua X, Cuiuri D, et al. Neutron diffraction residual stress determinations in titanium aluminide component fabricated using the twin

wire-arc additive manufacturing. J Manuf Process 2022;74:141–50. https://doi.org/10.1016/j.jmapro.2021.12.009.

[93] Sun J, Hensel J, Köhler M, Dilger K. Residual stress in wire and arc additively manufactured aluminum components. J Manuf Process 2021;65:97–111. https://doi.org/10.1016/j.jmapro.2021.02.021.

[94] Liu C, Lin C, Wang J, Wang J, Yan L, Luo Y, et al. Residual stress distributions in thick specimens excavated from a large circular wire+arc additive manufacturing mockup. J Manuf Process 2020;56:474–81. https://doi.org/10.1016/j.jmapro.2020.05.007.

[95] Ahmad SN, Manurung YHP, Mat MF, Minggu Z, Jaffar A, Pruller S, et al. FEM simulation procedure for distortion and residual stress analysis of wire arc additive manufacturing. IOP Conf Ser Mater Sci Eng, vol. 834, Institute of Physics Publishing; 2020. https://doi.org/10.1088/1757-899X/834/1/012083.

[96] Colegrove PA, Coules HE, Fairman J, Martina F, Kashoob T, Mamash H, et al. Microstructure and residual stress improvement in wire and arc additively manufactured parts through high-pressure rolling. J Mater Process Technol 2013;213:1782–91. https://doi.org/10.1016/j.jmatprotec.2013.04.012.

[97] Gornyakov V, Ding J, Sun Y, Williams S. Understanding and designing post-build rolling for mitigation of residual stress and distortion in wire arc additively manufactured components. Mater Des 2022;213. https://doi.org/10.1016/j.matdes.2021.110335.

[98] Martina F, Colegrove PA, Williams SW, Meyer J. Microstructure of Interpass Rolled Wire + Arc Additive Manufacturing Ti-6Al-4V Components. Metall Mater

Trans A Phys Metall Mater Sci 2015;46:6103–18. https://doi.org/10.1007/s11661-015-3172-1.

[99] Hönnige JR, Colegrove PA, Ahmad B, Fitzpatrick ME, Ganguly S, Lee TL, et al. Residual stress and texture control in Ti-6Al-4V wire + arc additively manufactured intersections by stress relief and rolling. Mater Des 2018;150:193–205. https://doi.org/10.1016/j.matdes.2018.03.065.

[100] Chi J, Cai Z, Wan Z, Zhang H, Chen Z, Li L, et al. Effects of heat treatment combined with laser shock peening on wire and arc additive manufactured Ti17 titanium alloy: Microstructures, residual stress and mechanical properties. Surf Coat Technol 2020;396. https://doi.org/10.1016/j.surfcoat.2020.125908.

[101] Mughal MP, Fawad H, Mufti R. Finite element prediction of thermal stresses and deformations in layered manufacturing of metallic parts. Acta Mech 2006;183:61–79. https://doi.org/10.1007/s00707-006-0329-4.

[102] Baufeld B, Brandl E, Van Der Biest O. Wire based additive layer manufacturing: Comparison of microstructure and mechanical properties of Ti-6Al-4V components fabricated by laser-beam deposition and shaped metal deposition. J Mater Process Technol 2011;211:1146–58. https://doi.org/10.1016/j.jmatprotec.2011.01.018.

[103] Wang T, Mazánová V, Liu X. Ultrasonic effects on gas tungsten arc based wire additive manufacturing of aluminum matrix nanocomposite. Mater Des 2022;214. https://doi.org/10.1016/j.matdes.2022.110393.

[104] tkD Y, H Rashed SherM. THEIDEALIZ~DSTRUCTURALUNITMETHOD AND~TSAPPLICATIONTODEEPG~RDER STRUCTURES. vol. 18. 1984.

[105] 1974_309 n.d.

[106] Murakawa H, Luo Y, Ueda Y. Prediction of Welding Deformation and Residual Stress by Elastic FEM Based on Inherent Strain (First Report) Mechanism of Inherent Strain Production. n.d.

[107] Anca A, Cardona A, Risso J, Fachinotti VD. Finite element modeling of welding processes. Appl Math Model 2011;35:688–707. https://doi.org/10.1016/j.apm.2010.07.026.

[108] Dong P, Hong JK, Bouchard PJ. Analysis of residual stresses at weld repairs. International Journal of Pressure Vessels and Piping 2005;82:258–69. https://doi.org/10.1016/j.ijpvp.2004.08.004.

[109] Wu C, Kim J-W. Review on Mitigation of Welding-Induced Distortion Based on FEM Analysis. Journal of Welding and Joining 2020;38:56–66. https://doi.org/10.5781/jwj.2020.38.1.6.

[110] Jaroslav_Mackerle_2002_Modelling_Simul._Mater._Sci._Eng._10_295 n.d.

[111] Barath Kumar MD, Manikandan M. Assessment of Process, Parameters, Residual Stress Mitigation, Post Treatments and Finite Element Analysis Simulations of Wire Arc Additive Manufacturing Technique. Metals and Materials International 2022;28:54–111. https://doi.org/10.1007/s12540-021-01015-5.

[112] Swaminathan K, Sangeetha DM. Thermal analysis of FGM plates – A critical review of various modeling techniques and solution methods. Compos Struct 2017;160:43–60. https://doi.org/10.1016/j.compstruct.2016.10.047.

[113] Buyukkaya E, Cerit M. Thermal analysis of a ceramic coating diesel engine piston using 3-D finite element method. Surf Coat Technol 2007;202:398–402. https://doi.org/10.1016/j.surfcoat.2007.06.006.

[114] Ma N. An accelerated explicit method with GPU parallel computing for thermal stress and welding deformation of large structure models. International Journal of Advanced Manufacturing Technology 2016;87:2195–211. https://doi.org/10.1007/s00170-016-8542-3.

[115] Feng Z, Ma N, Li W, Narasaki K, Lu F. Efficient analysis of welding thermal conduction using the Newton–Raphson method, implicit method, and their combination. International Journal of Advanced Manufacturing Technology 2020;111:1929–40. https://doi.org/10.1007/s00170-020-06233-6.

[116] Korioth TWP, Versluis A. MODELING THE MECHANICAL BEHAVIOR OF THE JAWS AND THEIR RELATED STRUCTURES BY FINITE ELEMENT (FE) ANALYSIS. n.d.

[117] Ding J, Colegrove P, Mehnen J, Ganguly S, Almeida PMS, Wang F, et al. Thermo-mechanical analysis of Wire and Arc Additive Layer Manufacturing process on large multi-layer parts. Comput Mater Sci 2011;50:3315–22. https://doi.org/10.1016/j.commatsci.2011.06.023.

[118] Tangestani R, Farrahi GH, Shishegar M, Aghchehkandi BP, Ganguly S, Mehmanparast A. Effects of Vertical and Pinch Rolling on Residual Stress Distributions in Wire and Arc Additively Manufactured Components. J Mater Eng Perform 2020;29:2073–84. https://doi.org/10.1007/s11665-020-04767-0.

[119] Jia J, Zhao Y, Dong M, Wu A, Li Q. Numerical simulation on residual stress and deformation for WAAM parts of aluminum alloy based on temperature function method. China Welding (English Edition) 2020;29:1–8. https://doi.org/10.12073/j.cw.20191101002.

[120] Murata H, Kato N, Tamura H. Effect of Transformation on Residual Stress in Welding Stress Releasement by Transformation Superplasticity (Part 5). n.d.

[121] Ooi SW, Garnham JE, Ramjaun TI. Review: Low transformation temperature weld filler for tensile residual stress reduction. Mater Des 2014;56:773–81. https://doi.org/10.1016/j.matdes.2013.11.050.

[122] Kromm A, Dixneit J, Kannengiesser T. Residual stress engineering by low transformation temperature alloys - State of the art and recent developments. Welding in the World 2014;58:729–41. https://doi.org/10.1007/s40194-014-0155-6.

[123] Kundu S. Transformation Strain and Crystallographic Texture in Steels. 2007.

[124] Francis JA, Kundu S, Bhadeshia HKDH, Stone HJ, Rogge RB, Withers PJ, et al. Transformation Temperatures and Welding Residual Stresses in Ferritic Steels. 2007.

[125] Harati E, Karlsson L, Svensson LE, Dalaei K. Applicability of low transformation temperature welding consumables to increase fatigue strength of welded high strength steels. Int J Fatigue 2017;97:39–47. https://doi.org/10.1016/j.ijfatigue.2016.12.007.

[126] Xu LY, Wang YF, Jing HY, Han YD. Fatigue strength improvement of stainless steel using weld toes dressing with low transformation temperature welding wire. Science and Technology of Welding and Joining 2014;19:664–72. https://doi.org/10.1179/1362171814Y.0000000240.

[127] Kromm A, Dixneit J, Kannengiesser T. Residual stress engineering by low transformation temperature alloys - State of the art and recent developments.

Welding in the World 2014;58:729–41. https://doi.org/10.1007/s40194-014-0155-6.

[128] Feng Z, Ma N, Tsutsumi S, Lu F. Investigation of the residual stress in a multi-pass t-welded joint using low transformation temperature welding wire. Materials 2021;14:1–15. https://doi.org/10.3390/ma14020325.

[129] Francis JA, Stone HJ, Kundu S, Bhadeshia HKDH, Rogge RB, Withers PJ, et al. The effects of filler metal transformation temperature on residual stresses in a high strength steel weld. Journal of Pressure Vessel Technology, Transactions of the ASME 2009;131. https://doi.org/10.1115/1.3122036.

[130] Hidekazu M, Miloslav B, Vega A, Sherif R, Davies CM, Dye D, et al. Effect of Phase Transformation onset Temperature on Residual Stress in Welded Thin Steel Plates †-state Phase Transformation) (Displacive Phase Transformation) (Residual Stress) (Finite Element Method). vol. 37. 2008.

[131] 北野 萌一＊, 照美, 中村, Houichi K, Terumi N. 低変態温度溶接材料を用いた溶融金属積層造形材の 変形低減法に関する基礎的検討 Distortion reduction of parts made by wire and arc additive manufacturing technique using low transformation temperature welding materials *. n.d.

[132] Houichi K, Terumi N. Residual stress in parts made by wire and arc additive manufacturing using low transformation temperature welding materials. n.d.

[133] Song K, Lin Z, Zhu Z, Zhao X, Ya W, Goulas C, et al. Microstructure and mechanical properties of wire and arc additive manufactured thin wall with low-temperature transformation. J Mater Sci 2023;58:13183–204. https://doi.org/10.1007/s10853-023-08645-7.

[134] Plotkowski A, Saleeby K, Fancher CM, Haley J, Madireddy G, An K, et al. Operando neutron diffraction reveals mechanisms for controlled strain evolution in 3D printing. Nat Commun 2023;14. https://doi.org/10.1038/s41467-023-40456-x.

[135] Unnikrishnan R, Idury KSNS, Ismail TP, Bhadauria A, Shekhawat SK, Khatirkar RK, et al. Effect of heat input on the microstructure, residual stresses and corrosion resistance of 304l austenitic stainless steel weldments. Mater Charact 2014;93:10–23. https://doi.org/10.1016/j.matchar.2014.03.013.

[136] Vinoth Jebaraj A, Sugavaneswaran M. Influence of Shot Peening on Residual Stress Distribution and Corrosion Resistance of Additive Manufactured Stainless Steel AISI 316L. Transactions of the Indian Institute of Metals 2019;72:1651–3. https://doi.org/10.1007/s12666-019-01601-7.

[137] Cunha L, Andritschky M. Residual stress, surface defects and corrosion resistance of CrN hard coatings1. vol. 111. 1999.

[138] Guo RQ, Zhang C, Yang Y, Peng Y, Liu L. Corrosion and wear resistance of a Fe-based amorphous coating in underground environment. Intermetallics (Barking) 2012;30:94–9. https://doi.org/10.1016/j.intermet.2012.03.026.

[139] Fusco MA, Ay Y, Casey AHM, Bourham MA, Winfrey AL. Corrosion of single layer thin film protective coatings on steel substrates for high level waste containers. Progress in Nuclear Energy 2016;89:159–69. https://doi.org/10.1016/j.pnucene.2016.02.016.

[140] Blink J, Farmer J, Choi J, Saw C. Applications in the nuclear industry for thermal spray amorphous metal and ceramic coatings. Metall Mater Trans A Phys Metall Mater Sci, vol. 40, 2009, p. 1344–54. https://doi.org/10.1007/s11661-009-9830-4.

[141] Suzuki T, Araki T, Kitaoka H, Terada K. Characterization of Non-stoichiometric Hydration and the Dehydration Behavior of Sitafloxacin Hydrate. vol. 60. 2012.

[142] Trzybiński D, Niedziałkowski P, Ossowski T, Trynda A, Sikorski A. Single-crystal X-ray diffraction analysis of designer drugs: Hydrochlorides of metaphedrone and pentedrone. Forensic Sci Int 2013;232. https://doi.org/10.1016/j.forsciint.2013.07.012.

[143] Eckardt R, Krupicka E, Hofmeister W. Validation of Powder X-Ray Diffraction Following EN ISO/IEC 17025. J Forensic Sci 2012;57:722–37. https://doi.org/10.1111/j.1556-4029.2011.02025.x.

[144] Bunaciu AA, Udriştioiu E gabriela, Aboul-Enein HY. X-Ray Diffraction: Instrumentation and Applications. Crit Rev Anal Chem 2015;45:289–99. https://doi.org/10.1080/10408347.2014.949616.

[145] Borghetti GS, Carini JP, Honorato SB, Ayala AP, Moreira JCF, Bassani VL. Physicochemical properties and thermal stability of quercetin hydrates in the solid state. Thermochim Acta 2012;539:109–14. https://doi.org/10.1016/j.tca.2012.04.015.

[146] Bragg WH, Bragg Apr WL, H Bragg BW, Professor of Physics C. The Reflection o f X-rays by Crystals. n.d.

[147] Tanaka K. X-Ray Stress Measurement by The Cos α Method Using Two-Dimensional Detector Part 1: Fundamentals of Measurements 総 説. vol. 66. 2017.

[148] Luo Q, Jones AH. High-precision determination of residual stress of polycrystalline coatings using optimised XRD-sin2ψ technique. Surf Coat Technol 2010;205:1403–8. https://doi.org/10.1016/j.surfcoat.2010.07.108.

[149] Lin J, Ma N, Lei Y, Murakawa H. Measurement of residual stress in arc welded lap joints by cosα X-ray diffraction method. J Mater Process Technol 2017;243:387–94. https://doi.org/10.1016/j.jmatprotec.2016.12.021.

[150] Prime MB. Cross-sectional mapping of residual stresses by measuring the surface contour after a cut. J Eng Mater Technol 2001;123:162–8. https://doi.org/10.1115/1.1345526.

[151] Prime MB, Dewald AT. The Contour Method 5.1 Introduction 5.1.1 Contour Method Overview. 2013.

[152] Schajer GS, Prime MB. Use of inverse solutions for residual stress measurements. J Eng Mater Technol 2006;128:375–82. https://doi.org/10.1115/1.2204952.

[153] Pagliaro P, Prime MB, Swenson H, Zuccarello B. Measuring multiple residual-stress components using the Contour method and multiple cuts. Exp Mech 2010;50:187–94. https://doi.org/10.1007/s11340-009-9280-3.

[154] Hosseinzadeh F, Kowal J, Bouchard PJ. Towards good practice guidelines for the contour method of residual stress measurement. The Journal of Engineering 2014;2014:453–68. https://doi.org/10.1049/joe.2014.0134.

[155] The contour method The contour method for residual stress measurement. 2018.

[156] Ma N. ハイブリッド解法とハイブリッドモデリング による溶接熱伝導・非線形力学挙動の解析 大阪大学接合科学研究所 麻 寧緒 Hybrid method and hybrid modelling for welding thermal-mechanical coupling analysis. n.d.

[157] Kazuki I, Shinsuke I, Satoru N, Masakazu S. Analysis of Residual Stress of Multi-pass Pipe Welding Considering 3 Dimensional Moving Heat Source Using Idealized Explicit FEM. n.d.

[158] Feng Z, Ma N, Hiraoka K, Komizo Y, Kano S, Nagami M. Development of 16Cr8Ni low transformation temperature welding material for optimal characteristics under various dilutions due to all repair welding positions. Science and Technology of Welding and Joining 2023;28:305–13. https://doi.org/10.1080/13621718.2022.2158282.

[159] Junji Y, Susumu M, Yoshiki M, Naoya H, Kazuo H. Analysis of Martensite Transformation Behavior in Welded Joint of Low Transformation-Temperature Materials. n.d.

Achievements

Publications related to doctor thesis:

(1) **Wenjia Huang**, Qian Wang, Ninshu Ma, Houichi Kitano, Distribution characteristics of residual stresses in typical wall and pipe components built by wire arc additive manufacturing, Journal of Manufacturing Processes, Volume 82, 2022, Pages 434-447, ISSN 1526-6125.

(2) **Wenjia Huang**, Qian Wang, Ninshu Ma, Houichi Kitano, Characteristics of residual stress distribution in wire-arc additive manufactured layers of low transformation temperature material, International Communications in Heat and Mass Transfer, Volume 148, 2023, 107066, ISSN 0735-1933.

(3) **Wenjia Huang**, Ninshu Ma, Qian Wang, Kazuo Hiraoka, Hisaya Komen, Chendong Shao, Fenggui Lu, Satoru Kano, Interpass temperature strategies for compressive residual stresses in cladding low-transformation-temperature material 16Cr8Ni via wire arc additive manufacturing, International Communications in Heat and Mass Transfer, Volume 157, 2024, 107777, ISSN 0735-1933.

(4) **Wenjia Huang**, Qian Wang, Ninshu Ma, Houichi Kitano., Analysis of residual stress distribution characteristic in typical WAAM components, 9th International Conference on Welding Science and Engineering (Excellent Presentation Award to Young Researcher), Harbin, 2023.

(5) **Wenjia HUANG**, Qian WANG, Ninshu MA, Houichi KITANO. Residual stress comparison in Wire Arc Additive Manufactured stainless wall and cylinder. IIW2022, Tokyo. 2022

(6) **Wenjia Huang**, Qian Wang, Ninshu Ma. Residual stress distribution in wire and arc additive manufacturing using SUS308LSi. the 1st Advances in Welding and Additive Manufacturing Research Conference 2022 (AWAMR2022), online. 2022 136

(7) 岡田雄二, 角和磨, **黄文嘉**, 馮中元, 麻寧緒, 平岡和雄, 諸岡聡, 菖蒲敬 久，LTT 補修溶接部やアークワイヤ積層材における内部残留応力の中性子測定， 2022 年 4 月溶接学会春春季全国大会，WEB 開催，2022

(8) **黄文嘉**、楢崎邦男、麻寧緒、北野萌一， アークワイヤ積層造形した SUS308 材の壁モデルと円筒モデルにおける残留応力の測定と数値解析. (一社)溶接学 会 2021 年度 秋季全国大会, WEB 開催，2021

Other publications:

(1) **Wenjia Huang**, Ninshu Ma, Yunwu Ma, Toshiro Amaishi, Kenji Takada, and Takayuki Hama. Material Model Development of Magnesium Alloy and Its Strength Evaluation, Materials 14, 2021, no. 2: 454.

(2) Qian Wang, Ninshu Ma, Junmiao Shi, **Wenjia Huang**, Xiao-Tao Luo, Peihao Geng, Mingxing Zhang, Xian-Cheng Zhang, Chang-Jiu Li, Unraveling microforging principle during in situ shot-peening-assisted cold spray additive manufacturing aluminum alloy through a multi-physics framework, Materials & Design, Volume 236, 2023, 112451, ISSN 0264-1275.

(3) Wang, Qian, Ninshu Ma, **Wenjia Huang**, Junmiao Shi, Xiao-Tao Luo, Sora Tomitaka, Satoshi Morooka, and Makoto Watanabe. Key Role of Temperature on Delamination in Solid-State Additive Manufacturing via Supersonic Impact. Materials Research Letters 11, no. 9 (2023): 742–48. doi:10.1080/21663831.2023.2227221. 137

(4) Sendong Ren, **Wenjia Huang**, Ninshu Ma, Goro Watanabe, Zhengguang Zhang, Wenze Deng, Numerical modeling from process to residual stress induced in resistance spot welding of DP980 steel. Int J Adv Manuf Technol 125, 3563–3576 (2023).

(5) Peihao Geng, Masashi Morimura, Ninshu Ma, **Wenjia Huang**, Weihao Li, Kunio Narasaki, Takuya Ogura, Yasuhiro Aoki, Hidetoshi Fujii, Measurement and simulation of thermal-induced residual stresses within friction stir lapped Al/steel plate, Journal of Materials Processing Technology, Volume 310, 2022, 117760, ISSN 0924-0136.

(6) Hong Ma, Peihao Geng, Guoliang Qin, Chunbo Zhang, Jun Zhou, **Wenjia Huang**, Ninshu Ma, Achieving superior property by forming fine-sized mult-principal element layer at the weld interface of stainless steel and medium entropy alloy, Materials & Design, Volume 223, 2022, 111255, ISSN 0264-1275

Acknowledgments

I would like to express my sincere gratitude to all those who have supported and assisted me throughout the completion of this doctoral dissertation.

First and foremost, I would like to extend my heartfelt thanks to my supervisor, Professor Ninshu Ma, for his invaluable guidance and unwavering support throughout the entire research process. His academic mentorship, constructive feedback, and encouragement have been instrumental in shaping this thesis and my academic growth. I am also very grateful to the defense committee, Professor Naoki Ohsawa, Professor Kazuhiro Iijima, and Associate Professor Akira Tatsumi, for their guidance and advice on my work.

I am also grateful to Assistant Professor Qian Wang, Associate Professor Yunwu Ma, Dr. Geng, Professor Kazuo Hiraoka, Associate Professor Hisaya Komen, and Professor Hisashi Serizawa for their active involvement and expert advice in the research project. Their expertise and insights have significantly contributed to the depth and quality of my study.

Furthermore, I wish to acknowledge the contributions of all members of the Ma lab. Dr. Kunio Narasaki, Associate Professor Junmiao Shi, Associate Professor Sendong Ren, Dr. Zhongyuan Feng, Professor Wangnan Li, Dr. Song Wu, Dr. Hongbo Xia, Dr. Mingrun Yu, Dr. Jinnan Wang, Dr. Ruwei Geng, Professor Chengsong Zhang, Professor Yunxia Chen, Dr. Yong Liu, Dr. Lei Hu, Professor Hui Huang, Dr. Fujun Cao, Associate Professor Yaqiong Ge, Associate Professor Pengkang Zhao, Professor Jiamin Sun, Professor Jingjing Li, Mr. Weihao Li, Mr. Renzhi Zhang, Dr. Yifan Gao, Mr. Mingzhe Fan, Mr. Suyu Wang, Mr. Jingjia Chen, Mr. Mohan He, Mr. Tianxing Chang, Mr.

Liangyu Fei, Mr. Kai Song, and others. Their collaboration, expertise, and camaraderie have created a conducive environment for conducting research and achieving meaningful results.

Additionally, I would like to extend my thanks to my family, especially my wife Dr. Yuelin Wang, my parents Mr. Ping Huang and Mrs. Caiping Zhang, and my friends for their unwavering support, understanding, and encouragement throughout my academic journey. Their constant support has been a source of strength and motivation.

Finally, I would like to thank the JSP SPRING program, the Joint Research Collaborative Program of JWRI, and the Osaka University international research program for their financial support, which made this research possible.

I am deeply grateful to everyone mentioned above for their contributions and support. Without their assistance, this thesis would not have been possible. Here's to continued collaboration and creating a brighter future together.